Application of DNA-based Nanofabrication in Nanoelectronics and Effect of Contaminations on the Surface Potential of Graphite

by

Ruobing Bai

B. S. in Applied Chemistry, East China University of Science and Technology, China, 2015

M. S. in Polymer Science, University of Akron, USA, 2016

Submitted to the Graduate Faculty of the

Dietrich School of Arts and Sciences in partial fulfillment

of the requirements for the degree of

Doctor of Philosophy

University of Pittsburgh

2021

UNIVERSITY OF PITTSBURGH

DIETRICH SCHOOL OF ARTS AND SCIENCES

This dissertation was presented

by

Ruobing Bai

It was defended on

July 14, 2021

and approved by

Jennifer Laaser, PhD, Assistant Professor, Department of Chemistry

Raúl Hernández Sánchez, PhD, Assistant Professor, Department of Chemistry

Feng Xiong, PhD, Assistant Professor, Department of Electrical and Computer Engineering

Dissertation Director: Haitao Liu, PhD, Professor, Department of Chemistry

Application of DNA-based Nanofabrication in Nanoelectronics and Effect of Contaminations on the Surface Potential of Graphite

Ruobing Bai, PhD

University of Pittsburgh, 2021

Reducing the critical feature size and lowering the overall fabrication cost are the keys to the future of semiconductor manufacturing. There is great interest in the development of novel electronic device manufacturing technologies compatible with high-resolution, low-cost, and large-scale fabrication. DNA-based nanofabrication technology developed in recent years is able to meet the above needs, due to its unique set of characteristics: designable patterns, nanometer-level resolution, low cost and scalability. Based on these advantages of DNA-based nanofabrication, this technology has broad prospects in the fields of electronic device manufacturing.

This dissertation focuses on the application of DNA materials in the field of electronic device fabrication. Chapter 2 introduces the method of combining DNA-based nanofabrication technology with traditional doping technology. This method can realize *n*-type patterned doping by using DNA nanostructures as patterns and dopant carriers. Chapter 3 reports the use of DNA nanostructures as templates to deliver different dopants to achieve both *n*-type and *p*-type patterned doping, thereby expanding the usability of DNA materials for doping. Chapter 4 reports the application of DNA-based doping technology in the production of PN diodes, thus demonstrating the application of DNA nanomaterials in the production of analog electronic devices. Motivated by our interest to expand the doping study to 2D materials, Chapter 5 reports the changes in surface

electrical properties of graphite materials over time in the air, allowing us to better understand the impact of air contaminations on the surface potential of graphite.

I hope this dissertation can provide more insights into the application of DNA nanostructures in the production of electronic devices, and lay a steppingstone for the application of DNA nanotechnology in the field of electronic manufacturing.

Table of Contents

List of Tables

List of Figures

Preface

First, I would like to thank my research advisor, Prof. Haitao Liu. I sincerely thank him for his support and guidance throughout my PhD. My advisor led me into the field of materials research and taught me many science-related skills. In addition, he has always cultivated our innovative thinking and encouraged me to become a real scientist. His encouragement, teaching and support helped me gain a lot on the road to PhD.

I would like to thank Prof. Jennifer Laaser and Prof. Geoffrey Hutchison for their time and assistance in my comprehensive examination. I would also like to thank Prof. Jennifer Laaser, Prof. Raúl Hernández Sánchez, and Prof. Feng Xiong for their time and effort in defending my PhD.

I also want to thank Prof. Feng Xiong for the cooperation guidance and the provision of experimental instruments for my use. I also thank Professor Lei Li for providing the laboratory for my characterization.

I would also like to thank my past and present colleagues and collaborators. Thanks to Dr. Anqin Xu, Dr. Liwe Hui, Dr. Muhammad Salim, Dr. Justin Hurst, Nathan Tolman, Min A Kim, Yanhao Du, Yihan Liu, John R Erickson, Yang Hu, and Bomin Zhang for their assistance in my research. I would also like to thank Dr. Joel Gillespie, Dr. Jun Chen and Dr. Esta Abelev for providing me with guidance and assistance in characterization techniques in the past. Thank all of you and wish you all the best in your career.

Finally, I want to thank my family (Zheng Bai, Min Liu and Ruyi Bai). My PhD study is inseparable from your support and encouragement. Thank you very much for providing me with a carefree learning environment. Hope our future will be even better.

1.0 Introduction

1.1 Doping in Semiconductors

Doping is a process of adding impurities to a pure material.[1] Addition of impurities will change the electrical conductivity of the material and make the material (such as silicon and germanium) very useful in semiconductor manufacturing.[2] Those impurities are referred to as dopants. There are two types of dopants: *n*-type dopants (electron donors) and *p*-type dopants (electron acceptors). The effective use of *n*-type and *p*-type dopants and the combination of different doped regions can create systems with many useful applications in modern electronics.[3]

1.1.1 *n*-type doping

For *n*-type doping, group V elements (such as antimony, phosphorus or arsenic) are usually used as dopants in Si. Group V elements have more outer electrons than silicon atoms. Their four external electrons are combined with adjacent silicon atoms, and the fifth electron can move freely to act as the charge carrier (Figure 1).[4] These impurity atoms provide an electron to the crystal and such impurity atoms are called donor atoms. Once the silicon crystal is doped with group V elements such as phosphorus, an *n*-type doped semiconductor is generated. Since there are more free electrons in *n*-type semiconductors, these electrons are also called majority charge carriers, and free moving holes are called minority charge carriers.

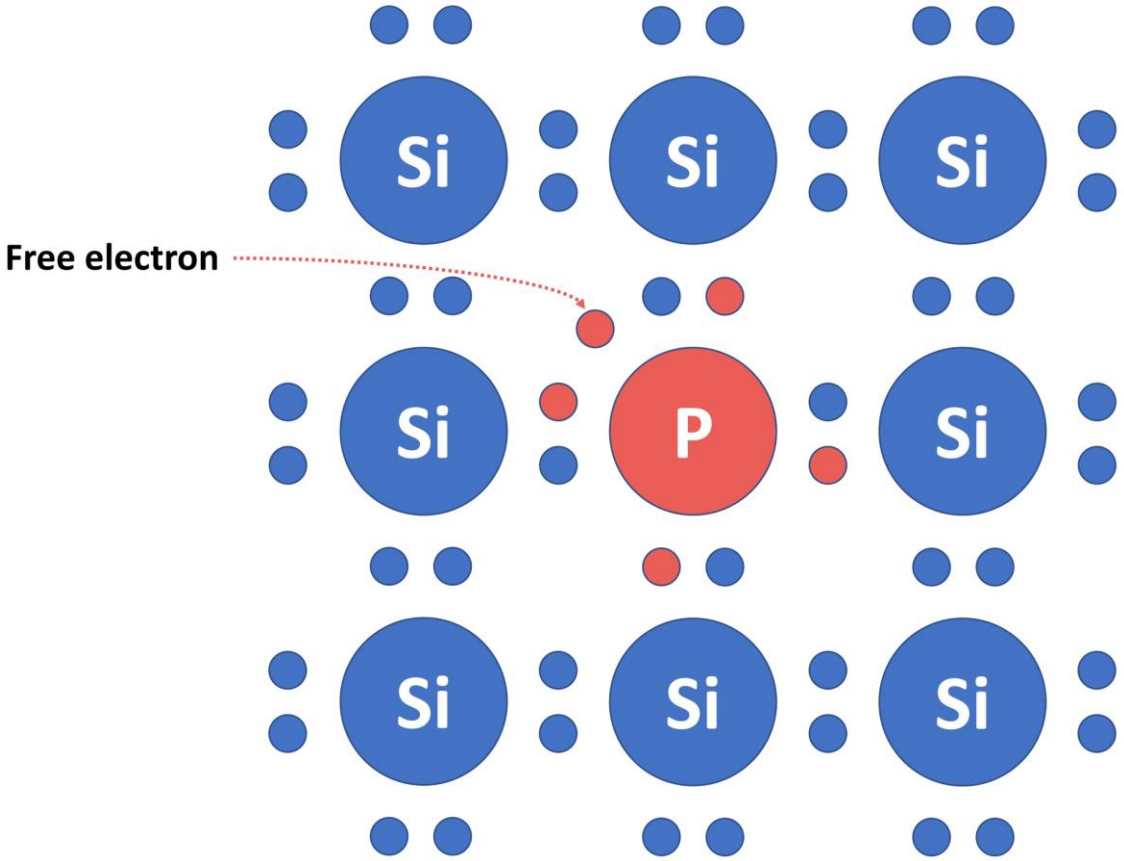

Figure 1. Schematic diagram of *n*-type doping silicon (Si) crystal using phosphorus (P).

1.1.2 *p*-type doping

For *p*-type doping, trivalent dopants such as boron, indium, gallium, and aluminum are usually used to dope silicon. The trivalent dopant atom has 3 electrons in its outer layer. Since these trivalent atoms have one electron less than the outer shell of silicon atoms, they leave a hole when they bond with silicon atoms (Figure 2).[5] These trivalent atoms can capture external electrons from silicon atoms. This type of dopant eagerly looks for a fourth electron and is called an acceptor dopant. Once the trivalent material is doped into a pure semiconductor, the semiconductor is called

the *p*-type semiconductor. In a *p*-type semiconductor, the carriers are positively charged and the moving direction of holes is opposite to the moving direction of electrons. The main charge carriers of this semiconductor are holes, while the minority charge carriers are electrons.[6]

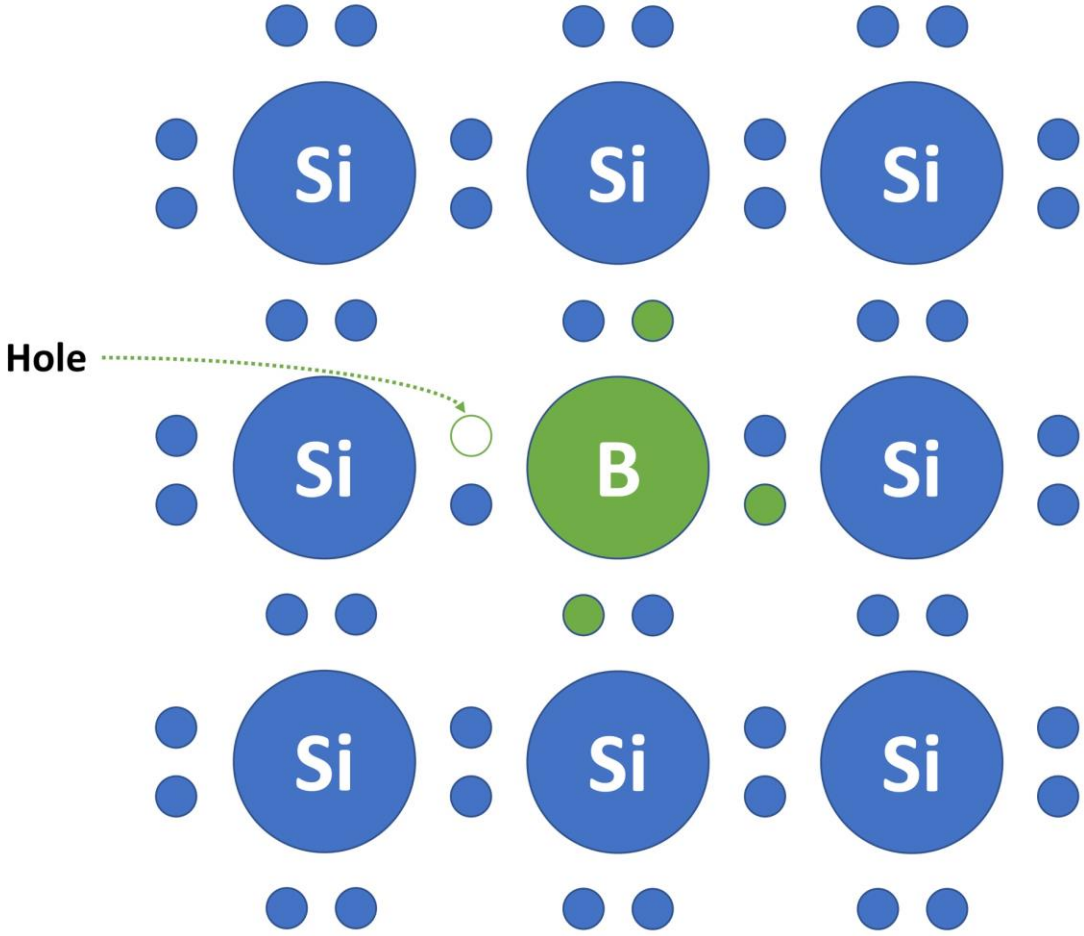

Figure 2. Schematic diagram of *p*-type doping silicon (Si) crystal using boron (B).

1.1.3 Effect of doping on the fermi level

The Fermi level is the highest energy level occupied by electrons at the temperature of 0K. Figure 3 shows a schematic diagram of the energy band diagram of a silicon semiconductor. The orbitals of the lower energy levels merge to form a band called the valence band, and the orbitals of the higher energy levels merge to form a band called the conduction band. The gap between the valence band and the conduction band is called the energy gap.[7] The Fermi level is usually located between the valence band and the conduction band. The position of the Fermi level in the semiconductor is closely related to the doping type and concentration. When there is *n*-type doping in the silicon crystal (such as using phosphorus), the excess free electrons in the doped atoms will shift the Fermi energy level up and make it easier for the electrons to jump into the conduction band. When the silicon crystal is *p*-type doped (such as using boron), the impurity atoms contain less valence electrons than silicon atoms. More holes created by impurity atoms will shift the Fermi level down.[8]

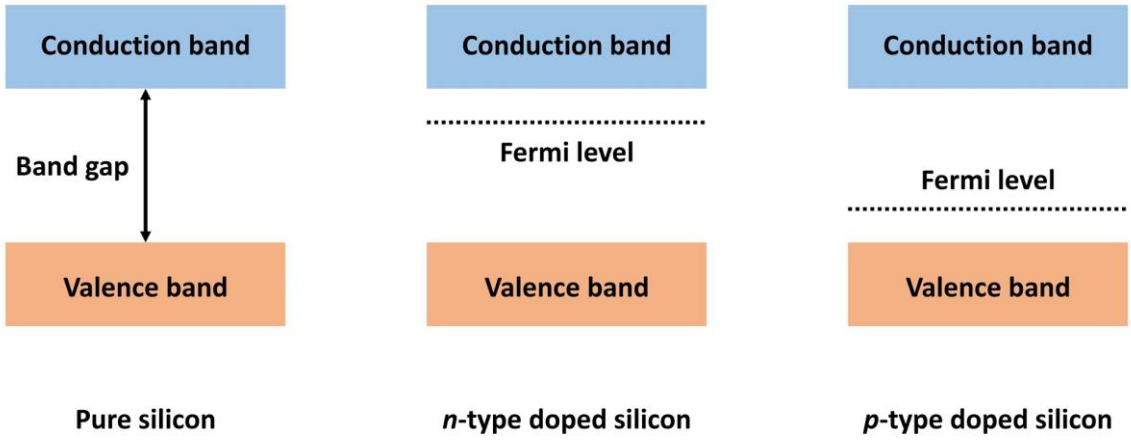

Figure 3. Schematic diagram for explaining the effect of doping on the shift of the Fermi level of silicon.

1.2 Doping Methods

Various techniques have been proposed to introduce dopants into silicon substrates. Among those techniques, ion implantation and diffusion are common methods to achieve doping. Here, we will discuss these two doping methods and the derivative doping method based on monolayers.

1.2.1 Ion implantation

Ion implantation is a method of introducing a controllable concentration of dopants at a very precise depth.[9] This method is an essential technology in the manufacture of semiconductor devices. During the ion implantation process, the charged dopants (ions) will be accelerated in an electric field and irradiated on the wafer to complete the doping.[10] The doping depth can be controlled very precisely by reducing or increasing the voltage required to accelerate the ions. The ion implantation process needs to be performed under high vacuum, and almost every element can be implanted into the wafer with high purity.[11] In addition, the process is performed at room temperature, so there is almost no lateral diffusion of dopants (illustrated in the schematic diagram in Figure 4). From the above operating conditions of ion implantation, it is not difficult to understand why ion implantation has such a precise control and excellent reproducibility for the doping process. Although ion implantation has many of the above-mentioned advantages, the damage of high-energy ions to the crystal lattice is a problem that cannot be ignored. People usually need to perform a thermal annealing process after ion implantation doping to ensure that damage is eliminated and the dopants are activated.[12-14] In addition, since the ion implanter is very

expensive, the use of ion implantation technology for doping will increase the cost of manufacturing each wafer.[15]

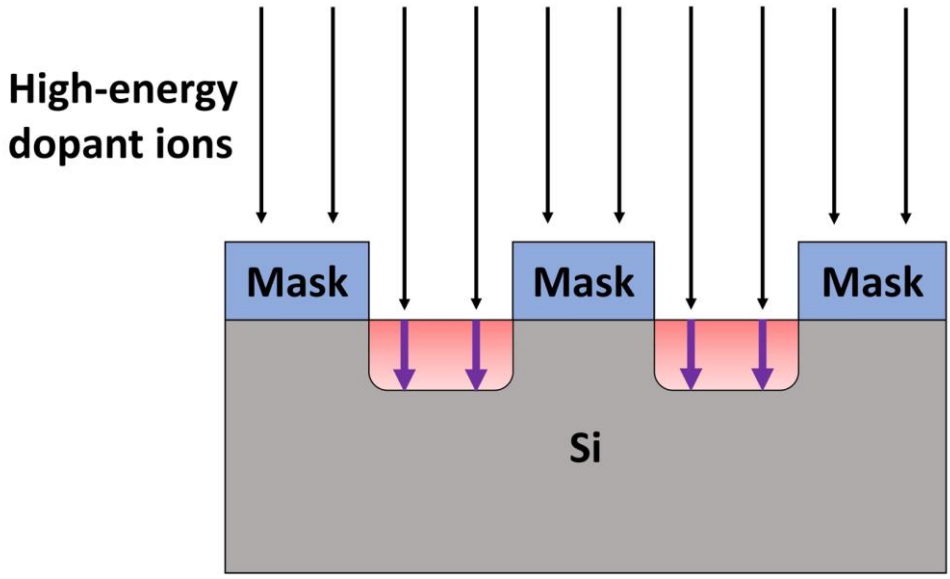

Figure 4. Schematic diagram of a silicon wafer doped by the ion implantation process.

1.2.2 Diffusion

Diffusion (the transfer of molecules from regions of higher concentration to regions of lower concentration) is another method of introducing dopants into silicon wafers.[16] This method can use a variety of different types of doping sources to achieve doping, such as gas (PH_3 or B_2H_6), liquid (BBr_3 or $POCl_3$) and solid sources (slices containing dopants). The speed of the diffusion process is closely related to the type of dopant, the concentration gradient, the temperature, the nature of the substrate and the crystallographic orientation of the substrate.[17] Generally, diffusion requires a particularly high temperature (900 °C to 1200 °C), and rapid thermal annealing (RTA)

is often used to achieve diffusion in the semiconductor manufacturing process.[18] RTA can quickly heat silicon wafers to high temperatures (over 1000 °C) in a few seconds. Once the wafer reaches this temperature, it will stay here for a few seconds to diffuse the dopants. Then finally a quenching step is performed to prevent dislocations and wafer cracks due to thermal shock. Such a rapid heating rate in RTA is usually achieved by high-intensity lamps or lasers.[19] Although the high-temperature diffusion method is convenient and can process multiple wafers at the same time, the method diffuses the dopant not only in the vertical direction but also in the lateral direction, which may cause undesirable expansion of the doped area (Figure 5).[20]

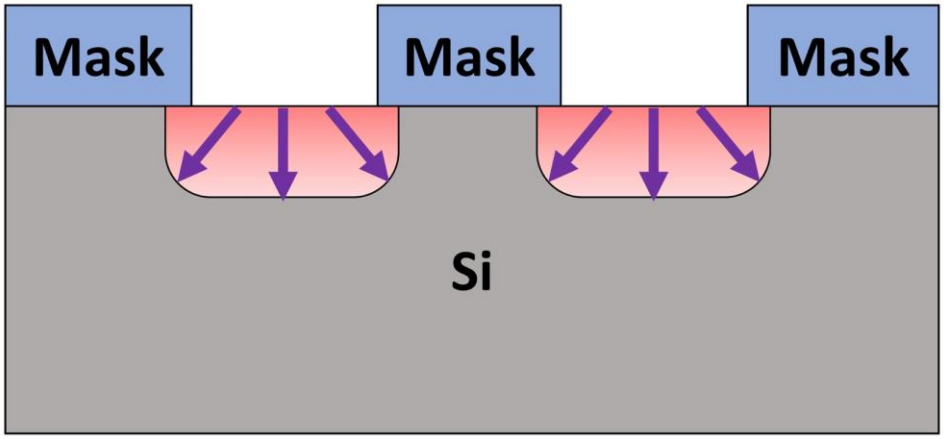

Figure 5. Schematic diagram of a silicon wafer doped by the diffusion method.

1.2.3 Monolayer doping

Monolayer doping (MLD) is a diffusion doping technology proposed in recent years.[21] The method starts by attaching a single layer of molecules containing dopant atoms to the silicon. After

the molecules are attached, a thin layer of silicon dioxide is covered on the molecular layer, and then a RTA step is performed to dope the molecules into the silicon (see Figure 6 for the monolayer doping process).[22] The doping depth of this method depends on the number of doping atoms in the single layer, the time and temperature of RTA.[23] MLD technology can use reactions to form a single layer of various molecules on silicon, and can precisely define the number of doping molecules in the impurity-containing layer.[24] These characteristics gave the MLD technology the advantages of good control and uniform formation of ultra-shallow doping distribution (a few nanometers).[25-26] In addition, MLD technology is also compatible with 3D nanomaterials, which can uniformly place dopants on multiple surfaces (including side surfaces) and perform ultra-shallow doping.[27-28] Although MLD technology has many of the above advantages, it still faces huge challenges for doping with special requirements (for example, different doping doses or different types of doping at different locations).

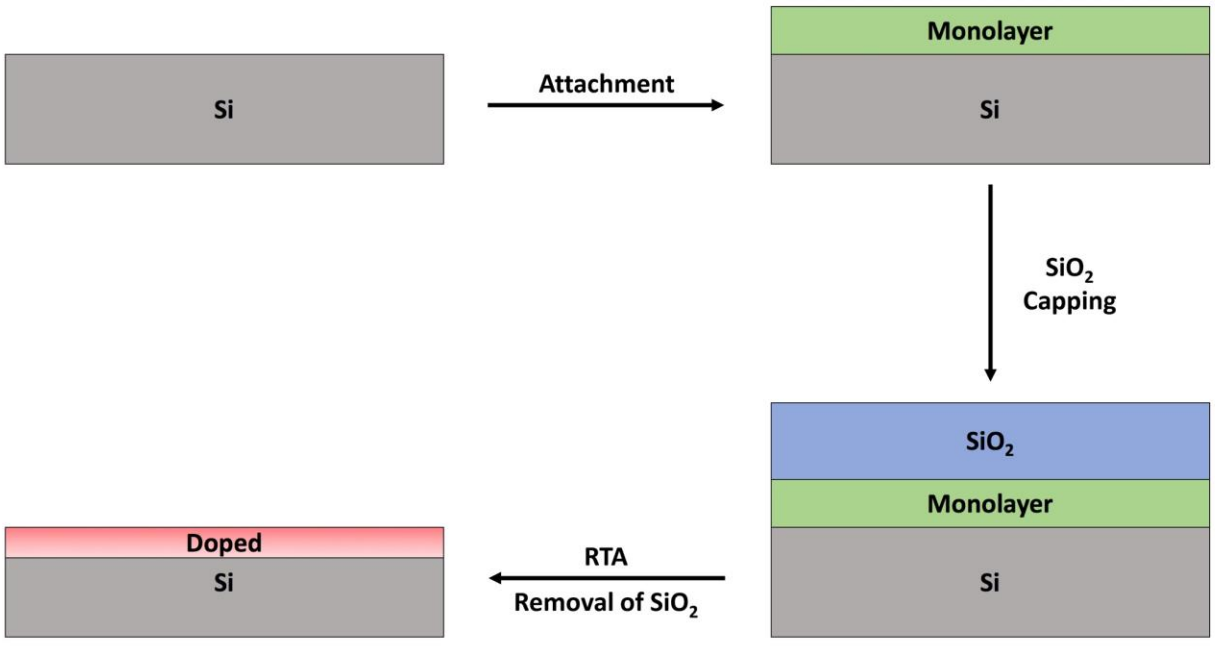

Figure 6. Schematic diagram for the monolayer doping process.

1.3 Site-specific Doping

Site-specific doping is of importance to semiconductor device fabrication because a device often requires different types and concentrations of dopants at different regions. To control the spatial location of the dopant, one typically uses a lithography step to pattern a diffusion barrier on the wafer. The diffusion barrier over the area to be doped is then etched away to expose the wafer, allowing thermal diffusion or ion implantation of the dopant atoms.[29-30] Nowadays, many different kinds of lithography methods have been proposed. These methods can be divided into top-down nanofabrication methods, such as optical lithography, scanning probe lithography, and nanoimprint lithography, and bottom-up nanofabrication methods, such as molecular self-assembly lithography.[31] In this section, some different lithography methods to form specific patterns for doping will be selected and discussed: optical lithography, nanoimprint lithography, and block copolymer lithography.

1.3.1 Optical lithography for site-specific doping

Optical lithography is a widely used process in the manufacture of semiconductor devices, which can help form doping at specific locations.[32] Generally, the traditional photolithography process requires three basic materials, photoresist, photomask and light source. Photoresist is photosensitive. There are two types of photoresist: positive and negative. The positive photoresist becomes more soluble after being exposed to a light source. In contrast, negative photoresists become less soluble after exposure. The photomask will have a designed pattern (usually up to tens of nanometers), and the pattern on the mask can be transferred to the photoresist after exposure to form the desired pattern.[33] The light source has a great influence on the resolution of the

generated pattern.[34] Depending on the light source used, the lithography technique also has some changes.[35] Ultraviolet light is the light source used in the traditional photolithography. To produce higher resolution, some other related lithography techniques have also been proposed, such as X-ray lithography, electron-beam lithography (EBL), and ion-beam lithography.[36-39] Generally, the photolithography step is to first coat a photoresist on the semiconductor. Then, the substrate coated with the photosensitive material is exposed under a mask with a specific pattern to change the solubility of the exposed area. The substrate is then washed with a suitable solvent, and the remaining photoresist pattern will protect the substrate from being doped. After the required doping process is completed, the photoresist can be removed to complete the formation of doping at specific locations on the substrate (seen Figure 7 for the process).[40] Although optical lithography has excellent resolution for fabrication, the technology relies on advanced equipment and requires a flat substrate to start with.

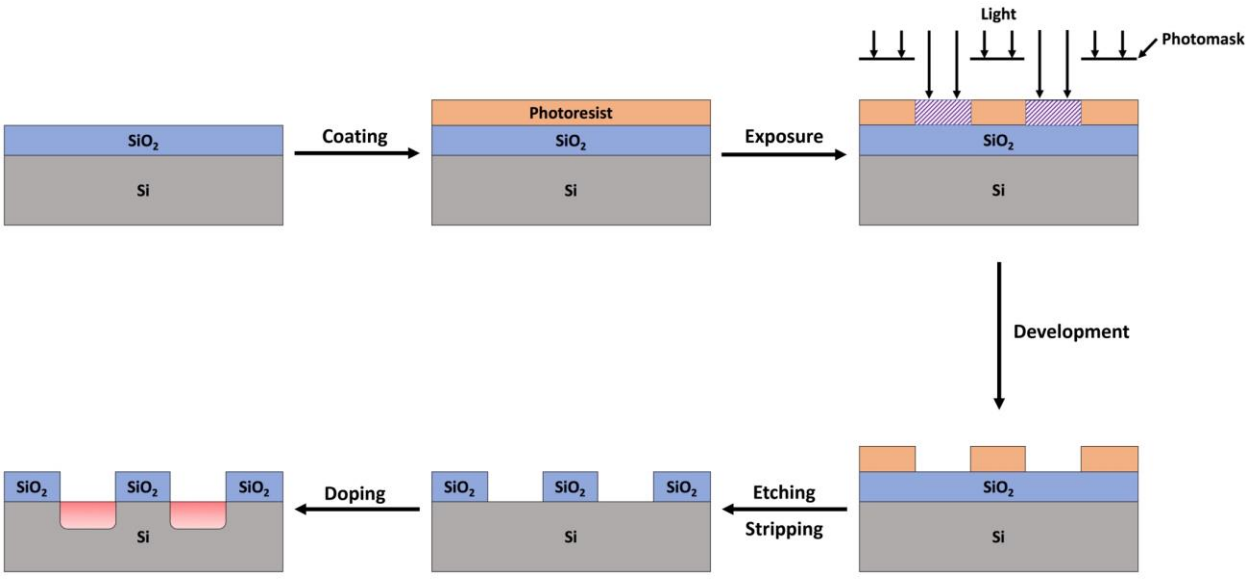

Figure 7. Schematic diagram of using the photolithography process to form the site-specific doping.

1.3.2 Nanoimprint lithography for site-specific doping

Nanoimprint lithography is a method of making nanoscale patterns using specific molds.[41] This method can also be used to help produce site-specific doping. As shown in Figure 8, this technique first spin-coats an imprint resist on the surface of the sample. The substrate and patterned mold are then pressed together. During the imprint process, thermal, optical or electrochemical methods will be used to transfer the pattern on the mold to the softened polymer film. After that, the mold is peeled from the surface of the sample, and the patterned resist can be left on the substrate.[42-43] Finally, etching and doping can be performed to form doping at specific locations. Nanoimprint lithography has many advantages such as simple process, low cost, high throughput and high resolution.[44] However, this method is highly dependent on the quality of the template. In practice, the large-scale adoption of nanoimprint lithography still faces some concerns, such as overlay, defects, and template patterning and template wear.[45]

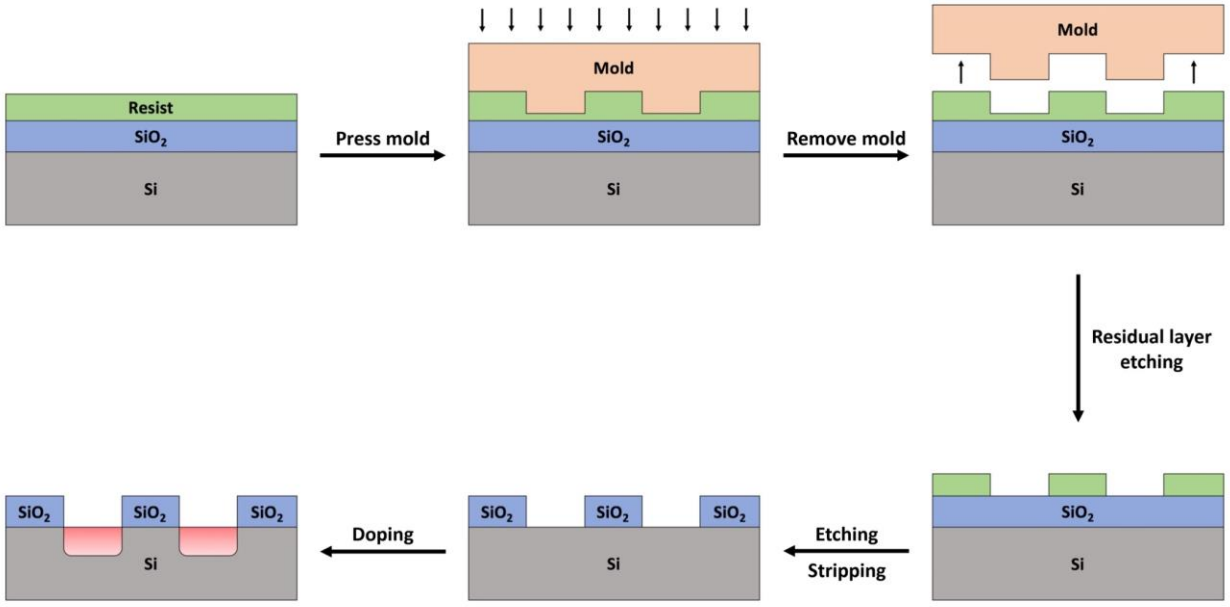

Figure 8. Schematic diagram of using the nanoimprint lithography process to form the site-specific doping.

1.3.3 Block copolymer lithography for site-specific doping

Block copolymer lithography is a bottom-up lithography method.[46-47] This method can also help form the site-specific doping. Block copolymer lithography uses various phase separation morphologies of block copolymers to pattern the substrate, and its feature size can be as small as a few nanometers (<10 nm).[48-50] Figure 9 shows the steps of this method. First, the block copolymer is deposited on the surface of the substrate. Then annealing is used for the phase separation step, so that the block copolymer forms an ordered structure, such as spherical, cylindrical, and layered structures. After that, the unwanted polymer phase is removed, and the remaining polymer phase forms the desired pattern. Finally, steps such as etching, stripping and

doping can be performed to obtain the site-specific doped substrate. The block copolymer lithography technology combines the self-assembly of block copolymers with lithography technology, thereby providing a simple and low-cost method for forming nanoscale patterns on a substrate.[51] However, this method still faces challenges for forming complex shapes of various designs, such as the shape of logic circuits. In addition, the block copolymer lithography method has not been well developed in the site-specific doping process.

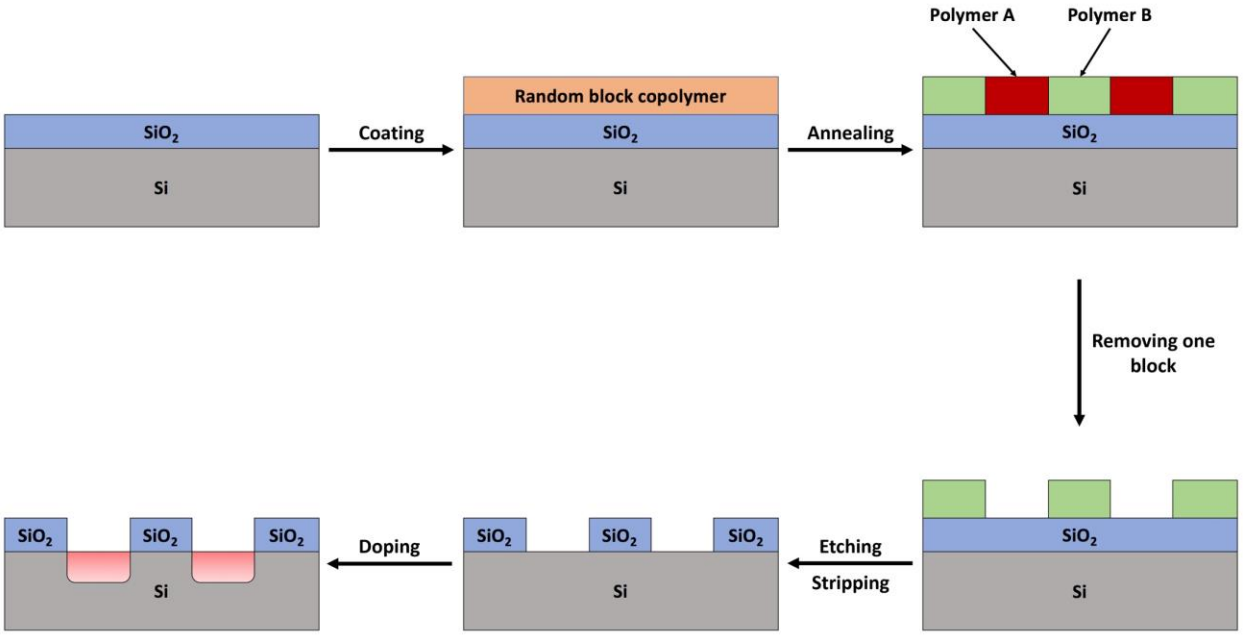

Figure 9. Schematic diagram of using the block copolymer lithography process to form the site-specific doping.

1.4 DNA-based Nanofabrication

While many lithography methods that have been proposed can well form doping at specific locations, some methods such as optical lithography are inseparable from the lithography step, which will increase the overall cost of the manufacturing process. In addition, since each doping step will deliver a fixed type and dosage of the dopant, multiple lithography and doping steps are needed if a device/circuit design calls for different doping types and/or concentrations.[52-53]

A major focus of the semiconductor research and development is to continuously reduce the critical feature size and lower the overall fabrication cost.[54-56] Therefore, it is of great interest to develop novel doping strategies that are compatible with high resolution patterning, low cost, and large scale fabrication.

Recently, the use of DNA nanostructures for bottom-up nanofabrication has attracted a lot of attentions. Although DNA materials are perceived to be expensive, 2D nanofabrication requires only a monolayer amount of DNA template and the recent development of the bio-based manufacturing process significantly lowered the cost of DNA nanostructures. It is estimated that the cost of DNA template can be less than $\$1/m^2$ for large scale 2D patterning.[57] DNA-based nanofabrication offers the best of both top-down and bottom-up fabrication methods: designer pattern, which is typically offered by top-down methods, and scalability/low cost, which is usually associated with bottom-up methods. Many protocols have been reported to achieve high resolution pattern transfer (10 nm resolution demonstrated in some cases) from a DNA template to SiO_2, Si, graphene, polymer and self-assembled monolayers (SAMs).[58-65] Shape programming and the ability to precisely place nanoscale objects make DNA nanostructures have great potential in the future of electronic product manufacturing. In this section, we will introduce DNA-based nanofabrication technology and discuss its applications, especially in the field of electronics.

Finally, we will propose some specific challenges in applying DNA nanomaterials to the fabrication of actual electronic devices.

1.4.1 DNA self-assembly

The idea of using DNA to construct nanoscale structures was first reported by Seeman in 1982.[66] Among the examples they demonstrated include a four-arm branched structure by using four single-stranded DNA with complementary sticky ends (Figure 10a).[67-68] Then, in 2006, Rothemund further expanded the idea of Seeman by using DNA origami technology to construct various highly complex and controllable structures.[69] They first designed multiple short single-stranded DNA, and then used them to fold the long single-stranded DNA into the desired shape through complementary base pairing (Figure 10b). They have demonstrated many different shapes of DNA nanostructures synthesized by this method, such as triangles, stars and rectangles (Figure 10c).[69] Since then, the methods of using DNA to design and construct various complex structures have been greatly developed. A series of 1D, 2D and 3D structures formed by DNA have also been widely reported (Figure 10d-f).[70-72] These structures include, but are not limited to, nanotubes,[73-74] nanoribbons,[75-76] hexagonal arrays,[77] cubes,[78] and polyhedron.[79-80] These different DNA structures have great potential for applications in many fields, such as chemical biology, drug delivery, energy transfer, photonics and electronics.[57, 81-86]

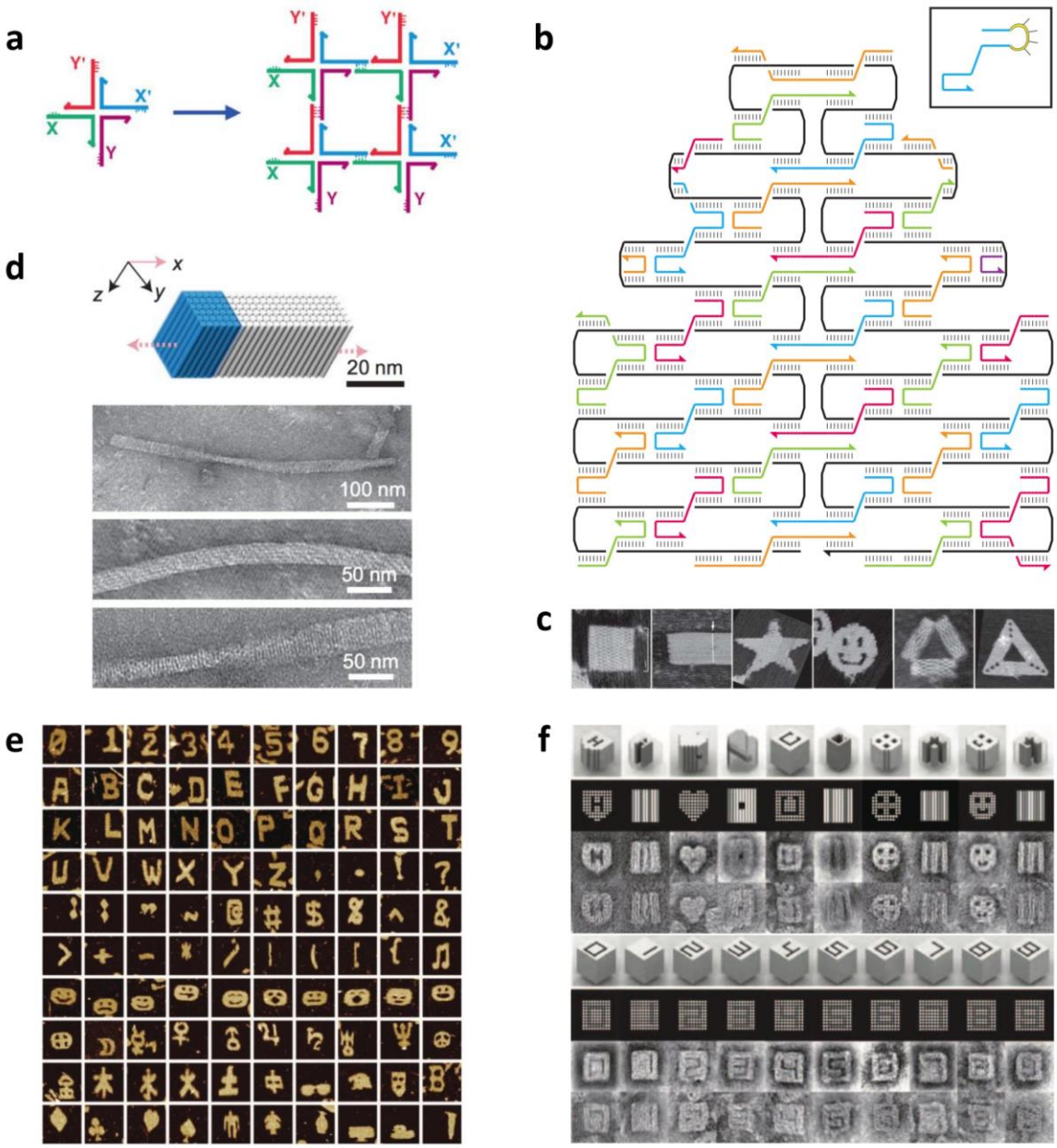

Figure 10. Examples of various shapes constructed by DNA self-assembly. a, Assembly of four branched DNA molecules with sticky ends to form a larger quadrilateral structure. b, A design of DNA origami to construct complex and controllable shapes. c, Atomic force microscopy (AFM) images of arbitrary shapes formed by DNA origami technology. The size of each image is 165 nm × 165 nm. d, Model and transmission electron microscopy (TEM) images of a 1D DNA crystal. e, AFM images of complex 2D shapes self-assembled from DNA.

Each image is 150 nm × 150 nm in size. f, Models and TEM images of complex 3D shapes self-assembled from DNA bricks. Reprinted with permission from: a, Reference 67, copyright © 2005, IOP Publishing Ltd; b, c, Reference 69, copyright © 2006, Springer Nature; d, Reference 70, copyright © 2014, Springer Nature; e, Reference 71, copyright © 2012, Springer Nature; f, Reference 72, copyright © 2012, American Association for the Advancement of Science.

1.4.2 Large scale DNA templates

If DNA templates are to be used in the mass production of electronic devices, the key issue of how to precisely control the deposition of DNA templates needs to be solved. The most promising solution to this problem is to produce large-size DNA templates (for example, the size of μm or even mm), and then deposit them on the substrate. In this way, large-scale DNA structures can be used directly on the substrate without the need for other complicated techniques to precisely control the deposition of DNA nanostructures.[87-90]

In DNA origami technology, using a longer scaffold is a direct way to increase the size of DNA origami, because the length of the scaffold determines the size of the DNA origami structure. People have tried some methods to extend the length of DNA scaffolds, such as polymerase chain reaction (PCR), circle-to-circle amplification and rolling-circle amplification.[91-93] Marchi et al. used a single-stranded DNA scaffold with a length of 51466 nucleotides instead of a traditional single-stranded DNA scaffold with a length of 7249 nucleotides and successfully created a larger DNA origami size (Figure 11a).[94]

Another more promising way to increase the size of DNA templates is to create small fragments of DNA nanostructures and then assemble these fragments into superstructures. The binding of DNA fragment units can interact through specific interactions (for example, hydrogen bonding between sticky ends) or non-specific interactions. Woo et al. and Rafat et al. reported that in the presence of Na^+, the diffusion rate of DNA nanostructures on the surface is faster, which can form a micron-level superlattice structure (Figure 11b).[95-96] Seeman et al. used cross-shaped DNA origami to construct DNA origami arrays by self-assembling DNA spiral structures in two independent directions. They have created large 2D arrays by using sticky end associations (Figure 11c).[97] Dietz et al. demonstrated that shape complementarity can also be used to assemble DNA structures. They designed 3D DNA origami building blocks and successfully assembled these DNA fragments into micron-scale DNA structures through the rules of shape complementarity (Figure 11d).[98]

Combining different subunits through specific molecular recognition can generate more complex large-scale DNA structures. In this case, each subunit needs to be specially designed to have a specific recognition function so that it can combine other nearby subunits in a specific way. Rothemund et al. designed the ends of DNA nanostructures so that they can form specific micron-scale DNA structures through a geometric arrangement of blunt-end stacking interactions (Figure 11e).[99] By establishing and using both blunt-end stacking and associations between very short sticky ends, Qian et al. also succeeded in creating large-scale DNA structures (Figure 11f).[100]

Although many methods have been proposed to increase the size of DNA assembly structures, the formation of large and complex DNA structures (for example, the shape of a large logic circuit template) usually requires the combination of more different DNA structural units. In addition, there are usually extremely high requirements on the accuracy of the structure in the

production of devices. In this case, the manufacturing cost and synthesis errors of large-size DNA are also key issues that need to be resolved.

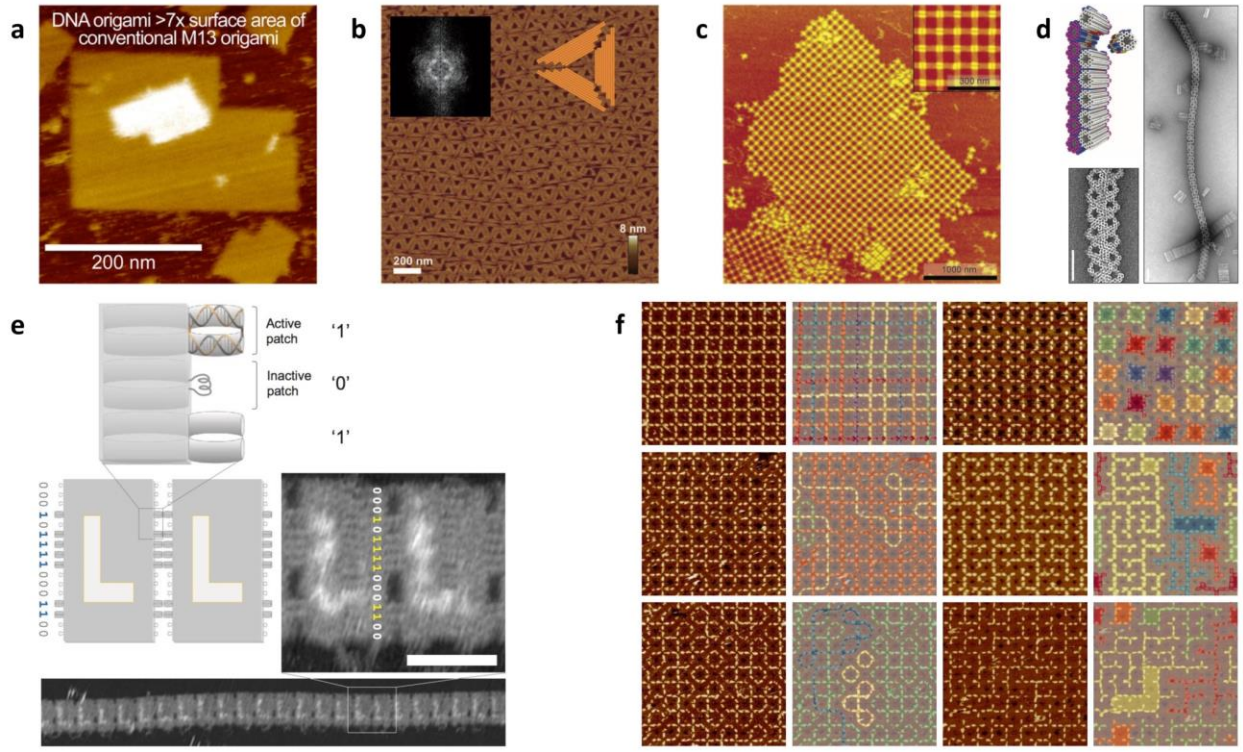

Figure 11. Examples of making large-scale DNA structures. a, AFM image of a large DNA origami structure prepared from a super longer DNA scaffold. b, AFM image of a superlattice structure formed by closely packed DNA nanostructures. c, AFM image of a large 2D DNA origami array created by using sticky end associations. d, Higher-order DNA origami structures created through the rules of shape complementarity. Scale bar: 50 nm. e, A large DNA structure created by the molecular recognition. The scale bar is 60 nm. f, Patterns constructed with programmable disorders by using both blunt-end stacking and associations between very short sticky ends. The size of each image is 880 nm × 880 nm. Reprinted with permission from: a, Reference 94, copyright © 2014, American Chemical Society; b, Reference 95, copyright © 2014, John Wiley and Sons; c, Reference 97, copyright

© 2011, John Wiley and Sons; d, Reference 98, copyright © 2015, American Association for the Advancement of Science; e, Reference 99, copyright © 2011, Springer Nature; f, Reference 100, copyright © 2016, Springer Nature.

1.4.3 Low-cost production of DNA structures

Continuously reducing production costs is a constant pursuit of the electronics manufacturing industry. Therefore, if DNA materials are to be used in the field of electronic manufacturing, it is extremely important to develop low-cost methods to produce DNA nanostructures.

Reducing the cost of synthesizing DNA strands is a direct way to reduce the cost of producing DNA structural templates. At present, some methods have been proposed to produce DNA nanostructures in *vivo* to reduce production costs. For example, Seeman proposed a bacterial culture method to prepare DNA nanostructures on a large scale.[101-102] Subsequently, bacterial plasmids have also been used to produce long DNA chains, including the preparation of the M13mp18 sequence, which is most commonly used in DNA structure.[103] Recently, Dietz et al. used bacteriophages to generate single-stranded precursor DNA, which contains target strand sequences interleaved with self-excising 'cassettes'. In this way, they can produce single-strand DNA of almost any length and sequence in a scalable and cost-effective manner (Figure 12a). They also estimated that the cost of producing DNA nanostructures with this method can be greatly reduced by three orders of magnitude, reaching 0.18 euros per milligram.[104]

Reducing the use of different DNA sequences and optimizing the synthesis process are very helpful in reducing the total cost. Generally, the formation of complex and large DNA

structures involves many customized short DNA strands to fold long DNA strands, which will greatly increase production costs. In recent years, Marchi et al. described a method for realizing cheap DNA synthesis by an inkjet-printing process on a chip embossed with functionalized micro pillars made from cyclic olefin copolymer.[94] Niekamp et al. recently demonstrated a method of folding a custom template chain by binding individual staple sequences to multiple positions on the template. In this way, they can use only 10 staples to fold a 6k-nt scaffold with repetitive sequences into complex DNA origami nanostructures, thereby effectively reducing the material cost for producing DNA origami structures (Figure 12b).[105] Using only single-stranded DNA to assemble and form structures is very attractive for reducing the mass production cost of DNA structures. Mao et al. demonstrated that two short and identical single strands of DNA construct superstructures of pre-designed 1D and 2D arrays (Figure 12c).[106] Yin et al. respectively demonstrated the process of constructing diversified multi-base single-stranded DNA and RNA and folding them into DNA and RNA nanostructures (Figure 12d).[107]

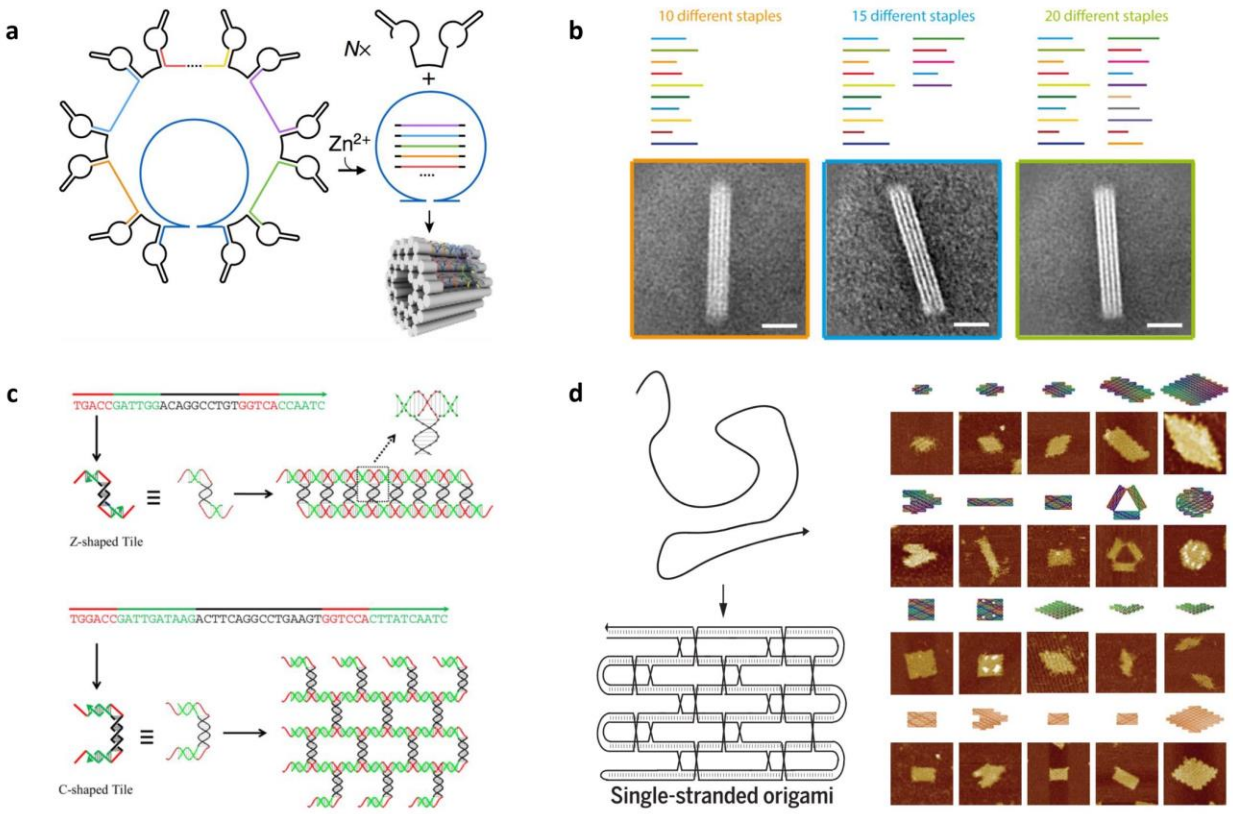

Figure 12. Examples of low-cost production of DNA structures. a, Bacteriophages for the mass production of DNA. b, DNA nanostructures folded with custom scaffolds using 10, 15 or 20 unique staple sequences. Scale bars: 20 nm. c, Self-assembly from single strands of DNA into 1D and 2D arrays. d, DNA and RNA nanostructures folded from single-stranded DNA and RNA. Reprinted with permission from: a, Reference 104, copyright © 2017, Springer Nature; b, Reference 105, copyright © 2016, Oxford University Press; c, Reference 106, copyright © 2014, American Chemical Society; d, Reference 107, copyright © 2017, American Association for the Advancement of Science.

1.4.4 Pattern transfer based on DNA templates

The process of copying the pattern of the template to other materials is called pattern transfer. Pattern transfer is particularly important to produce electronic devices, and this process is usually achieved by photolithography. Studying the pattern transfer of DNA templates on other materials is extremely important for the use of DNA materials in the field of electronic manufacturing.

There have been many reports confirming that DNA template patterns can be transferred to metallic materials. Generally, these reports directly utilize or modify the chemical characteristics of DNA, and then bind metal ions or metals to specific sites on the DNA structure to control the nucleation growth of nanocolloids or the direct binding of metal nanoparticles.[108] In this way, it has been proven that many metals (such as Ag, Pd, Cu, Au, etc.) can bind to the DNA template and remain on the substrate in the same pattern as the DNA template.[109-114] Recently, Yin et al. also used DNA molds to design and synthesize inorganic nanostructures with arbitrarily three-dimensional shapes. They fixed a single gold seed in the three-dimensional cavity of the DNA structure. Then, the further growth of the gold seed in the cavity can fill and replicate the shape of the cavity, so that three-dimensional inorganic materials with various structures can be generated (Figure 13a).[115] Metallized DNA nanostructures can also be used as a mask to pattern other inorganic materials, such as graphene[116] and 2D transition metal dichalcogenides.[117]

The pattern of DNA template has also been confirmed to be transferable to a variety of inorganic oxide materials. Surwade et al. reported that DNA nanostructures can adjust the gas phase HF etching of SiO_2 depending on the reaction conditions to produce positive or negative pattern transfer to SiO_2 (Figure 13b).[58, 63] Then Surwade et al. also reported that the DNA template can regulate the chemical vapor deposition of inorganic oxide materials (such as SiO_2 and TiO_2)

to form inorganic oxide nanostructures that inherit the shape of the DNA template. This method can produce positive and negative patterns on various substrates, such as silicon, mica, and gold (Figure 13c).[59] Hui et al. recently also combined DNA nanostructures with atomic layer deposition (ALD) technology to realize the patterning of a series of metal oxides (such as Al_2O_3, TiO_2 and HfO_2).[118]

In addition, Surwade et al. reported that unmodified DNA nanostructures can block the deposition of organosilanes in the gas phase. Therefore, they can pattern single-component and mixed SAMs of arbitrary shapes with nanometer-scale resolution.[60] Tian et al. also showed that DNA nanostructures can be printed on polymer substrates, which can then be used in soft lithography.[61]

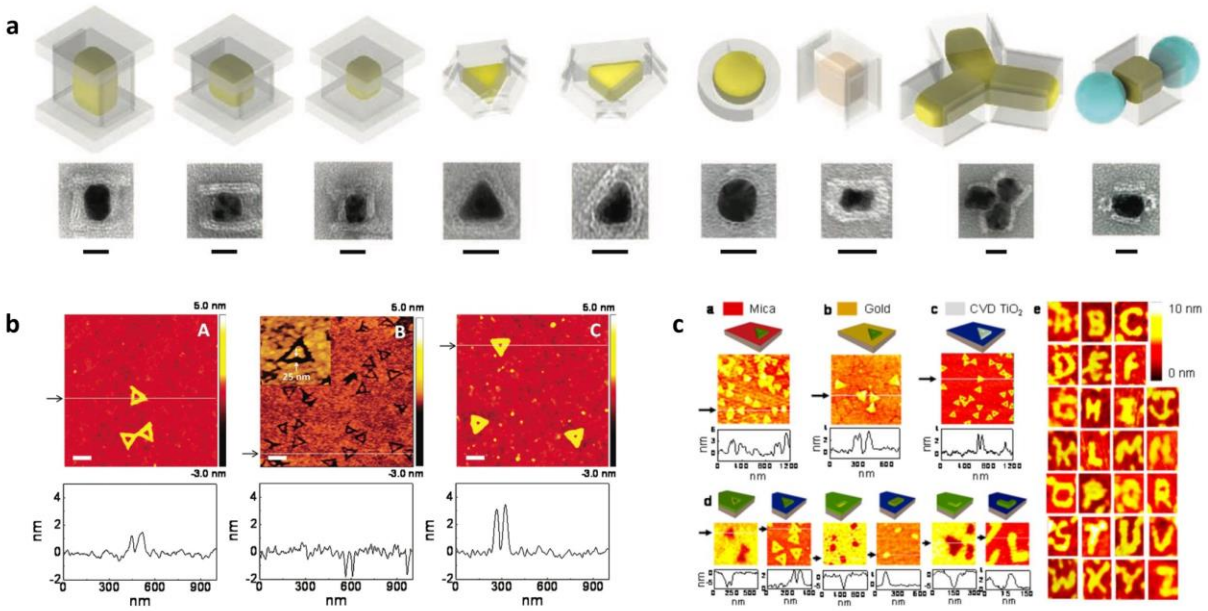

Figure 13. Examples of pattern transfer based on DNA templates. a, Casting inorganic structures with DNA molds. Scale bars: 20 nm. b, AFM images of pattern transfer from DNA nanostructures to SiO_2. DNA origami on a SiO_2 surface (left), negative pattern transferred

(middle), positive pattern transferred (right). c, Pattern transfer from various DNA templates to inorganic oxides on different substrates. The size of the 26 positive SiO_2 patterns (right) is 140 nm × 160 nm. Reprinted with permission from: a, Reference 115, copyright © 2014, American Association for the Advancement of Science; b, Reference 58, copyright © 2011, American Chemical Society; c, Reference 59, copyright © 2013, American Chemical Society.

1.4.5 Limitations and challenges of DNA nanostructures for nanofabrication

Since the manufacturing process of electronic devices usually involves harsh chemical reaction conditions (such as high temperature, high energy, plasma, HF etching, etc.), it is necessary to study the application of DNA nanostructures under extreme chemical conditions. These studies are also very helpful for the application of DNA materials in the field of nanoelectronics. Traditionally, the application of DNA nanostructures is limited to low temperature and/or aqueous environments because DNA lacks the required chemical stability. The thermal decomposition of DNA usually occurs at around 200 °C (190-230 °C).[119-120] Even for DNA on a dry substrate, the thermal stability of DNA will be limited when the temperature is higher than 250 °C.[121-122] In addition to poor thermal stability, the small thickness (1D and 2D) and high porosity of DNA nanostructures may also limit the masking and protection capabilities of the DNA template during pattern transfer. Facing the limitation of the chemical stability of DNA nanostructures, some strategies and methods have been proposed.

One of the strategies to enhance the stability of DNA structure is to selectively grow thin metal layers on the DNA structure. After coating the thin metal layer, the DNA structure becomes

sufficiently stable. Then, reactions such as ion etching can be performed to pattern the substrate. Jin et al. reported that using metallized DNA nanostructures as a mask to pattern single-layer graphene through an oxygen plasma etching reaction (Figure 14a).[116]

In addition to the use of metal coatings, other alternative coatings have also been explored to improve the stability of the DNA structure. Yan and Fan's team demonstrated a method of coating an amorphous silica layer on 1D, 2D, and 3D DNA nanostructures, which increased the strength of the template by a factor of ten (Figure 14b).[89, 123] Recently, Liu et al. have also enhanced the mechanical stability of DNA nanostructures by coating a thin layer of Al_2O_3 on DNA nanostructures. The Al_2O_3 thin layer grown by ALD can maintain the shape of the DNA template, so the template can be reused in imprint technology.[124]

Some studies performed rapid thermal treatment on DNA nanostructures covered with a thin layer of SiO_2 or Al_2O_3 at *ca.* 1000 °C. One study pointed out that at high temperatures, the carbonization of organics in DNA produced amorphous carbon nanostructures, while another study pointed out that carbon materials reacted with Si to form SiC nanostructures.[125-126] In both cases, the thin film coating limits the deformation of the DNA during decomposition, so the new product can also maintain the shape of the DNA nanostructure. In related studies, Liu et al. found that even without a covering layer, heat treatment or UV/O_3 decomposition of DNA nanostructures left residues of the same pattern.[122] These related works point out that materials that are transformed into the same pattern after processing may continue to be useful in the production of semiconductor devices.

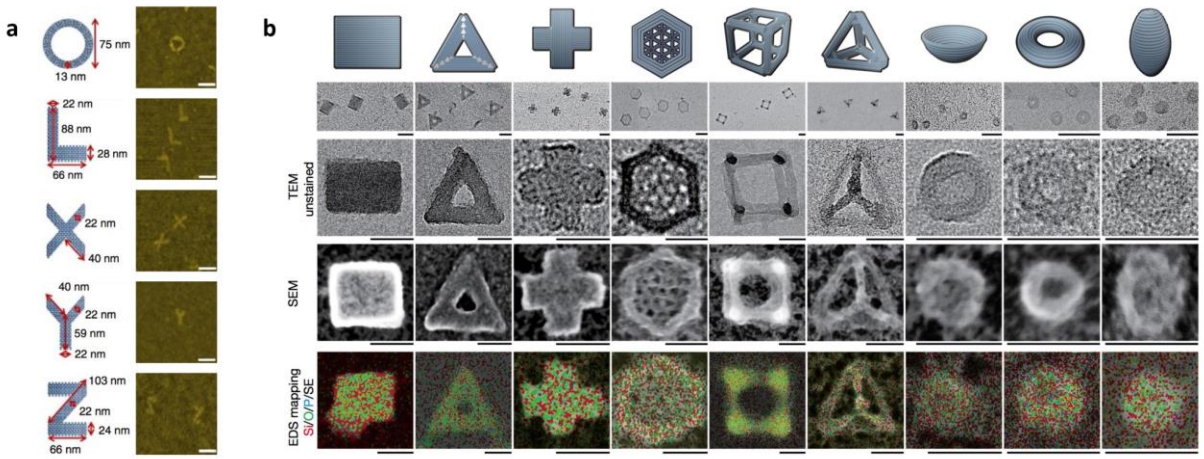

Figure 14. Examples to enhance the stability of DNA structures. a, Graphene patterned using metallized DNA nanostructures as a mask. The scale bars are 100 nm. b, Complex silica composite nanomaterials templated with DNA origami. Scale bars, zoomed-out 100 nm and zoomed-in 50 nm. Reprinted with permission from: a, Reference 116, copyright © 2013, Springer Nature; b, Reference 123, copyright © 2018, Springer Nature.

Although DNA-based nanofabrication has made significant progress and development, it still requires a lot of effort to apply this technology to the electronics industry. Compared with existing transistors with a minimum feature size of *ca.* 5 nm, the minimum 4 - 6 nm feature size of DNA nanostructures does not seem to have a clear advantage. However, the low capital and low operating costs of bottom-up DNA-based nanofabrication may provide opportunities for this technology to have practical applications in the field of electronic processing.

Before DNA materials can be better used for actual manufacturing in the electronics industry, it is necessary to develop methods to make DNA-based nanofabrication technologies compatible with existing semiconductor manufacturing technologies (such as photolithography,

etching, doping, etc.). This requires continuous research and efforts to develop DNA-based semiconductor manufacturing technology.

The use of DNA-based nanofabrication technology to complete tasks that are difficult to accomplish with existing semiconductor manufacturing technologies may enable this technology to have better practical application prospects in the electronics industry. For example, DNA-based nanofabrication may allow the modification of DNA nanostructures to simultaneously process multiple locations on the substrate surface with different effects, which usually requires multiple traditional processes to achieve. In addition, it is also promising to use DNA-based nanofabrication technology to develop surface patterning processes for super-large or curved substrates (such as automobiles, glass or ships) without using a clean room, which is usually difficult to achieve with traditional photolithography.

Noting the great potential of DNA in the field of electronic manufacturing, we would like to point out three specific challenges that we want to solve in the use of DNA to make electronic products. The first challenge is to use DNA at high temperatures. In the manufacturing process of electronic products, some harsh conditions are usually involved. For example, a high temperature of about 1000 degrees is used in the diffusion doping process; however, when the temperature exceeds 200 degrees, DNA may be damaged. Therefore, to be able to use DNA at high temperatures to achieve site-specific doping is a challenge. To overcome this challenge, we used the residues of DNA after its oxidation, which have the similar pattern as the original DNA, to achieve *n*-type site-specific doping. In this case, we can use the residue contains phosphorus atoms which act as a doping source at high-temperature to achieve *n*-type doping. The second challenge is to achieve the bottom-up doping in any desired patterns and polarity. Although monolayer doping has many advantages such as precise control of dopants concentration, multi-surface

doping and ultra-shallow doping depth, this doping method is not well developed for bottom-up patterned doping. To address this challenge, we used DNA as a template to pattern mixed monolayers that contain boron or phosphorus atoms, and then achieved *n*-type and *p*-type site-specific doping using these patterned monolayers. The third challenge is to use DNA nanotechnology to make electronic devices and showcase the benefit of using DNA nanostructure in electronics manufacturing. To address this challenge, we demonstrated a method of manufacturing transistors through DNA-based patterning and doping, and successfully produced field-effect devices and PN diodes. We show that DNA nanostructure can server as both a patterning template and doping template, potentially allowing significantly time and cost saving of device manufacturing.

2.0 DNA-Based Strategies for *n*-type Site-specific Doping

2.1 Chapter Preface

Materials contained in this chapter were published as a research article in *Advanced Functional Materials*; materials and figures used in this chapter have been reprinted with permission from: *Advanced Functional Materials*, **2021,** *31*(1), 2005940. Copyright © 2021, John Wiley and Sons.

List of Authors: Ruobing Bai, Yanhao Du, Anqin Xu, Yang Hu, John R Erickson, Liwei Hui, Jun Chen, Feng Xiong, Haitao Liu

Author Contributions: R.B., F.X. and H.L. designed and directed the experiments. R.B., Y.D., and Y.H. conducted the experiments. All authors discussed the results. R.B. and H.L. wrote the manuscript with input from all authors.

2.2 Introduction

Site-specific doping is an essential component in the manufacturing of almost all semiconductor devices, such as transistors,[127-128] sensors,[129] and photovoltaics.[130] The doping type (*n* or *p*), concentration, and spatial profile of the dopant atoms impact many, if not all, operation characteristics of the device.[131-133] A major focus of the semiconductor research and development is to continuously reduce the critical feature size and lower the overall fabrication cost.[54-56]

Therefore, it is of great interest to develop novel doping strategies that are compatible with high resolution patterning, low cost, and large scale fabrication.

To control the spatial location of the dopant, one typically uses a lithography step to pattern a diffusion barrier (e.g., SiO_2) on the wafer. The diffusion barrier over the area to be doped is etched away to expose the wafer, allowing thermal diffusion or ion implantation of the dopant atoms.[29-30] While this approach works well, it requires a lithography step, which contributes to the overall cost of the fabrication process. Besides, since each doping step will deliver a fixed type and dosage of the dopant, multiple lithography and doping steps are needed if a device/circuit design calls for different doping types and/or concentrations.[52-53]

Here we propose and demonstrate a strategy to use DNA nanostructures as the template to define the doping region and as the dopant carrier to deliver dopant to Si wafer. In the simplest implementation, we show that the phosphorus atoms naturally contained in DNA can diffuse into Si under high temperature to result in localized *n*-type doping. By using this method, we can overcome the problem of using DNA at high temperatures, because we will use inorganic residues that have a similar pattern to the original DNA. Compared to the conventional doping strategies, this approach is unique in that it has the potential to deliver different types and/or dosages of dopants within one doping step. Such a capability could dramatically reduce the number of lithography and doping steps in the fabrication of semiconductor devices.

Our work is inspired by the recent development of monolayer-based doping, which uses SAMs of phosphorus- or boron-containing molecules as the dopant source to dope Si. The monolayer decomposes at high temperature to release the dopants, which diffuse into the underlying Si substrate. This monolayer doping approach can produce ultra-shallow junction depth of a few nanometers and is suitable for large-volume production.[24, 26, 134] However, this approach

still requires a lithography step to define the area to be doped and the dopant dosage cannot be spatially varied within one doping step.

Previous research has extensively explored the use of DNA nanostructures for bottom-up nanofabrication. Although DNA materials are perceived to be expensive, 2D nanofabrication requires only a monolayer amount of DNA template and the recent development of the bio-based manufacturing process significantly lowered the cost of DNA nanostructures. It is estimated that the cost of DNA template can be less than $\$1/m^2$ for large scale 2D patterning.[57] DNA-based nanofabrication offers the best of both top-down and bottom-up fabrication methods: designer pattern, which is typically offered by top-down methods, and scalability/low cost, which is usually associated with bottom-up methods. We and others have reported protocols to achieve high resolution pattern transfer (10 nm resolution demonstrated in some cases) from a DNA template to SiO_2, Si, graphene, polymer and SAMs.[58-65] Here, we show the programmability of the DNA nanostructure also enables site-specific doping of Si wafer.

2.3 Experimental Section

2.3.1 Materials

Intrinsic silicon wafers [100] with native oxide layers were purchased from WaferPro. DNA strand for the nanotube synthesis was purchased from IDT (Sequence: 5'-CCA AGC TTG GAC TTC AGG CCT GAA GTG GTC ATT CGA ATG CCT GAG CGC TCA-3'). Sulfuric acid, acetic acid (≥99.7%), 2-Amino-2-(hydroxymethyl)-1,3-propanediol (Trizma base or Tris, ≥99.9%), ethylenediaminetetraacetic acid (EDTA, ≥99%), magnesium acetate tetrahydrate

(≥99%), hydrogen peroxide solution (30% wt. % in water), and ethanol were purchased from Sigma-Aldrich (St. Louis, MO). Nanopure water (18.3 MΩ) was obtained using a water purification system (Barnstead MicroPure Standard, Thermo Scientific, Waltham, MA) and used throughout the entire experiment to prepare chemical solutions and clean experimental samples.

2.3.2 Deposition of DNA nanotubes onto the silicon wafer

The synthesis and deposition of DNA nanotubes here were based on previous published paper.[61, 135] Briefly, we diluted the DNA single strand in 10 × TAE-Mg^{2+} buffer (400 mM tris-acetic acid, 10 mM EDTA, 125 mM Mg^{2+}, pH = 8.0) to a final concentration of 2 μM. The DNA single strand solution was then slowly cooled down from 95 °C to 23 °C in 2 days and stored at 4 °C overnight for the subsequent deposition step. A Si/SiO_2 substrate was cleaned by piranha solution (3/7 (v/v) hydrogen peroxide/sulfuric acid solution) for 30 min (*Warning*: piranha solution reacts violently with organic compounds, please handle in a fume hood and use proper personal protection equipment). The prepared DNA sample (10 μL) was then pipetted onto the cleaned wafer and placed in a plastic petri dish. We then inserted a wet Kimwipe between the lid and the bottom to maintain high humidity inside the petri dish and reduce the evaporation. After 40 minutes of undisturbed incubation, we dried the Si substrate with N_2 gas, then immersed it into an 8/2 (v/v) ethanol/water solution for 20 seconds to remove salt impurities and then dried the substrate with N_2 gas again. This washing and drying process was repeated 3 times.

2.3.3 Site-specific doping

After UV/O_3 and the deposition of the capping layer, the samples were subjected to the RTA process using a Surface Science Integration RTA Solaris 75 instrument. In this process, the temperature rose to 1000 °C within 20 seconds and this temperature was maintained for either 10 or 30 seconds. Then the temperature of the entire system was cooled down to 150 °C within 3 minutes. After the RTA process, we used 1% HF to remove the silicon dioxide capping layer and a hot piranha solution (for 60 min) to wash away any phosphate residues on the surface. The wafer was washed with HF (1%) again to remove the oxide layer produced on the substrate during the piranha washing process. Finally, the sample was washed with deionized water and dried with N_2 gas.

2.3.4 AFM characterization

Throughout the study, AFM topography images were acquired in tapping mode using an Asylum MFP-3D Atomic Force Microscope with HQ:NSC15/Al BS AFM probes (325 kHz, 40 N/m) purchased from MikroMasch (NanoAndMore USA). Conductive atomic force microscopy (CAFM) images were obtained by using the same instrument in contact mode with Budget Sensors ContE-G tips (13kHz, 0.2 N/m). Kelvin probe force microscopy (KPFM) images of the samples were acquired using tapping mode with Budget Sensors Tap 190E-G tips (190 kHz, 48 N/m). The KPFM measurements were performed in an amplitude-modulated system by using a two-pass technique. The first pass was to determine the topography of the surface and the second pass was to measure the contact potential difference (CPD) of the sample surface. For the second pass, the

separation distance was varied from 10 nm to 30 nm and the applied tip voltage was 3 V. All images were analyzed by Igor Software (Version 6.3.7.2) as part of the Asylum Research package.

2.3.5 Device fabrication and characterization

The dielectric layer and metal contacts were patterned by EBL using a Raith e-Line system. A 20 nm of HfO_2 layer was deposited by ALD using a Cambridge Nanotech Fiji ALD system, covering all the surfaces where the metal would lay down except for the small area where the metal contacted with the nanowire. The metal contacts were 2 nm of Ti and 90 nm of Au evaporated using a Plassys electron beam evaporator. Finally, the metal contacts were wire-bonded to a chip carrier using aluminum wires. The device was then tested by a Keithley 4200A-SCS Parameter Analyzer in a vacuum chamber at room temperature.

2.4 Results and Discussion

2.4.1 Site-specific doping of Si wafer using DNA nanostructures as dopant carriers

We first show that the phosphorus atoms naturally present in the DNA can diffuse into Si wafer at high temperature to result in localized *n*-type doping. As shown in Figure 15, we deposited DNA nanotubes onto a Si wafer (intrinsic wafer with the native oxide) and used UV/O_3 to remove the organic components from the DNA. Our previous work showed that the phosphate groups in DNA remained on the substrate after the oxidation of the DNA and maintained the same shape of the DNA nanostructure.[125] We then used sputtering to deposit a thin layer of SiO_2 onto the

substrate, followed by a treatment of RTA at 1000 °C to diffuse the phosphorus atoms into the Si substrate. Here, the SiO_2 capping layer prevents the loss of phosphorus atoms and limits their lateral diffusion during the doping step. Finally, we removed the SiO_2 capping layer with a HF wash to expose the Si substrate and cleaned the surface using the piranha solution.

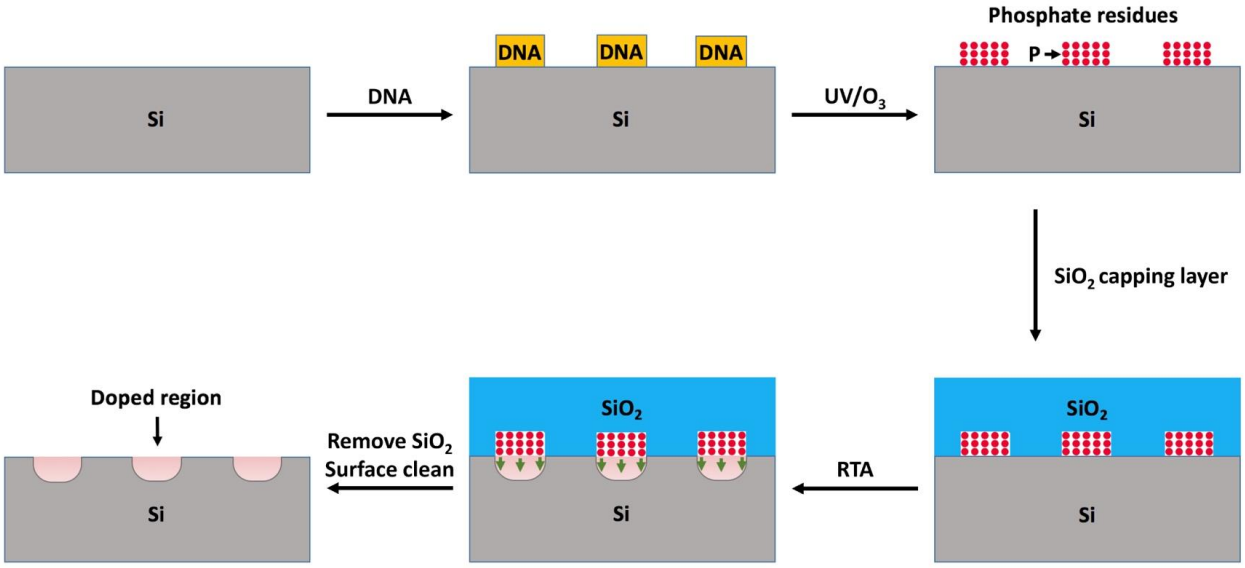

Figure 15. Schematic diagram of using DNA nanostructures as dopant carriers to prepare site-specific *n*-type doped silicon wafers.

2.4.2 Confirmation of site-specific doping

Figure 16a shows the AFM images of DNA nanotubes deposited on the Si wafer and the resulting phosphate residue after the UV/O_3 treatment. Each micrometer-long DNA nanotube was self-assembled from one short DNA single-strand containing four palindromic segments. These self-assembled DNA nanotubes have a width of ≈70 nm and a height of ≈2.0 nm, indicating that

they collapsed after drying. After UV/O_3 treatment, the height of DNA nanotubes reduced to ≈0.5 nm (Figure 16b). The height change is consistent with the expected oxidative removal of the organic components in DNA, as we previously reported.[125] The morphology of the phosphate residue mimics that of the DNA nanotubes before the UV/O_3 treatment.

After coating the whole wafer with a SiO_2 capping layer, we triggered the diffusion of the dopants into the silicon wafer through an RTA process. The oxide capping layer was then removed to allow characterization. We first used KPFM to characterize the surface of the doped wafer to investigate its surface morphology and electrical properties. From the topography and potential images (Figure 16c, d), we observed wire-like structures on the wafer. These features are very shallow trenches (1 - 2 nm in depth) and show a positive surface potential contrast of ≈50 mV compared to the flat area. The difference in the surface potential is expected because doping shifts the Fermi level of Si and the positive surface potential here also confirms the *n*-type doping effect by DNA (see the KPFM images in Figure 27 and Figure 41 in other chapters for a better understanding).[8] The shallow trench is likely due to doping-enhanced etching of Si.[136-137] In subsequent sections, we discuss further on the formation of these shallow trenches as well as a method of determining the dopant diffusion length based on doping-enhanced etching of Si.

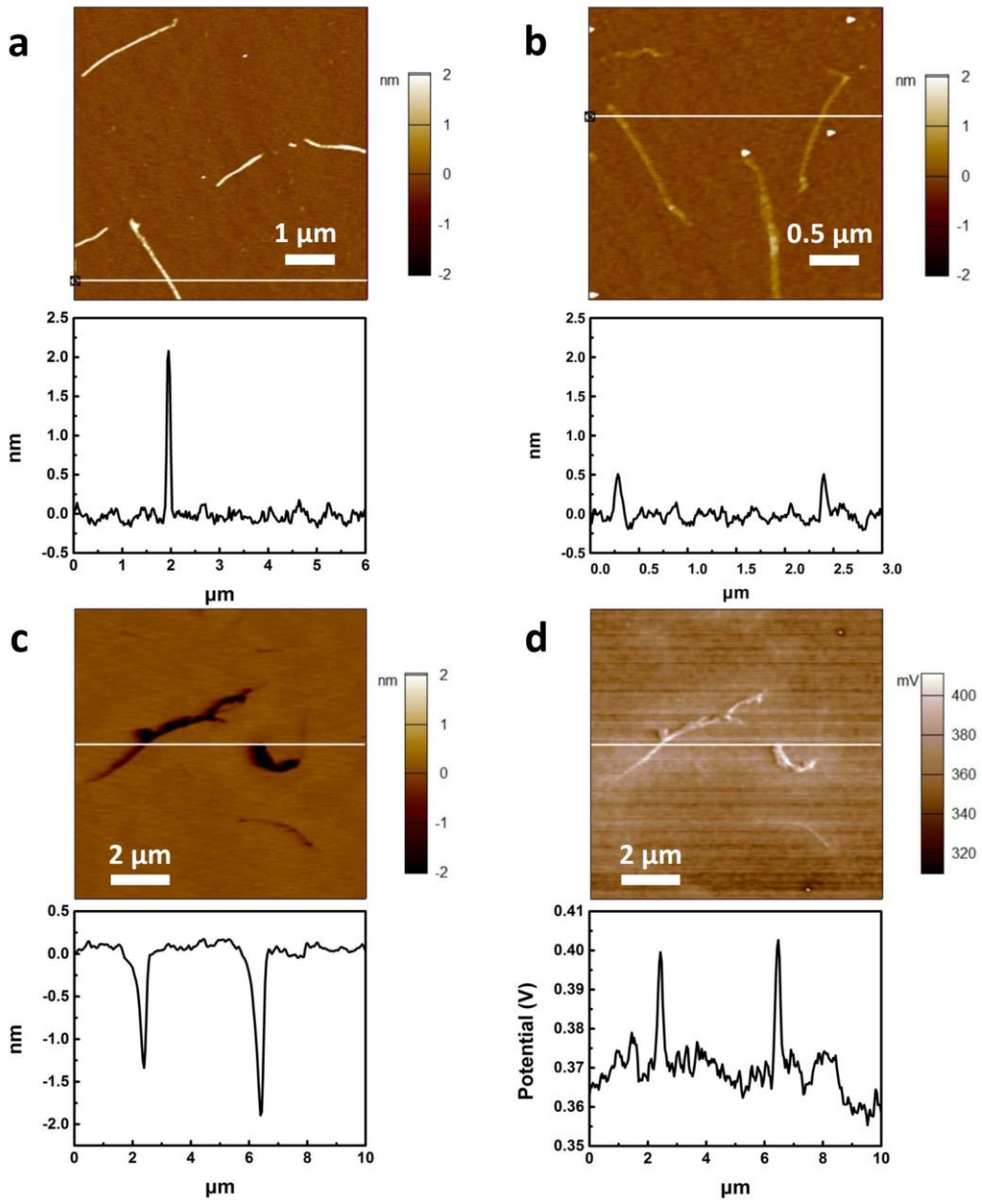

Figure 16. AFM and KPFM characterization of the site-specific *n*-type doping of Si wafers by using DNA nanostructures as dopant carriers. a, DNA nanotubes deposited on an intrinsic Si wafer. b, Phosphate residue after oxidation of DNA nanotube with UV/O_3. c, d, KPFM topography and potential images after the Si was doped by the phosphate residues. White line indicates the cross section where the below relationship graph is obtained. The doped wafer tested here was processed by RTA for 30s.

We used CAFM to characterize another doped sample. Shown in Figure 17, we observed trench-like features that are highly conductive, as seen in the current map. This observation is expected as doping (either *n* or *p*) increases the conductivity of Si. The trenches here is slightly deeper than those shown in Figure 16, which we attribute to the variations in the degree of solid-state reaction under different RTA and etching conditions. Overall, these data indicate the successful doping of Si by DNA.

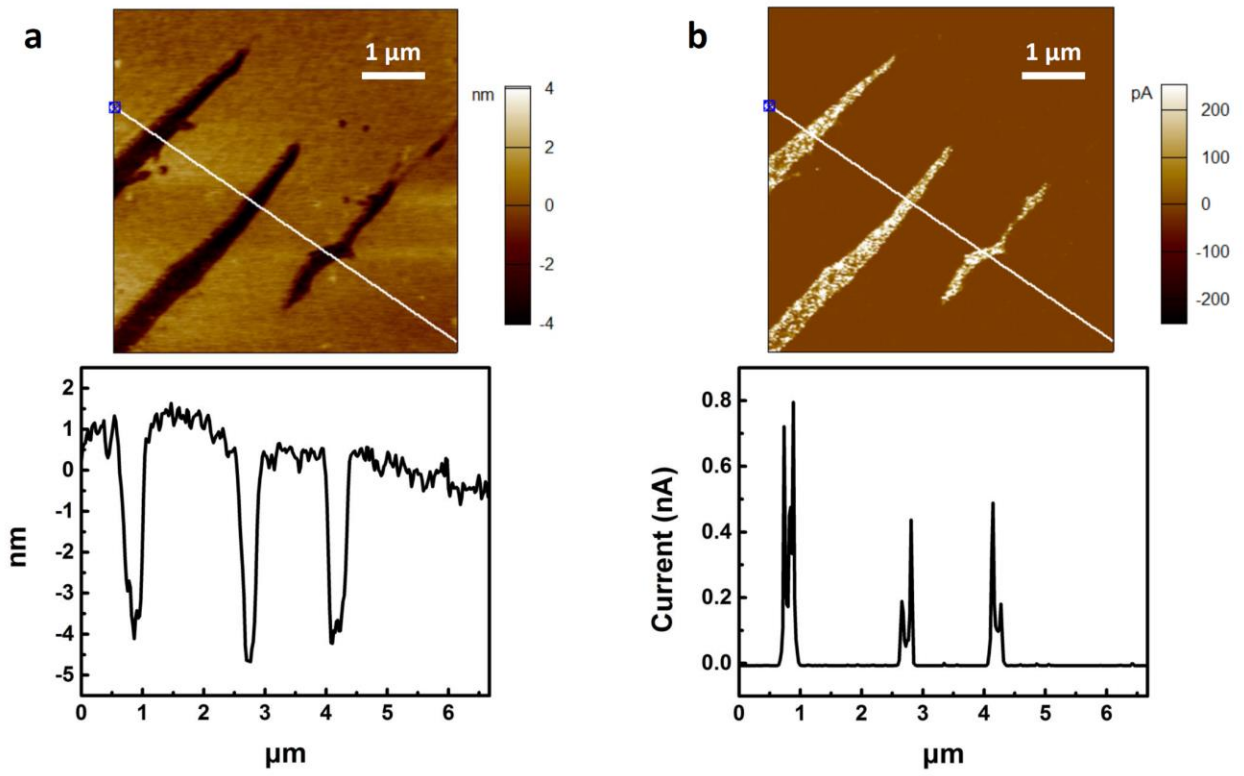

Figure 17. CAFM images and cross sections of the site-specific doped wafer by using DNA as the dopant carrier. a, Topography image. b, Current map. For this sample, 30s of RTA was used and the CAFM test was performed under a sample voltage of 0.5 V.

2.4.3 Determination of the dopant diffusion length and doping resolution

After confirming that the site-specific doping did occur, our next goal is to determine the dopant diffusion depth. Previous work showed that doping affects the etching rate of Si due to the formation of a borate or phosphate glass layer at the high dopant density and this behavior can be used to visualize the spatial distribution of the dopant in Si.[138] However, the reported etching protocols do not show significant change of etching-rate dependence when the dopant concentration is below 10^{18} cm^{-3}.[138-139]

Here, we have developed a new method to directly measure the doping depth of our samples. We found that the depth of the trench-like feature increased after repeated cycles of piranha wash (which oxidizes a thin layer of Si into SiO_2) and HF wash (which removes SiO_2 to expose underneath Si). This observation implies that the doped region (trench) is more reactive than the non-doped region (background). From the experimental results in Figure 18 (also see Figure 19), we can see that for the first 16 piranha-HF cycles, the depth of the doped region (measured at the same location) increased almost linearly per cycle to ≈14 nm and plateaued until cycle 20. From separate experiments, we estimated that the un-doped Si was etched at a rate of 0.9 nm per cycle (see Eq. 1 for details). Combining these results, we calculated that the dopant diffusion length is ≈30 nm (≈0.9 nm × 16 + 14 nm). The experimental result is in good agreement with the theoretical estimate for the doping depth (33 nm) using a diffusion model (see Eq. 2 for details).

The lateral diffusion length is expected to be similar to the vertical doping depth because the wafer was capped by SiO_2 and the diffusion of phosphorous atoms in SiO_2 is several orders of magnitude slower compared to that in Si (SiO_2 is often used as the blocking layer in conventional doping processes). The width of the doped region, as measured by KPFM/CAFM was ≈100 nm

wider than that of the corresponding DNA nanostructure. This value is twice of the calculated diffusion distance for these samples using Eq. 2 (≈50 nm for 30 s RTA treatment). However, we note that the intrinsic resolution of KPFM/CAFM is too low (20 – 30 nm) to draw a quantitative conclusion here.

The doping depth/width is a function of doping temperature, time, and initial surface dopant density. The former two parameters can be varied during the RTA and the last one can be manipulated by changing the DNA structure. Under the same processing condition, the ultimate doping resolution can be obtained from using a single-stranded DNA as the doping source. In this case, the diffusion length can be estimated based on the same diffusion model and equation (Eq. 2). Since the areal density of phosphorus atoms of a single-stranded DNA is ≈¼ of that of the DNA nanotubes (two layers of double-stranded DNA) used here, we expect that the doping distance when using a single-stranded DNA will be ≈50% of that obtained using DNA nanotubes, that is, ≈15 nm after RTA at 1000 °C for 10 s. Reducing the temperature and time of RTA may further reduce the doping length to the sub-10 nm region.

The geometry of the DNA nanostructure could also impact the doping resolution. The highest doping resolution can be achieved using linear 1D DNA nanostructures. For 2D structures (*e.g.*, criss-cross patterns), the doping resolution will decrease near the intersections and corners due to increased availability of dopant near these areas (dopant diffusion from multiple strands and/or higher density of dopant at the junction/corner). For 3D DNA nanostructures, the doping resolution will be further decreased due to the much higher dopant density. Additional concerns, such as the mechanical deformation of the DNA nanostructure during drying, makes 3D DNA nanostructure even less attractive as a dopant source.

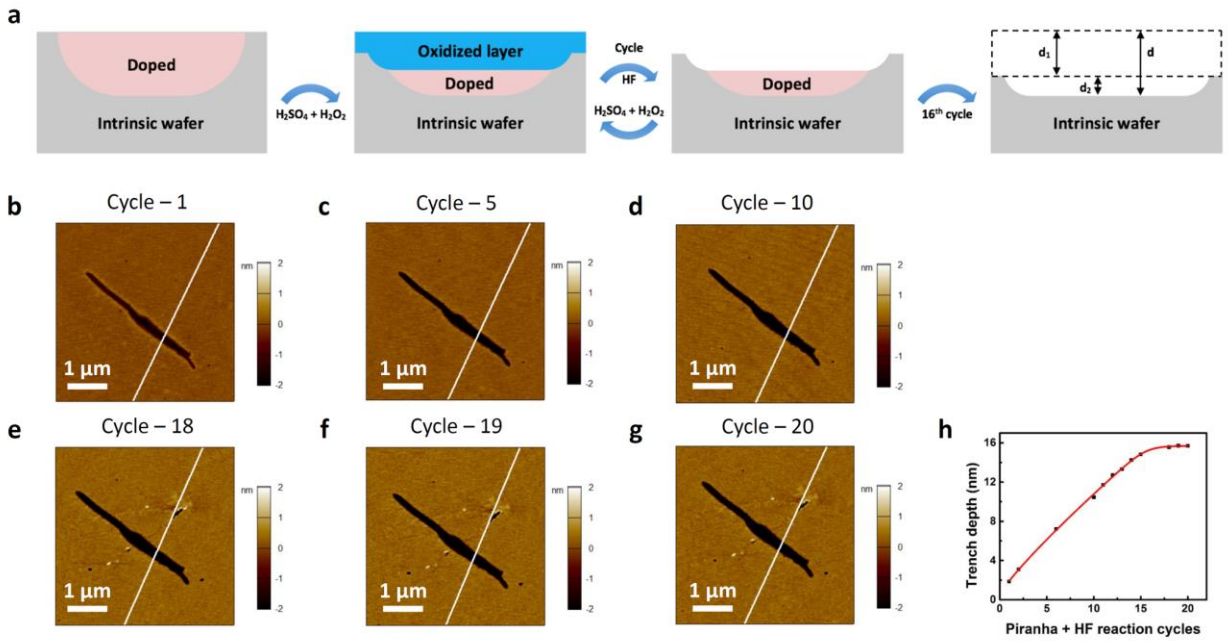

Figure 18. Use reactivity difference to obtain the doping depth. a, Schematic diagram for the piranha and HF reaction cycles (*d* is the doping depth, d_1 is the thickness of Si etched away from the un-doped area, and d_2 is the depth of the trench measured in the AFM image). b-g, AFM images of the doped sample (10s of RTA) at the same position after different reaction cycles: 1, 5, 10, 18, 19, 20. White lines indicate locations where the trench depths were measured. h, A plot of the measured trench depth versus the number of reaction cycles.

2.4.4 Silicon consumption after the piranha solution and the HF solution

In each reaction cycle (piranha and HF treatment), a ≈2 nm SiO_2 layer was generated and eliminated (characterized by ellipsometry). Using the thickness of the resulting SiO_2 and the below equation, we calculated the thickness loss of the Si layer after each cycle:

$$Thickness\ of\ Si = Thickness\ of\ SiO_2 \times \frac{Molar\ volume\ (Si)}{Molar\ volume\ (SiO_2)}$$

Eq. 1

2.4.5 Theoretical calculations for the doping depth

A model of the constant-dose condition was used here; the doping depth can be calculated using the following equation:

$$x = \sqrt{4Dtln\frac{N_0}{N_B}}$$

Eq. 2

x: Doping depth

D: Diffusivity (1.27 x 10^{-14} cm^2/s)

t: Diffusion time (10 or 30 s)

N_0: Surface dose

N_B: Background dose (5.7 x 10^{11} cm^{-3})

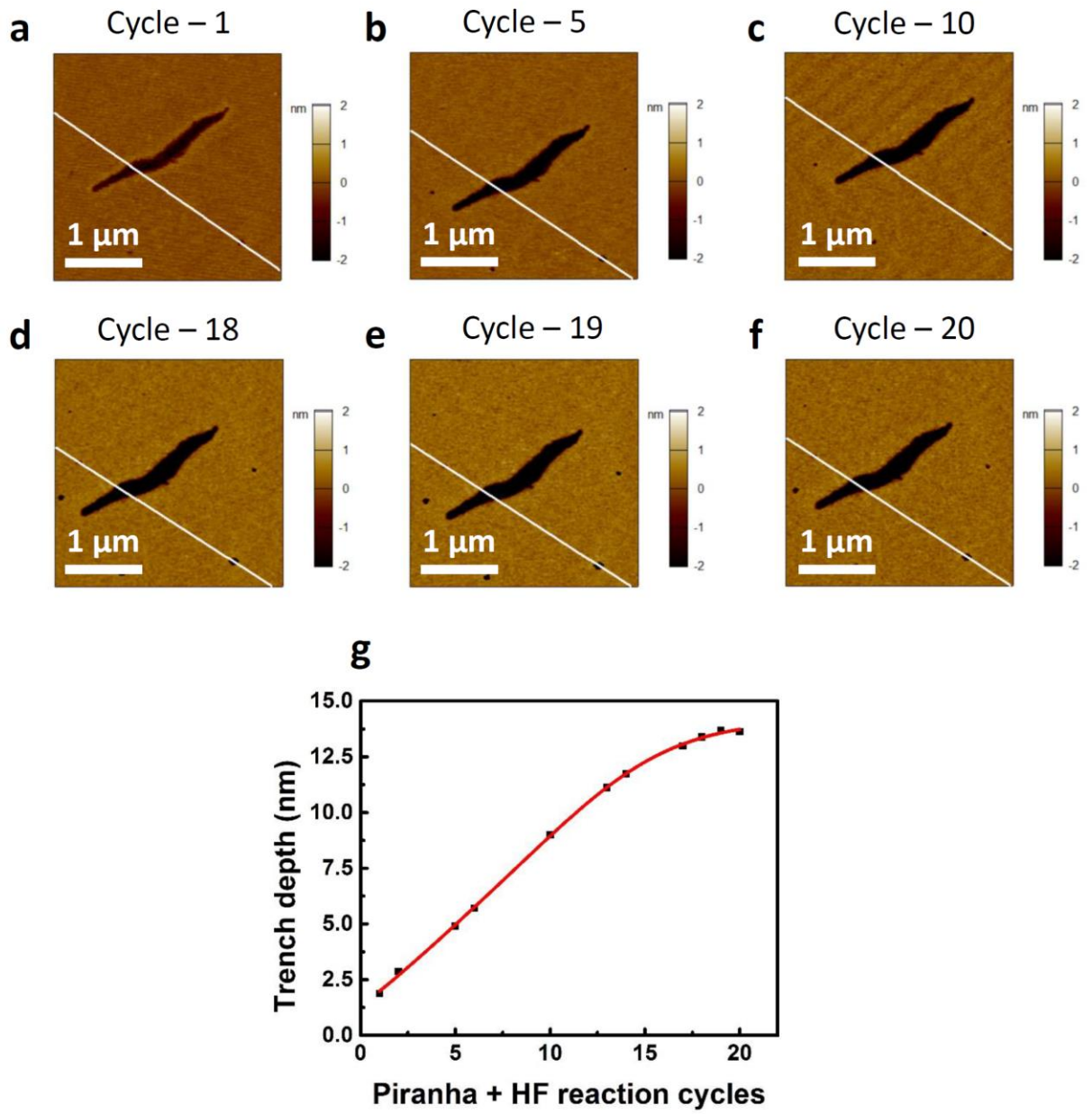

Figure 19. Use reactivity difference to obtain the doping depth of another doped region. a-f, AFM images of the doped sample (10s of RTA) at the same position under different reaction cycles: 1, 5, 10, 18, 19, 20. White cross sections indicated locations where the trench depths were measured. g, The measured trench depth *vs* the number of reaction cycles.

2.4.6 Fabrication and characterization of field effect transistor

We carried out nanoscale measurements to obtain the electrical properties of an individual doped area of Si. Our previous characterization implied that each DNA nanowire structure produced a doped region in Si in the shape of a half-cylinder of 30 nm in radius and 2 - 20 μm in length, that is, a doped 'nanowire' embedded in the intrinsic Si wafer. We have patterned electrodes onto an individual doped nanowire to conduct electrical measurements. In this case, the preparation of the sample is slightly different from the previous method to eliminate the parasitic contact resistance from the field effect transistor (FET) electrodes with the intrinsic Si substrate. We used an intrinsic wafer with a 30 nm SiO_2 layer; the oxide layer helps to eliminate unintentional doping of the background region during the RTA.[140-141] After the deposition of DNA nanotubes (Figure 20a), we used a previously published vapor-etching method[58, 63] to completely remove the SiO_2 only under DNA materials (Figure 20b) and treated the substrate with UV/O_3. We then coated the whole wafer with a thin Al_2O_3 layer using ALD, followed by RTA to initiate dopant diffusion. Finally, we removed the Al_2O_3 layer by H_3PO_4 and cleaned the surface using piranha solution to remove any remaining phosphate residues (Figure 20c). The piranha cleaning also oxidized the silicon surface to produce a thin oxide layer (thickness: ≈0.5 nm, Figure 20d).

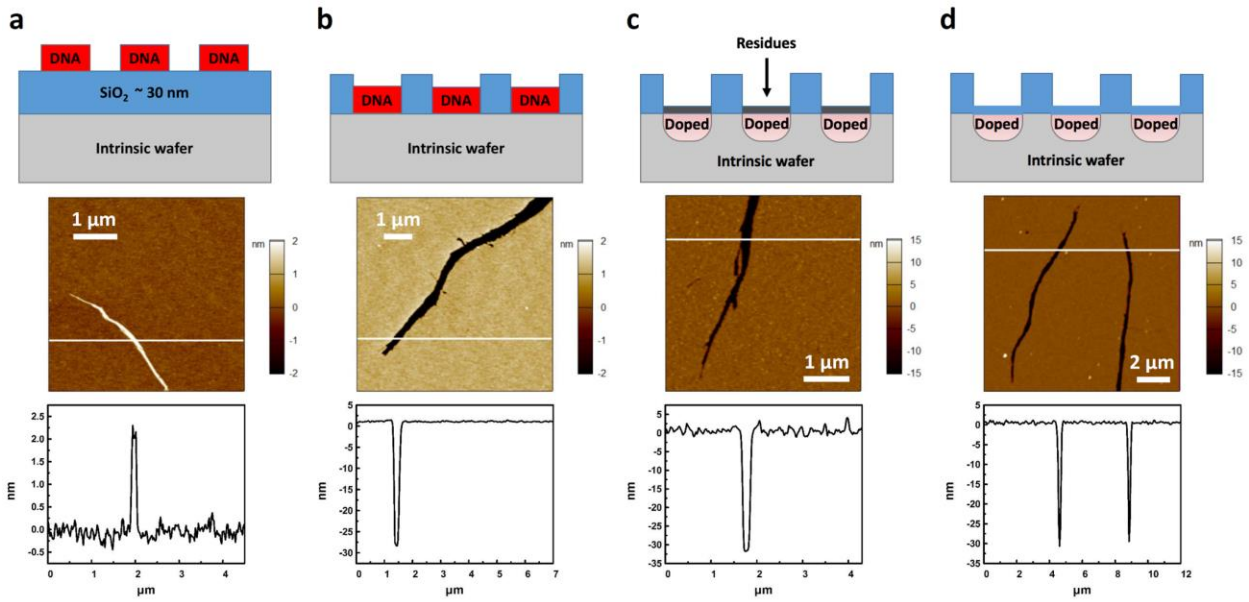

Figure 20. Schematic diagrams, AFM images and cross sections of DNA-doped Si wafer for FET fabrication. a, Deposition of DNA nanotubes onto a Si/SiO_2 substrate. b, Selective removal of the SiO_2 underneath DNA template via DNA-enhanced etching of SiO_2. c, Introduction of the dopant atoms and removal of the Al_2O_3 capping layer. d, After cleaning the surface with piranha solution.

We used EBL to pattern gate and channel electrodes on a single nanowire-like doped region (Figure 21a-c) for determining the channel resistance and hence doping concentration via four-point probe measurements. A thin HfO_2 layer (20 nm) was used as the gate dielectric. Figure 21b, c show the optical micrographs of the finished device, and Figure 21d is a photograph of the device after wire bonding to an external chip carrier.

From the nanoscale four-point probe measurements, we obtained a resistance of 23 kΩ for the doped 'nanowire' area, with contributions from the 'nanowire' doped region and the un-doped background; this value is much smaller compared to the one measured on a control device (904 kΩ) patterned on an intrinsic, none-doped region of the wafer (Figure 21e). From the measured

resistance and the geometry of the doped region, we estimated that the resistivity of the doped region was 0.0079 Ω·cm and the dopant concentration was 6.4×10^{18} cm^{-3} (see Eq. 4 for the calculation). Figure 21f is the transfer characteristic of the FET, showing an increase of channel current responding to an increase of the gate voltage. This gate response indicates that the channel is *n*-doped, as expected from doping by phosphorous atoms in DNA. The weak gating effect here (Figure 21f) indicates degenerate doping across the entire length of the 'nanowire' region.[21]

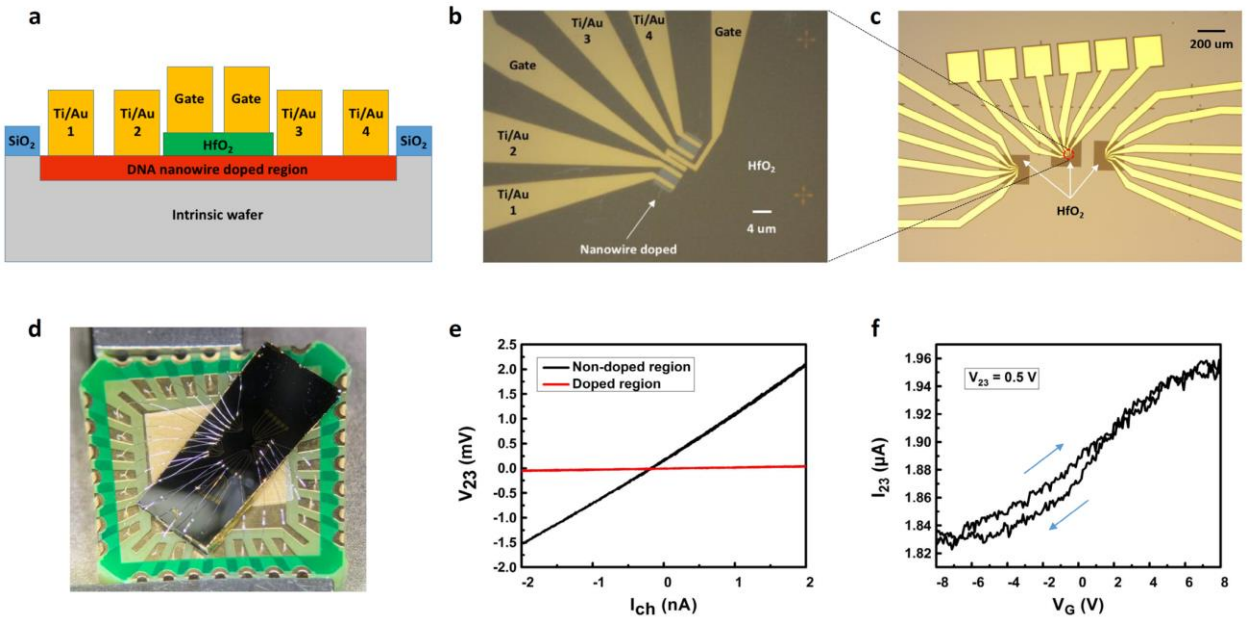

Figure 21. Fabrication of FET from a single 'nanowire'-shaped doped region. a, Schematic diagram of the cross section of the FET. b, c, Optical image of the patterned electrodes. d, Photograph of the device after wire bonding. e, I-V curves of four-point probe measurement of resistance of the 'nanowire' doped region and non-doped region. I_{ch} represents the current applied in the channel between electrodes 1 and 4. V_{23} represents the measured voltage between electrodes 2 and 3. f, The transfer characteristic of the FET: the channel current as

a function of the gate voltage. Electrode 3 is grounded, V_{23} is the applied voltage between electrodes 2 and 3, and I_{23} represents the current between electrodes 2 and 3.

2.4.7 Estimation of the resistivity of the doped 'nanowire' structure

Since the resistance of the doped 'nanowire' area (R_{total}: 23 kΩ) is much smaller than that of the control device ($R_{background}$: 904 kΩ), the resistance contributed from the pure 'nanowire' doped region could be estimated by the below equation:

$$\frac{1}{R} = \frac{1}{R_{total}} - \frac{1}{R_{background}} = \frac{1}{23\text{k}\Omega} - \frac{1}{904\text{k}\Omega}$$

Eq. 3

Thus, R = 23.6 kΩ. The doped area has a length of 4 μm, a diameter of 400 nm, and a diffusion length of 30 nm was used to estimate the resistivity. Therefore, the resistivity of the doped 'nanowire' region was calculated as:

$$\rho = R \times \frac{A}{l} = 23.6\ \text{k}\Omega \times \frac{\left(400 \times 30 + \frac{1}{2} \times \pi \times 30^2\right) nm^2}{4\ \mu\text{m}} = 0.0079\ \text{ohm} \cdot \text{cm}$$

Eq. 4

ρ: Resistivity

R: Resistance

A: Cross sectional area

l: Length

Using the known relationship between the doping concentration and the resistivity, we estimated the doping concentrations of phosphorus atoms inside the 'nanowire' doped region as 6.4×10^{18} cm^{-3}.

2.5 Conclusions

In summary, we have successfully employed DNA nanostructure to achieve site-specific doping of Si wafer. DNA nanostructures can be utilized as both the etching template as well as the doping source (*via* the phosphorous atoms within the DNA) to produce *n*-type site-specific doping. Our work shows that DNA nanostructures can serve as dual-purpose templates, allowing patterning and doping of Si wafer. Such a strategy offers a new avenue to reduce the complexity and cost of semiconductor nanofabrication. What is more exciting, although not demonstrated here, is the possibility to vary the doping concentration/depth by varying the areal density of DNA (*e.g.*, a DNA nanowire having varying thickness along its length). Doing so will allow single-step, nanoscale spatial control of the doping concentration/depth within a semiconductor device.

More investigations are still needed to realize the application of DNA-based doping in mass production. This includes efficiently generating large-scale DNA templates, accurately depositing metal electrodes with nanometer precision, and developing a manufacturing process compatible with complementary metal-oxide–semiconductor (CMOS) devices. There are already impressive progresses made in these directions. Molecular recognition is an attractive pathway to

obtain increasingly larger size of DNA assemblies;[99] site-specific metallization offers the possibility to integrate electrodes into DNA nanostructure templates.[142] Combining these ideas with our findings, the DNA-based doping strategy may offer a promising solution for future manufacturing of nanoscale electronic devices.

3.0 DNA-patterned SAMs for Site-specific Doping

3.1 Chapter Preface

Materials contained in this chapter were published as a research article in *Advanced Functional Materials*; materials and figures used in this chapter have been reprinted with permission from: *Advanced Functional Materials*, **2021,** *31*(1), 2005940. Copyright © 2021, John Wiley and Sons.

List of Authors: Ruobing Bai, Yanhao Du, Anqin Xu, Yang Hu, John R Erickson, Liwei Hui, Jun Chen, Feng Xiong, Haitao Liu

Author Contributions: R.B., F.X. and H.L. designed and directed the experiments. R.B., Y.D., and Y.H. conducted the experiments. All authors discussed the results. R.B. and H.L. wrote the manuscript with input from all authors.

3.2 Introduction

Site-specific doping of various regions of silicon has been widely used as a technique to fabricate electronic devices.[143-144] This technique enables the conductivity of the semiconductor to be well controlled with the change of the applied voltage.[145] By using site-specific doping to create and other technologies to connect many such controllable semiconductor components, modern microelectronic devices can be constructed.[146] However, to form site-specific doped wafers, the silicon surfaces need to be patterned to define the doped regions.[147] Techniques for patterning

include top-down methods (e.g., photolithography,[148] EBL,[149-150] proximity X-ray lithography[151] and extreme ultraviolet lithography[152]) that modify large pieces of materials to form desired patterns, and bottom-up methods (e.g. molecular self-assembly[153-154]) that build atoms or molecules into desired patterns.

Recently, DNA-based nanofabrication has attracted intensive investigations. In this technique, arbitrarily-shaped DNA nanostructures can be designed and produced precisely by folding a long single scaffold strand DNA with many short staple strands.[69] These designed DNA nanostructures have been shown as powerful tools for producing desired patterns on silicon wafers[64, 155] and locating molecular and nanoscale objects with high spatial precision in a similar fashion.[113, 156] Furthermore, unlike most popular optical lithography, DNA-based nanofabrication does not require high-energy radiation sources and complex optics. Therefore, for applications in large surface patterning, DNA-based nanofabrication will be very cheap and the cost of DNA templates has been estimated to be as low as $\$6/m^2$.[57] By noticing enormous potential of DNA origami as a structural and templating material, we have previously developed a method of applying DNA nanostructures as templates and dopant carriers to achieve the site-specific *n*-type doping.[157]

Here, we demonstrate the use of DNA nanostructures as templates to achieve both *n*-type and *p*-type site-specific doping of silicon wafers. We used DNA nanostructures to pattern doping materials in the form of mixed silane monolayer, which was used to dope silicon wafers in a site-specific fashion. Those doping areas were then characterized by KPFM and CAFM to verify site-specific doping. Finally, the resistance changes after the doping process were investigated by four-point probe measurements to analyze the introduction of dopant atoms. This study provided a way

for both *n*-type and *p*-type site-specific doping using DNA origami, which might be used in future device fabrication.

3.3 Experimental Section

3.3.1 Materials

DNA strands for the nanotube synthesis were purchased from IDT (Sequence: 5'-CCA AGC TTG GAC TTC AGG CCT GAA GTG GTC ATT CGA ATG CCT GAG CGC TCA-3'). Intrinsic silicon wafers [100] with native oxide layers were purchased from WaferPro. 2-diethylphosphatoethyl triethoxysilane (DEPTS) was purchased from Fisher Scientific (Fair Lawn, NJ). Octadecyl trichlorosilane (ODTCS), 2-(chlorodimethylsilyl)-4,4,5,5-tetramethyl-1,3,2-dioxaborolane (CTDB), acetic acid (≥99.7%), sulfuric acid, 2-Amino-2-(hydroxymethyl)-1,3-propanediol (Trizma base or Tris, ≥99.9%), EDTA (≥99%), magnesium acetate tetrahydrate (≥99%), hydrogen peroxide solution (30% wt. % in water), hexane (mixture of isomers), dichloromethane, and ethanol were purchased from Sigma-Aldrich (St. Louis, MO). Nanopure water (18.3 MΩ) was obtained using a water purification system (Barnstead MicroPure Standard, Thermo Scientific, Waltham, MA) and used throughout the entire experiment to prepare chemical solutions and clean experimental samples.

3.3.2 Synthesis and deposition of DNA nanotubes onto the silicon wafer

The DNA nanotubes used here were synthesized according to a previous published paper.[135] Briefly, the DNA single strand was diluted to a final concentration of 2 μM in 10 × TAE-Mg^{2+} buffer (400 mM tris-acetic acid, 10 mM EDTA, 125 mM Mg^{2+}, pH = 8.0). The DNA single strand solution was then slowly cooled from 95 °C to 23 °C in 2 days and stored at 4 °C overnight for the subsequent deposition step. The synthesized DNA sample (10 μL) was then pipetted onto a clean Si/SiO_2 substrate (cleaned by 3/7 (v/v) hydrogen peroxide/sulfuric acid solution for 30 min) and placed in a plastic petri dish without interruption for 40 min. A wet Kimwipe was inserted between the cover and the bottom to maintain moisture inside the petri dish and reduce evaporation. Thereafter, the substrate was dried by a N_2 gas followed by immersion into an 8/2 (v/v) ethanol/water solution for 10 seconds to remove salt impurities (this process was repeated 3 times).

3.3.3 Patterning of mixed monolayers

The Si substrate with the DNA nanotubes was placed inside a 40-mL vial containing a 30 μM solution of ODTCS and hexane for 24 hours. Then the substrate was dried with N_2 gas and the surface was cleaned with pure hexane. We then sonicated the above substrate in deionized water to remove the DNA nanostructures. Thereafter, we placed the Si substrate with ODTCS SAM inside a desiccator for 24 hours; inside the desiccator was a 20-mL vial containing 3 mL of DEPTS. For the growth of CTDB SAM, we immersed the Si substrate with ODTCS SAM into a 1% solution of CTDB in dichloromethane for 24 hours. In both cases, we sonicated the sample in ethanol (or dichloromethane) to remove excess DEPTS (or CTDB).

3.3.4 Site-specific doping

After introducing doping materials into those negative trenches, an AJA orion sputter system was used to sputter a silicon dioxide capping layer with a 50-nm thickness to prevent the diffusion of dopants into the air. The sputtering process was performed at room temperature (24 ˚C) and included three steps: cleaning of the target, ignition of ions and deposition of silicon dioxide. After depositing the capping layer, the samples were subjected to a RTA process using a Surface Science Integration RTA Solaris 75 instrument. In this process, high intensity lamps were used as heat sources to generate a high temperature around 1000 °C in a few seconds, and this high temperature of 1000 °C was held for about 30 seconds. The temperature of the entire system was then slowly cooled down to prevent thermal shock. After the RTA process, the samples were washed with 1% HF to remove the silicon dioxide capping layer. A hot piranha solution (3/7 (v/v) hydrogen peroxide/sulfuric acid solution) was also used to wash away any possible residues on the surface for 30 min. Finally, the oxide layer produced during the piranha washing process was removed using HF (1%) and the substrate was thoroughly washed with water and dried with a N_2 gas.

3.3.5 AFM characterization

Throughout the study, surface morphologies of the samples were monitored by tapping mode AFM using an Asylum MFP-3D Atomic Force Microscope with HQ:NSC15/Al BS AFM probes (325 kHz, 40 N/m) purchased from MikroMasch (NanoAndMore USA). Current maps were obtained by using the same instrument in contact and electrical mode with Budgetsensors ContE-G tips (13kHz, 0.2 N/m). Potential maps of the samples were monitored using tapping mode

with Budgetsensors Tap 190E-G tips (190 kHz, 48 N/m). The KPFM measurements were performed in an amplitude-modulated system by using a two-pass technique. The first pass was to determine the topography of the surface and the second pass was to measure the CPD of the sample surface. For the second pass, the separation distance was varied from 10 nm to 30 nm and the applied tip voltage was 3 V. All images were analyzed by Igor Software (Version 6.3.7.2) as part of the Asylum Research package.

3.3.6 Four-point probe resistance measurements

The four-point probe setup was made of four equally spaced tungsten metal tips. The diameter of the metal needle was 200 μm and the distance between the adjacent two metal tips was 1 mm. During the experiment, the metal tips were connected to a Model 2614B Keithley source meter. The voltage drop was measured across the two inner probes by passing a linearly sweeping current through the two outer probes. The slope of the I-V plot was then used to determine the sample resistance.

3.3.7 Water contact angle measurements

The VCA optima XE contact angle system was used to measure the water contact angle at 24 ˚C. The size of each water droplet was 2 μL. The images of water droplets were taken by a charge-coupled device camera. Three images were taken for each substrate and the average including the standard deviation of the mean was calculated.

3.4 Results and Discussion

3.4.1 Achievement of both *n*-type and *p*-type doping using DNA-patterned SAMs

We used DNA templates to form mixed SAMs to achieve site-specific delivery of dopants.[60] This approach allows us to achieve both *n*- and *p*-type doping. Figure 22 shows the steps of preparing the site-specific doped sample. First, we deposited the DNA templates onto a Si substrate to define the areas to be doped. This substrate was then immersed in an ODTCS (which does not contain phosphorous or boron atom) solution to grow ODTCS-SAMs on and around the DNA materials. After sonicating the treated substrate in deionized water, we removed the DNA templates and the ODTCS-SAMs overlying the DNA templates, which exposed the underlying Si surface for the subsequent introduction of the doping materials. The newly exposed Si surface was then reacted with different doping materials such as DEPTS (phosphorous-containing) and CTDB (boron-containing) to form SAMs in these regions. After that, we sputtered a SiO_2 capping layer onto the surface of the entire substrate followed by RTA process to initiate the dopant diffusion.

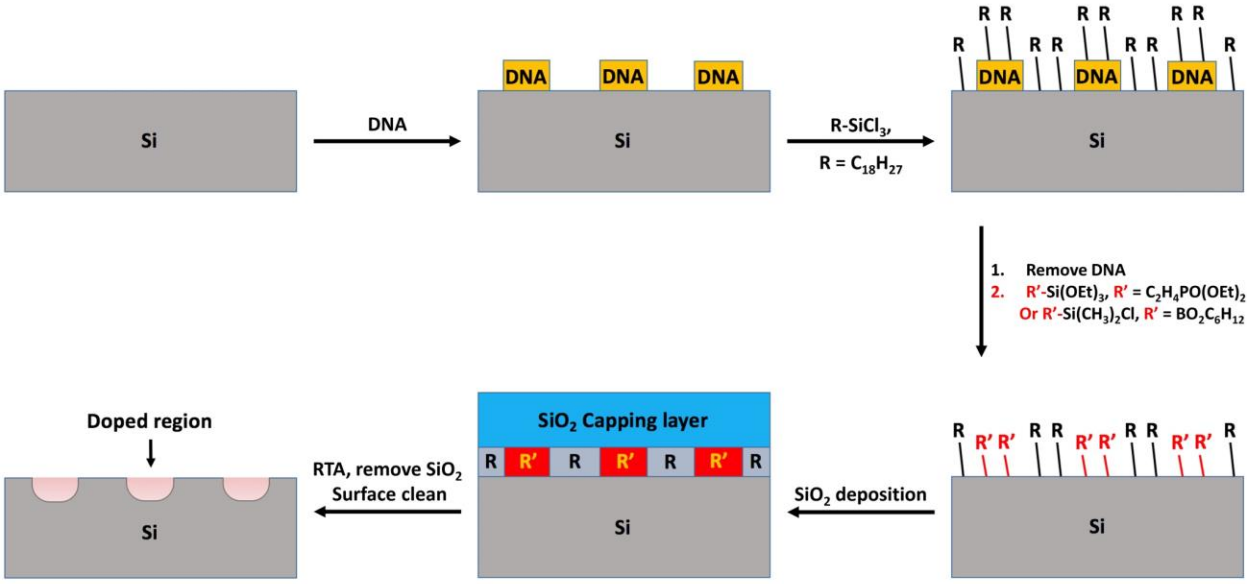

Figure 22. Schematic diagram of using DNA-patterned SAMs to prepare both *n*-type and *p*-type site-specific doped silicon wafers.

3.4.2 Confirmation of the formation of mixed SAMs containing dopant atoms

To verify the successful growth of the mixed SAMs, AFM were first used to record the topography of the sample during each step at the same location. A large aggregate of DNA nanostructure was chosen here because it is easy to locate such features in subsequent AFM imaging. As shown in Figure 23a, b after immersing the DNA-templated substrate in ODTCS solution, the height of DNA nanotubes changed from 2.0 nm to 1.8 nm. The change of the height of these DNA nanotubes was consistent with the idea that C_{18}-SAMs grow both on the wafer substrate and DNA nanotubes. The height variation of the background in Figure 23b was around 0.2 nm, which means that C_{18}-SAMs was relatively uniform. After removing the DNA nanotubes from the substrate, a negative tone pattern with 0.8 nm depth was obtained (shown in Figure 23c).

These negative tone patterns indicated that those specific sites were successfully exposed for the following reactions. The same process and results were also seen for another intrinsic wafer (prepared for doping with boron atoms) (Figure 23d-f).

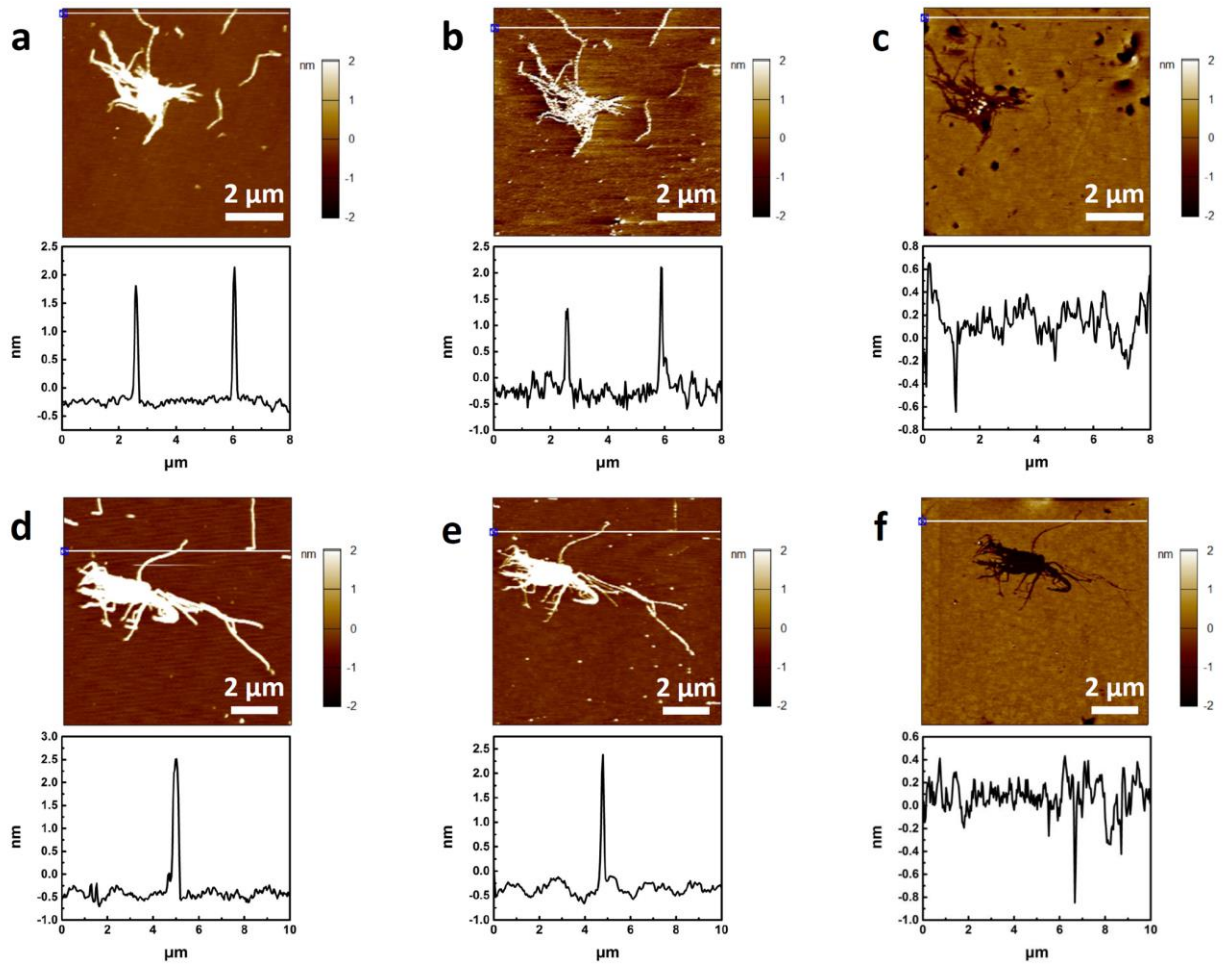

Figure 23. DNA-templated growth of patterned ODTCS SAMs. a, d, AFM images and cross sections of DNA nanotubes deposited onto a silicon wafer. b, e, After growing ODTCS SAMs on the sample. c, f, After sonicating the sample in deionized water to remove DNA nanotubes. Two samples were shown. For each sample, the AFM images were performed on the same location.

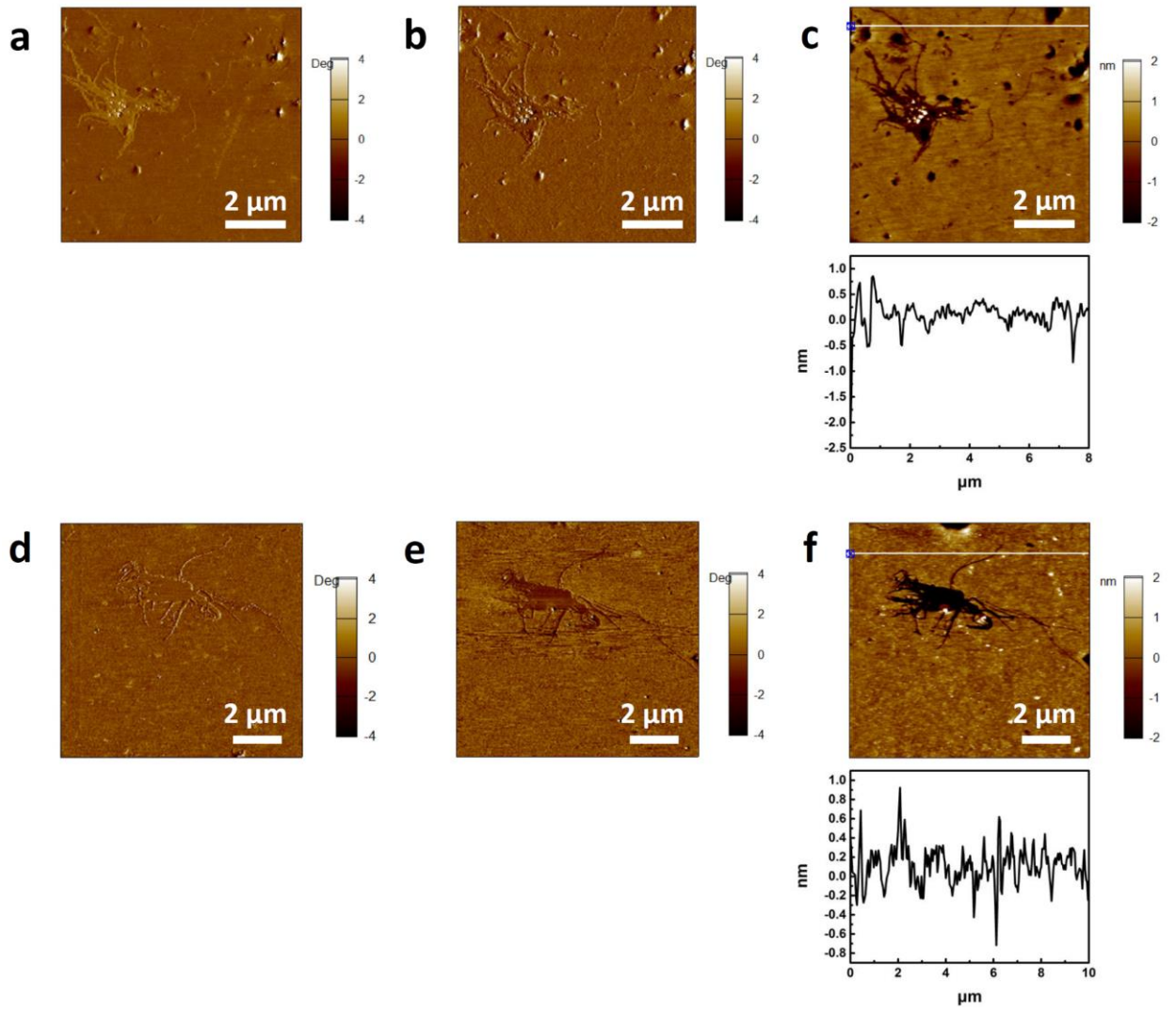

Figure 24. DNA-templated growth of mixed SAMs. a, d, Phase images of DNA nanotubes patterned C_{18}-SAMs on a SiO_2 substrate. The DNA nanostructures were removed to produce negative trenches. b, e, Phase images after backfilling of DEPTS and CTDB SAMs. c, f, Corresponding AFM height images and cross sections.

To introduce doping materials onto those specific locations, the negative-tone patterned substrates were reacted with either the vapors of DEPTS or immersed in 1% CTDB solution. The DEPTS and CTDB molecules were filled onto those trenches, thereby providing phosphorus and

boron atoms for the next diffusion step. The height images after the introduction of doping materials were shown in Figure 24c, f; however, since the chain lengths of these doping materials were quite small, the height image contrast after doping did not change much from the image before doping. Therefore, it was hard to track this reaction using only topography images. AFM phase images (Figure 24a, b, d and e) showed some minor changes after introducing doping materials. Although this small change might be the indication of the change of compositions inside the negative trenches, the change was too small to draw a conclusion. Therefore, alternative methods need to be used to prove this introduction of doping sources. (see below).

The wettability of the substrate was also tested to aid in verifying the successful growth of SAMs onto the substrate. As shown in Table 1 and Figure 25, after growing ODTCS SAMs onto DNA nanotubes and the silicon wafer, the water contact angle changed from 13.2° ± 1.2° to 114.2° ± 1.5°. This change from a hydrophilic surface to a hydrophobic one indicated the successful growth of ODTCS SAMs. After removing DNA templates, the water contact angle has decreased from 114.2° ± 1.5° to 61.6° ± 3.0°. This observation was reasonable because of the exposure of hydrophilic silicon wafers (≈40%) to those negative trenches. After the introduction of DEPTS and CTDB doping materials onto these hydrophilic sites, the water contact angles have increased up to 73°. This result suggested the successful deposition of doping materials of DEPTS and CTDB onto those specific trenches. The combination of changes of water contact angle and AFM images demonstrated the successful operation at each step.

Table 1. Water Contact Angle Values for Different Samples.

Sample	Water Contact Angle (°)
1. Clean intrinsic wafer	17.6 ± 0.8
2. DNA nanotubes on the intrinsic wafer	13.2 ± 1.2
3. ODTCS grown on the intrinsic wafer	114.2 ± 1.5
4. CTDB grown on the intrinsic wafer	54.1 ± 0.2
5. DEPTS grown on the intrinsic wafer	33.0 ± 0.6
6. ODTCS on the wafer with DNA	114.3 ± 0.7
7. ODTCS on the wafer (DNA removed)-1	61.6 ± 3.0
8. ODTCS on the wafer (DNA removed)-2	54.9 ± 0.9
9. ODTCS-CTDB on the wafer -1	73.2 ± 3.1
10. ODTCS-DEPTS on the wafer-2	63.4 ± 0.3

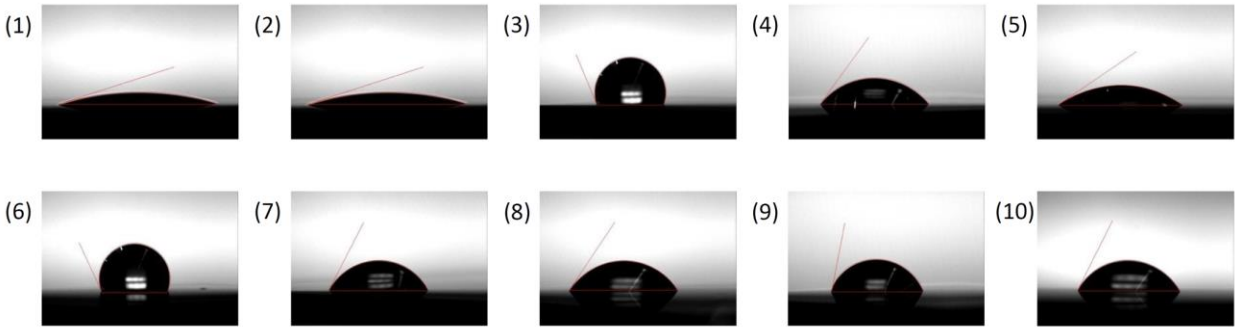

Figure 25. Water contact angle images of samples 1-10 in Table 1. Red lines indicate the measurements of the water contact angle.

3.4.3 Verification of *n*-type and *p*-type site-specific doping

To study the change in the electrical property of the sample surface, CAFM was used to characterize these samples. During our characterization, a negative sample voltage was applied. Therefore, a lower current corresponded to a higher conductivity. As can be seen from Figure 26, the morphologies of the current images consisting of higher conductivities were very similar with those of the topographic images, indicating that the doping process did occur at the specific and designed sites. We attributed the negative height pattern observed in the phosphorus-doped wafer to solid-state reactions between the Si and SAMs precursor during the doping process.[158] We have also noticed that it is not possible to use data here to determine the conductivities of two samples due to many complexities, including wear of the contact tip coating caused by multiple scans and the variations of electrical contact between the tip and the sample.[159]

We also used KPFM to characterize the DEPTS and CTDB doped silicon wafers. In these experiments, we imaged the same location before and after doping. We observed differences in the potential differences between the doped region and the background Si and the pattern in the surface potential map closely resembled that of the original DNA nanostructure (Figure 27a-f). These results indicate the success of site-specific dopant delivery in both cases. Moreover, for the Si wafer doped with phosphorus atoms (*n*-type), the surface potential of the doped region is larger than that of the background wafer. For the boron-doped silicon wafer (*p*-type), the surface potential of the doped region is smaller than that of the background wafer. The opposite change of surface potential seen in the phosphorus-doped and boron-doped samples is expected because *n*- and *p*-type doping shifts Fermi level in opposite directions.[160] It is worth noting that the differences in surface potential could be affected by the adsorption of water, among other factors. As a result, these values may not directly correlate with the built-in potential difference of the sample.[161]

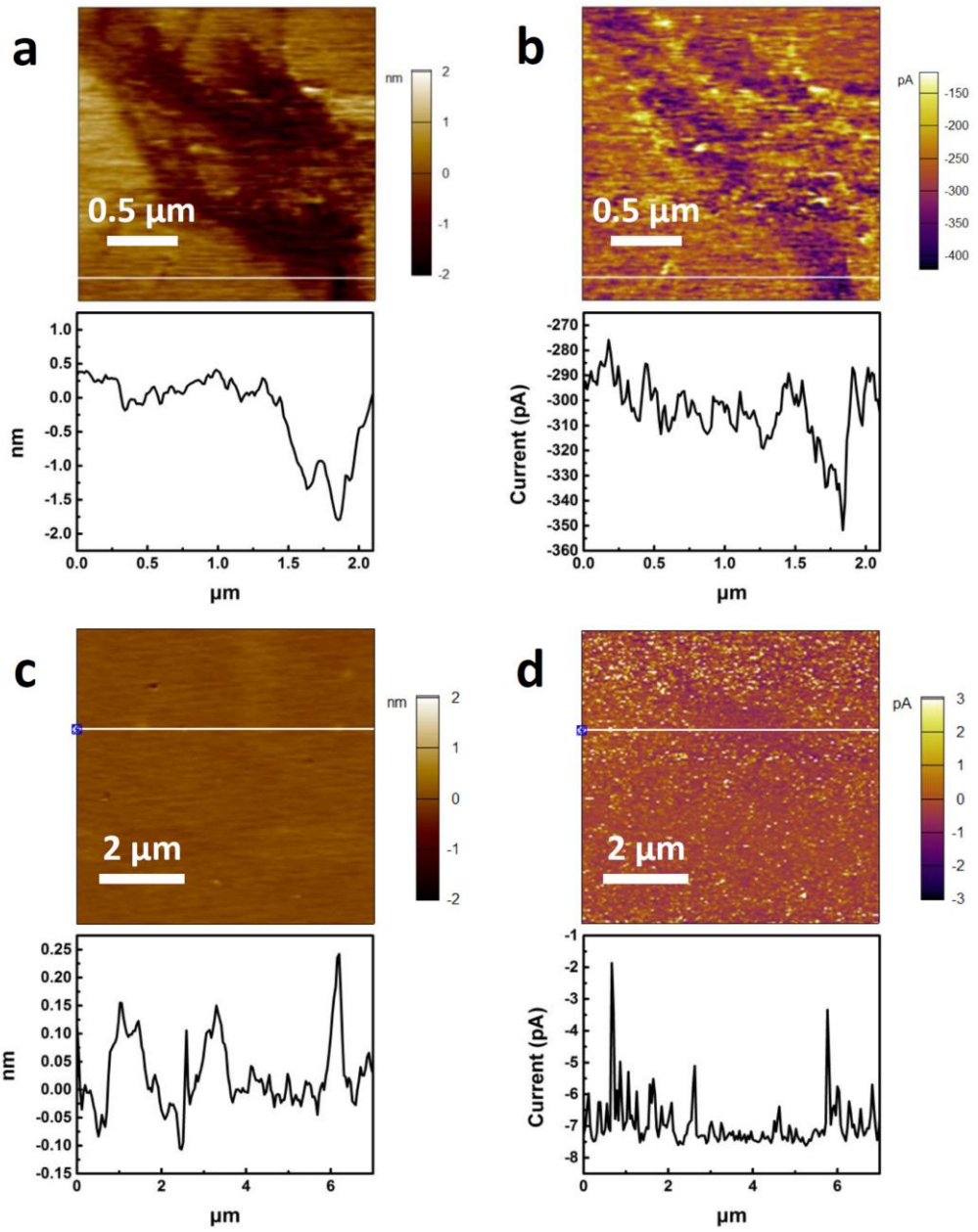

Figure 26. CAFM images and cross sections for the site-specific doped wafers using DNA-patterned SAMs. a, b, Height and current images of the phosphorus-doped wafer (sample voltage was -9 V). c, d, Height and current images of the boron-doped wafer (sample voltage was -1 V). The poor contrast of the conductivity may come from the wear of the contact tip coating caused by multiple scans and the variations of electrical contact between the tip and the sample.

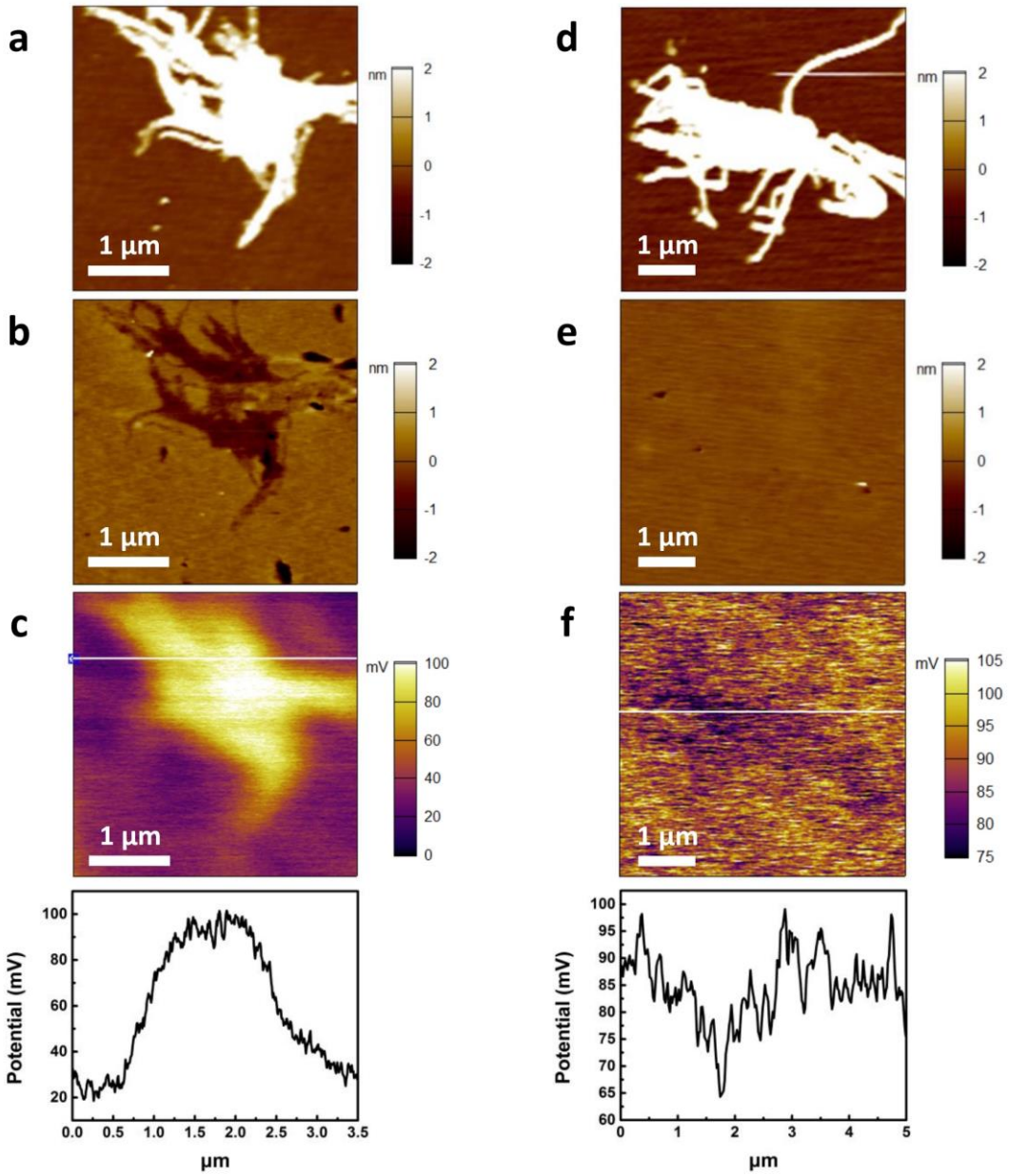

Figure 27. AFM and KPFM characterization of the site-specific doping of Si wafers using DNA-patterned SAMs. a, d, AFM images of the DNA materials deposited on intrinsic Si wafers. b, c, Height and surface potential images of the DEPTS-doped wafer at the same location. e, f, Height and surface potential images of the CTDB-doped wafer at the same location. White lines indicate the cross sections where the below graphs are obtained. All doped wafers tested here were processed by RTA at 1000 °C for 30s.

We also conducted macroscopic electrical measurements on the surfaces of different samples to obtain their resistances by using four-point probe measurements. A schematic diagram of the setup is shown in Figure 28 (*t* is the effective thickness and the distance between the two metal tips is 1 mm). As can be seen from measured results in Table 2, the resistance of the doped wafer was significantly reduced compared with the intrinsic wafer. It can also be seen that the resistance of the site-specific doped wafer with phosphorus or boron atoms was between that of the intrinsic wafer and the wafer doped with uniform phosphorus-contained self-assembled monolayers (PO-SAMs) or boron-contained self-assembled monolayers (BO-SAMs). In addition, it was observed that the resistance of the phosphorus doped wafer was much larger than that of the boron doped sample. This observation is also consistent with KPFM measurement. Overall, the decrease in resistance after doping further confirmed the successful introduction of doping materials into the wafer.

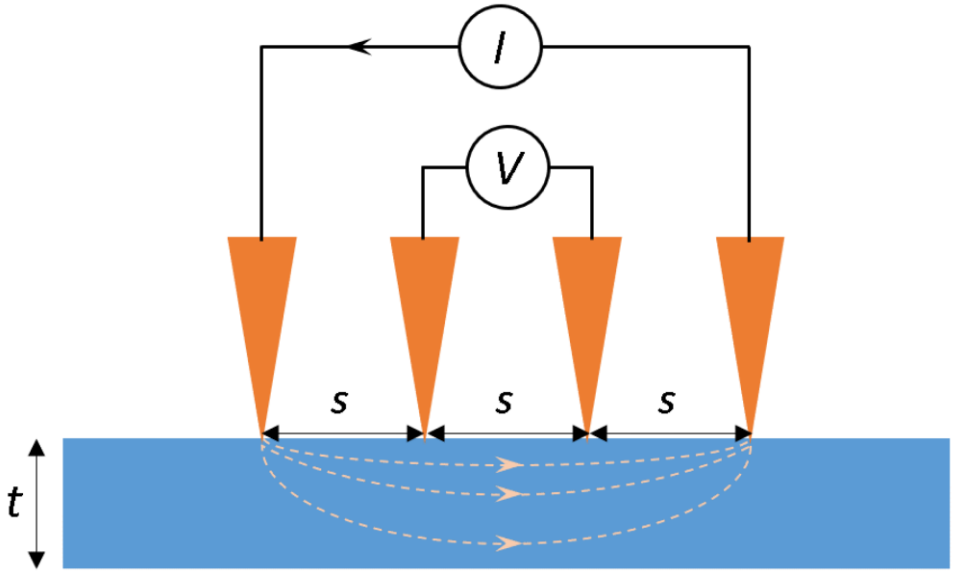

Figure 28. Schematic of the collinear four-point probe measurement with equidistant contact spacing.

Table 2. Resistances of Different Samples Based on the Four-point Probe Measurements.

Sample (Surface Coverage)	Resistance (Ω)
Intrinsic wafer	116,555 ± 4,494
Wafer doped with C_{18}-SAMs	1,782 ± 83
Wafer doped with PO-SAMs (50%)	383 ± 16
Wafer doped with PO-SAMs (100%)	87 ± 11
Wafer doped with BO-SAMs (30%)	867 ± 61
Wafer doped with BO-SAMs (100%)	740 ± 52

3.5 Conclusions

In summary, we have shown that DNA nanostructures can be used as templates to pattern mixed SAMs to achieve site-specific delivery of both *n*- and *p*-type dopants, and then help form *n*-type and *p*-type site-specific doped Si wafers. Similar morphologies found in KPFM potential map and CAFM current map indicated the successful introduction of doping atoms in the region defined by the DNA template. As expected, opposite CPD values were also found in the samples doped with phosphorus atoms and boron atoms. Moreover, the increase in conductivity in the doped samples shown in the electrical measurements further indicated the occurrence of site-specific doping. Our work points out a way to couple doping with DNA-based fabrication to produce both *n*-type and *p*-type site-specific doped Si wafers, which offers a new avenue to reduce the complexity and cost of semiconductor nanofabrication.

4.0 DNA-based Doping to Fabricate PN Diodes

4.1 Chapter Preface

Materials contained in this chapter are in preparation for publication as a research article.

List of Authors: Ruobing Bai, Yihan Liu, Bomin Zhang, Feng Xiong and Haitao Liu

Author Contributions: R.B. and H.L. designed and directed the experiments. R.B., Y.L., and B.Z. conducted the experiments. All authors discussed the results. R.B. and H.L. wrote the manuscript with input from all authors.

4.2 Introduction

As the demand for high performance of electronic devices in terms of power, speed and density continues to grow, there is an increasing need for new technologies to produce electronic devices.[34, 162] Since the development of today's semiconductors is to continuously reduce the size of key features and reduce the overall manufacturing cost,[54, 163] the development of technology compatible with high-resolution patterning, low-cost, and large-scale fabrication to produce electronic devices will cause great interest.

To achieve high-resolution patterning for the fabrication of electronic devices, the industry usually chooses to use a photolithography process.[164] Although this method is very successful and widely used in industry and research, photolithography requires a clean environment, expensive mask and equipment, which results in high costs for the manufacturing process.[165] In addition, if the device design requires the use of different doping types or different doping concentrations in

different regions, it will require multiple photolithography and doping steps, which further increases the manufacturing cost and complexity.[166-167]

We have previously reported the use of DNA nanostructures to achieve site-specific doping. This DNA-based doping strategy could help reduce lithography and doping steps in semiconductor manufacturing because DNA nanostructures have the potential to deliver different types and/or dosages of dopants in one doping step.[168] Previous work mainly used DNA nanostructures as templates and doping sources to achieve high-resolution patterning and deliver dopants to specific locations. Here, we try to fabricate PN diodes through similar methods to realize practical applications in the production of electronic devices based on DNA nanostructures. We also proposed a method to simplify the device manufacturing process using metal-modified DNA. The electronic devices produced here through DNA nanostructures have many advantages. First, DNA-based nanofabrication has the advantages of both top-down (designed pattern) and bottom-up (scalability/low cost) fabrication methods.[31, 169] Second, the cost of using the DNA template for 2D patterning is less than $\$1/m^2$, which provides the potential for high-resolution patterning in a large scale.[57] Many previous papers have reported the use of DNA nanostructures to achieve high-resolution patterning on different substrates (such as SiO_2, Si, polymers, graphite and self-assembled monolayers).[58-63] Utilizing the advantages of high-resolution patterning, low cost, and large-scale manufacturing of DNA nanostructures, here we demonstrated the use of self-assembled DNA nanostructures to fabricate electronic devices in short steps, thereby eliminating photolithography and reducing excess doping and electrode deposition steps. Our method saves a lot of efforts for manufacturing electronic devices, and provides the possibility to produce high-resolution electronic devices in a large scale at low cost.

4.3 Experimental Section

4.3.1 Materials

p-type silicon wafers [100] with native oxide layers (1 – 10 Ohm·cm, double side polished) were purchased from University Wafer. DNA strands for the synthesis were purchased from IDT. 5' thiol-modified 10 poly T was purchased from Eurofins. 5 nm Au nanoparticles were purchased from Fisher Scientific. Sulfuric acid, 2-Amino-2-(hydroxymethyl)-1,3-propanediol (Trizma base or Tris, ≥99.9%), EDTA (≥99%), acetic acid (≥99.7%), magnesium acetate tetrahydrate (≥99%), hydrogen peroxide solution (30% wt. % in water), Bis(*p*-sulfonatophenyl)phenylphosphine dihydrate dipotassium salt (BSPP), sodium chloride, methanol and ethanol were purchased from Sigma-Aldrich (St. Louis, MO). Nanopure water (18.3 MΩ) was obtained using a water purification system (Barnstead MicroPure Standard, Thermo Scientific, Waltham, MA) and used throughout the entire experiment to prepare chemical solutions and clean experimental samples.

4.3.2 Synthesis and deposition of DNA nanotubes and DNA-Au-DNA onto the silicon wafer

The synthesis of DNA nanotubes here were based on previous published paper.[61, 135] Briefly, we diluted the DNA single strand in 10 × TAE-Mg^{2+} buffer (400 mM tris-acetic acid, 10 mM EDTA, 125 mM Mg^{2+}, pH = 8.0) to a final concentration of 2 μM. The DNA single strand solution was then slowly cooled down from 95 °C to 23 °C in 2 days and stored at 4 °C overnight for the subsequent deposition step. The synthesis of DNA-Au-DNA structure here was first inspired by the previous published paper.[99] In short, we modified their four DNA origami short staples, and added 10 additional A tails to all the short staples in the middle 200 nm part for the

connection of gold nanoparticles in the middle part in the following step. We then mixed the DNA scaffold strand and staple strands for each design together to target concentrations of ~2 nM and ~75 nM, respectively, in 1 × TAE-Mg^{2+} buffer. Each origami mixture (scaffold + corresponding staples) was annealed separately from 90 °C to 50 °C (with a rate of -1 °C/min), mixed together at 50 °C, and kept at 50 °C for 12 hr, then cooled to 20°C at a rate of -5 °C/hr to form a long DNA structure. We then reacted the long DNA structure with a synthetic 5 nm Au nanoparticle-DNA conjugate in solution, which was synthesized in the same way as the previous paper[142] (check their paper for details) to form DNA-Au-DNA structure. A Si/SiO_2 substrate was cleaned by piranha solution (3/7 (v/v) hydrogen peroxide/sulfuric acid solution) for 30 min (*Warning*: piranha solution reacts violently with organic compounds, please handle in a fume hood and use proper personal protection equipment). The clean substrate was placed in a furnace at 900 degrees for 3 hours to grow SiO_2 with a suitable thickness, and the surface of the substrate was cleaned again by piranha solution. The prepared DNA sample (10 μL) was then pipetted onto the cleaned wafer and placed in a plastic petri dish. We then inserted a wet Kimwipe between the lid and the bottom to maintain high humidity inside the petri dish and reduce the evaporation. After 40 minutes of undisturbed incubation, we dried the Si substrate with N_2 gas, then immersed it into an 8/2 (v/v) ethanol/water solution for 20 seconds to remove salt impurities and then dried the substrate with N_2 gas again. This washing and drying process was repeated 3 times.

4.3.3 Selective removal of SiO_2 under DNA nanostructures

The removal process was operated based on the previous paper.[63] Briefly, we exposed the DNA-deposited Si/SiO_2 substrate to HF vapor to remove all SiO_2 under the DNA nanostructure, while leaving a certain thickness of SiO_2 in the area where there is the Au-DNA or background.

The remaining SiO_2 was measured by ellipsometry, and the thickness of the etched trench in the DNA region was measured by AFM. These two measurements were combined and compared to ensure that all SiO_2 under the DNA was completely removed.

4.3.4 Site-specific doping

The etched sample was subjected to the UV/O_3 for 3 hours to purify the phosphorus dopants. Then the sample was capped by a 20 nm Al_2O_3 by ALD to prevent the diffusion of dopants to the air. After depositing the capping layer, the samples were subjected to the RTA process using a Surface Science Integration RTA Solaris 75 instrument. In this process, the temperature rose to the desired temperature within 20 seconds and this temperature was maintained 10s. Then the temperature of the entire system was cooled down to 150 °C within 3 minutes. After the RTA treatment, we used 2 M H_3PO_4 to remove the capping layer and used a hot piranha solution (for 60 minutes) to wash away any residue on the surface. Finally, the sample was washed with deionized water and dried with N_2 gas.

4.3.5 AFM and scanning electron microscopy (SEM) characterization

Throughout the study, AFM topography images were acquired in tapping mode using an Asylum MFP-3D Atomic Force Microscope with HQ:NSC15/Al BS AFM probes (325 kHz, 40 N/m) purchased from MikroMasch (NanoAndMore USA). SEM images were obtained by a ZEISS Sigma 500 VP microscopy.

4.3.6 Device fabrication and electrical measurements

The dielectric layer and metal contacts were patterned by EBL using a Raith e-Line system. A 20 nm of HfO_2 layer was deposited by ALD using a Cambridge Nanotech Fiji ALD system, covering all the surfaces where the metal would lay down except for the small area where the metal contacted with the nanowire. The metal contacts were 2 nm of Ti and 60 nm of Au evaporated using a Plassys electron beam evaporator. Finally, the metal contacts were wire-bonded to a chip carrier using aluminum wires. The device was then tested by a Keithley 4200A-SCS Parameter Analyzer in air at room temperature.

4.4 Results and Discussion

4.4.1 Preparation of PN diodes using DNA-based doping

We used DNA nanowires to form *n*-type site-specific doped regions on *p*-type silicon wafers, thereby forming multiple vertical PN junctions. The method for forming *n*-type site-specific doping here is the same as our previously reported DNA-based site-specific doping method. First, we deposited self-assembled DNA nanotubes on a *p*-type wafer with 40 nm SiO_2 (Figure 29a).[157] Each micrometer-long DNA nanotube was self-assembled from one short DNA single-strand containing four palindromic segments. These self-assembled DNA nanotubes have a width of *ca.* 70 nm and a height of *ca.* 2.0 nm. After successful deposition, we exposed the sample to HF vapor to remove all SiO_2 under the DNA material, while leaving about 30 nm SiO_2 in the background to eliminate unintentional doping of the background region during the RTA. (Figure

29b). After etching, the SiO_2 thickness and groove depth on the sample surface are both ≈30 nm (measured by ellipsometry and AFM), indicating that the SiO_2 under the DNA has been completely removed. After that, the sample was treated with UV/O_3 to remove the organic components in the DNA, and then covered with 20 nm Al_2O_3 to prevent the dopant from diffusing into the air. Then the sample was treated with RTA for 10 seconds, washed with H_3PO_4 to remove the capping layer, and washed with piranha solution to complete the formation of multiple vertical PN junctions.

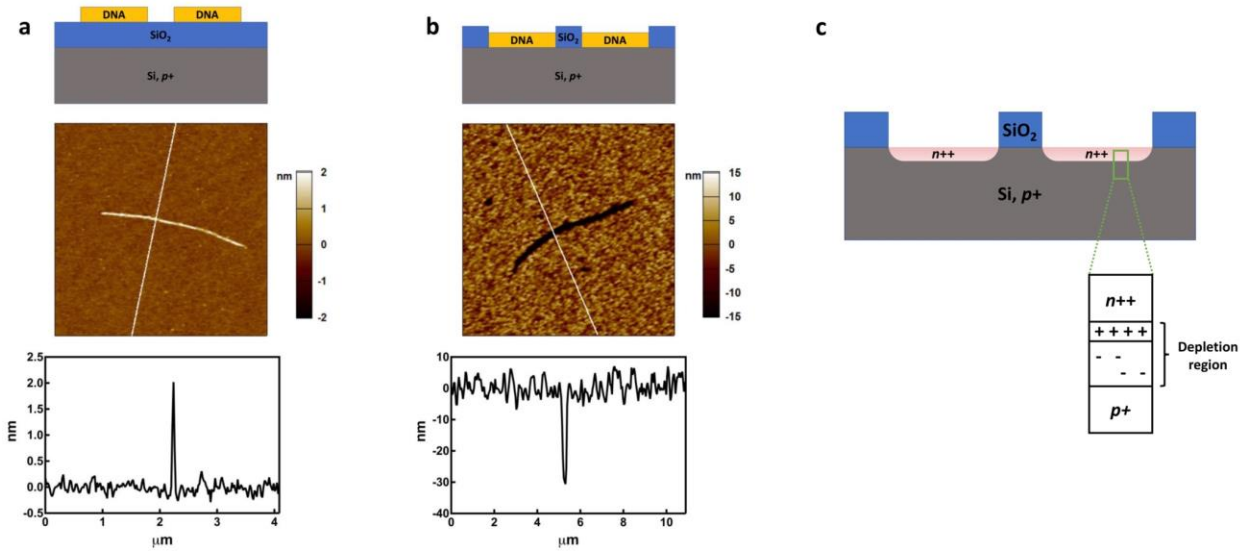

Figure 29. Schematic diagrams, AFM images and cross sections of the silicon wafer prepared from DNA nanotubes for PN diodes fabrication. a, Deposition of DNA nanotubes onto a Si/SiO_2 substrate. b, Selective removal of the SiO_2 underneath DNA template via DNA-enhanced etching of SiO_2. c, Schematic diagram of the sample after the DNA-based doping process.

4.4.2 Fabrication of electrodes to test PN diodes

We used EBL to pattern electrodes on a single nanowire-like doped region (Figure 30a, b) to test the performance of a single vertical PN diode. During the fabrication, we deposited a thin layer of HfO_2 (20 nm) to prevent the electrode from contacting the doped areas other than the single nanowire doped area. After depositing suitable electrodes, we used wire bonding to connect the electrodes to the external chip carrier to avoid damaging the HfO_2 layer, allowing better electrical measurements. Figure 30c is a photography of the device after wire bonding. A schematic diagram of the sample ready for testing is also shown in Figure 30d. It should be noted that the area doped with nanowires is embedded in the intrinsic Si wafer.

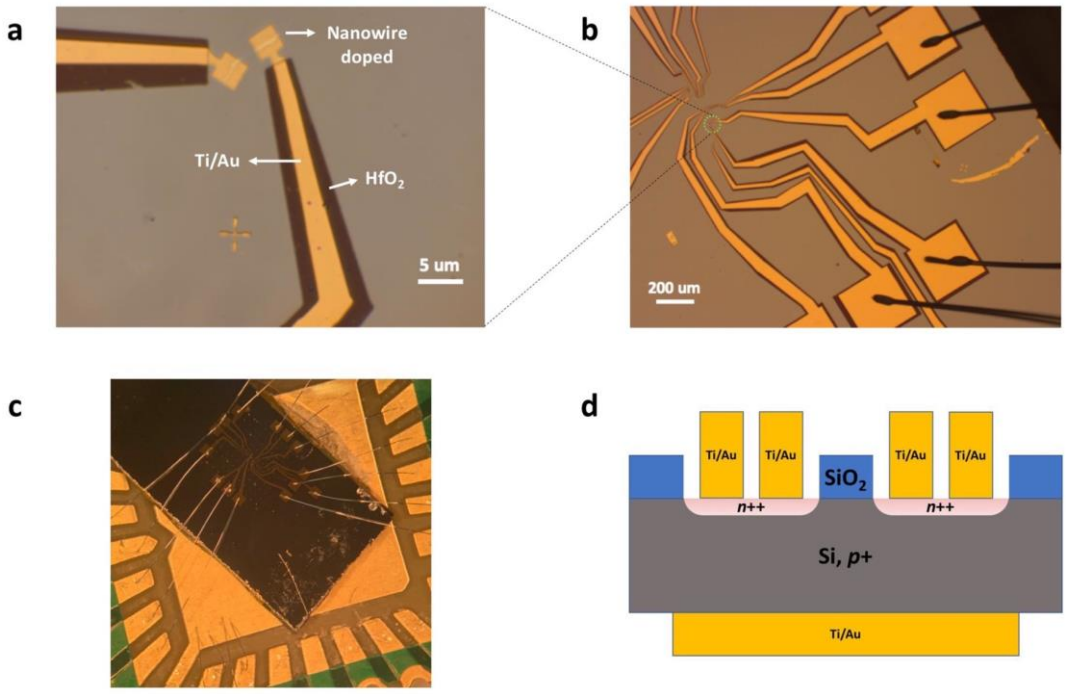

Figure 30. Fabrication of PN diodes from a single 'nanowire'-shaped doped region. a, b, Optical image of the patterned electrodes. c, Photograph of the device after wire bonding. d, Schematic diagram of the PN diode.

4.4.3 Characterization of the PN diode

To measure the PN diode, we connected the anode to the *p*-type wafer and the cathode to the electrode on the nanowire doped area (Figure 31a). The characterization result of the device performance is shown in Figure 31b. It can be seen from the results that the DNA nanowire doped region exhibits the unique current-voltage performance of the PN diode, while the non-doped region does not. By analyzing the I-V curve in the result, it can be known that the knee voltage of the PN diode is ≈0.7 V, which is consistent with the theoretical knee voltage of Si.[170-171] The different responses of the device to forward and reverse voltages confirm the successful fabrication of vertical PN diodes.

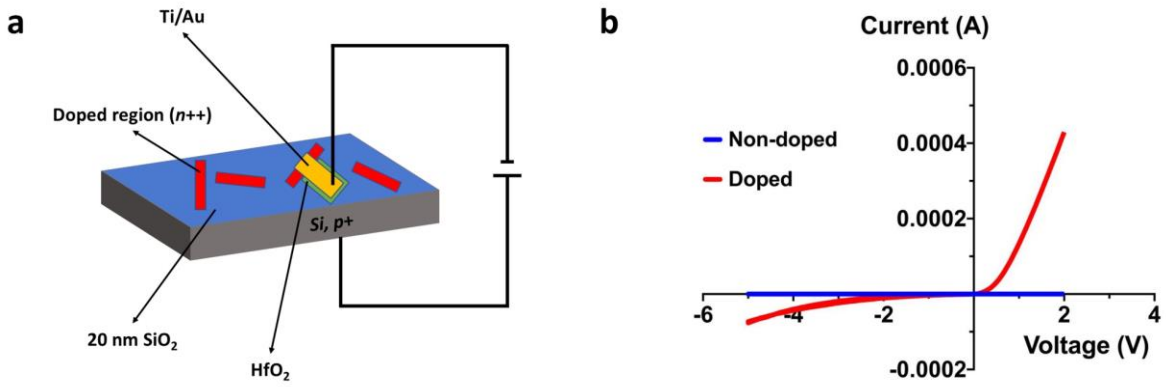

Figure 31. Characterization of the PN diode. a, Schematic diagram for the test of the device. b, I-V curves for the 'nanowire' doped region and non-doped region.

4.4.4 Fabrication of other devices using modified DNA

After getting the good performance of the first PN diode, we attempted to use modified

DNA to produce more complicated electronic devices. We proposed to use a DNA-Au-DNA structure to fabricate a three-terminal device. Our goal is to demonstrate the triplet function of the DNA nanostructure template: first, as a template to intergrade electrode; second, as an etching template; and third, as a doping source.

The steps are shown in Figure 32. We first deposited the synthesized DNA-Au-DNA on a *p*-type wafer with 40 nm SiO_2. Then, we exposed the sample to HF vapor to remove all SiO_2 under the DNA material, while leaving approximately 10 nm SiO_2 as a dielectric layer under the Au nanoparticles. After that, a DNA-based doping method similar to that used in the manufacture of PN diodes can be used to dope phosphorus atoms into the wafer to form an *n-p-n* junction. At the same time, the process will leave a dielectric layer (SiO_2) and the gold electrode in the middle, serving as the gate electrode. In addition, we intend to control the dopant concentration on both sides to achieve degenerative doping, which will create good electrical contact. By using this modified DNA to manufacture electronic devices, the complexity and cost of manufacturing transistors can be greatly reduced.

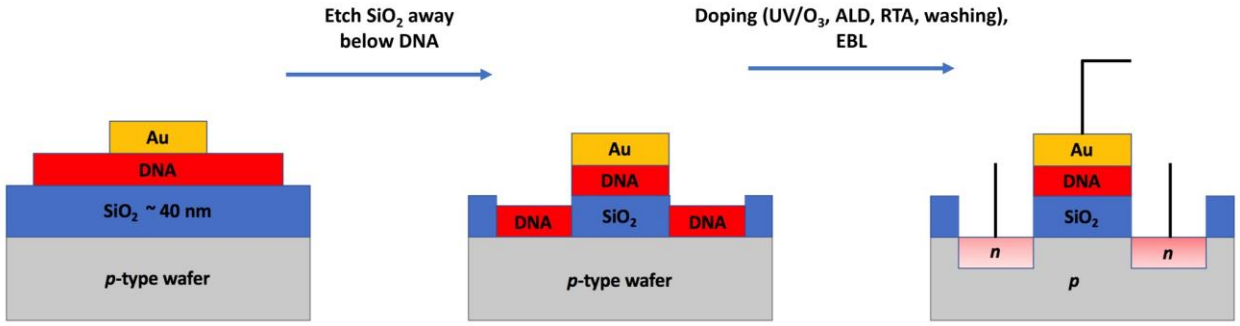

Figure 32. Shcematic diaggram the use of Au-modified DNA to simplify the fabrication of three-terminal devices.

For this work, we have synthesized the DNA-Au-DNA structures using the base pairing. We used AFM images to track and verify the formation of the designed structure (Figure 33a). The width of the DNA-Au-DNA structure is *ca.* 50 nm, the length is *ca.* 600 nm, and the height of the Au-DNA in the middle is *ca.* 8 nm. We found that not all structures are perfect DNA-Au-DNA structures. Many structures contain DNA-Au fragments, and the desired DNA-Au-DNA structure accounts for only 10% of all structures. To increase the yield, purification methods such as gel purification can be performed. However, given the proof-of-principle nature of the work, it is not critical to achieve high yield of the assembly. After etching, we used ellipsometry and AFM to check and verify that there is indeed an etching difference between DNA and Au modified DNA parts (Figure 33b). We found that the depth of the trench created by the DNA portion is about 17 nm, and the remaining SiO_2 under the Au-DNA is about 10 nm. It is difficult to identify the gold nanoparticles after etching from the AFM images due to the rough surface. To see the etching difference between DNA and Au-DNA parts, we used another etched sample for inspection. This time we removed all the material on the top surface by sonicating the sample in water for 2 days. Later in AFM images (Figure 33c), we found the trench depths of Au-DNA and DNA are different. Since the height of the Au-DNA material is about 8 nm, the trench depth under the Au-DNA is also about 8 nm, which indicates that it is difficult to see the Au-DNA part in the AFM without the sonication treatment. Without the sonication treatment, the height of the Au-DNA part close to the background height and the rough surface both increase the difficulty of seeing the Au-DNA part. However, the 35-nm depth of the trench under DNA is much larger than that under Au-DNA, which shows that the etching difference does exist. Although it is difficult to see the Au-DNA part, we still performed a DNA-based doping process because we already know that there is an etching difference.

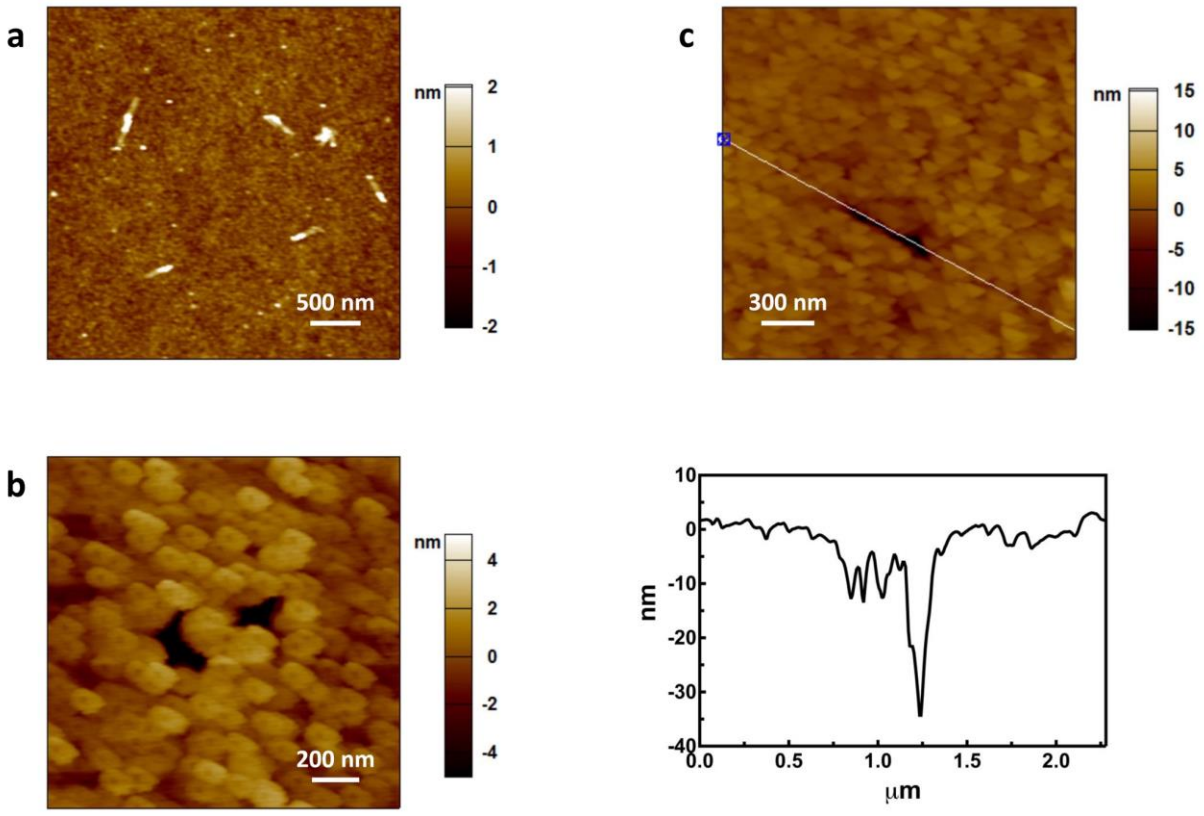

Figure 33. AFM images of the wafer prepared for the fabrication of a three-terminal device. a, Depostion of DNA-Au-DNA structures onto a Si/SiO_2 substrate. b, Selective removal of the SiO_2 underneath DNA template via DNA-enhanced etching of SiO_2. c, Removal of DNA-Au-DNA structures for another etched sample by the sonication in water for 2 days. White cross section indicates the location where the height values were measured.

A major challenge we faced here is to image the structure at high resolution and over larger area so that the EBL process can pattern testing electrodes on the two doped regions and the gold electrode in between. We had challenges using SEM to observe the gold nanoparticles, possibility due to the thin layer of SiO_2 underneath (Figure 34). Since it is necessary to use EBL to write at least three electrodes on the etched structure, the lack of high quality SEM image makes the EBL process extremely challenging. In addition, our existing EBL equipment also has limitations in

alignment, which further increases the difficulty of patterning the testing electrodes. These engineering issues needs to be addressed before this project can be taken to the next step.

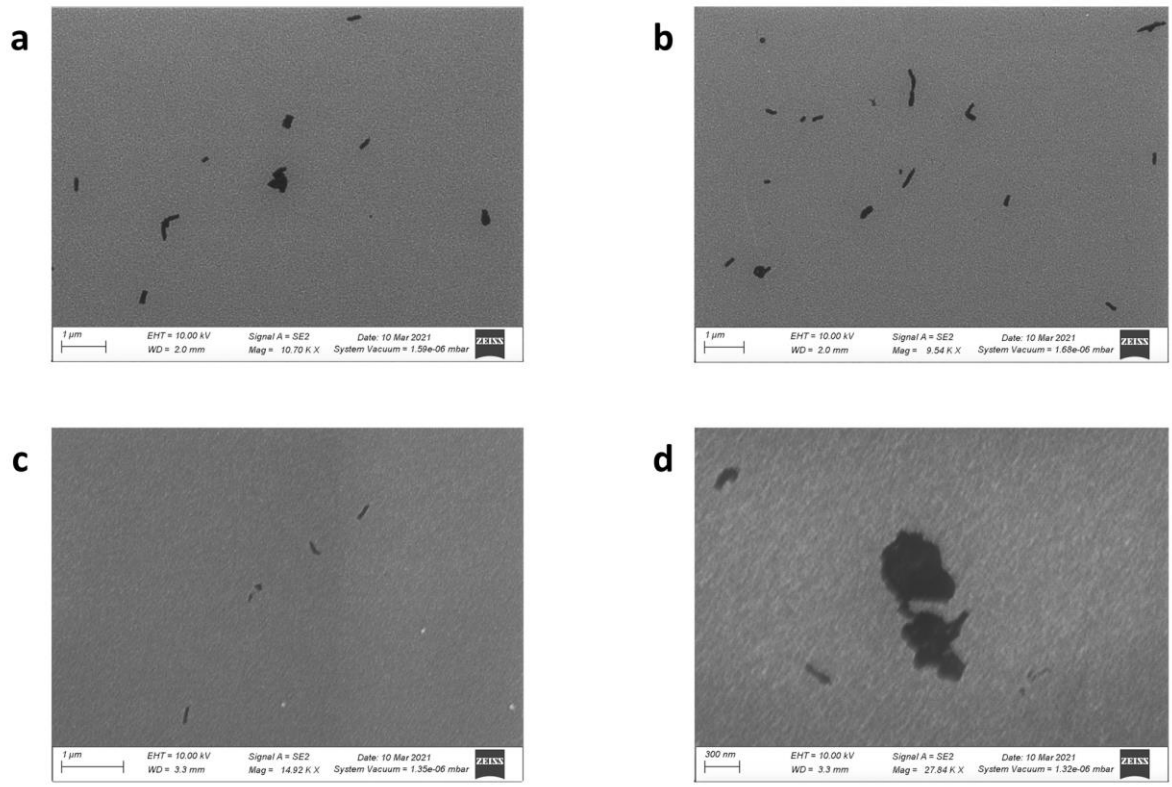

Figure 34. SEM images of wafers after the DNA-based doping processes. a, b, RTA process performed at 900 °C. c, d, RTA process performed at 1000 °C.

4.5 Conclusion

In summary, we have successfully fabricated PN diodes using DNA-based doping methods. The performance of the device under the forward and reverse voltages is consistent with

the traditional PN diode. The successful fabrication of PN diodes here further provides the application of DNA-based doping in device manufacturing. We have also proposed a method of using metal-modified DNA to simplify the manufacturing process of complex devices, although there are still some technical challenges. We hope that the device fabrication method here will help the future manufacturing of electronic devices based on DNA nanotechnology, so that electronic devices can be produced in a simple, low-cost, high-resolution and large-scale way.

5.0 Effect of Contaminations on the Surface Potential of Graphite

5.1 Chapter Preface

Materials contained in this chapter are in preparation for publication as a research article.

List of Authors: Ruobing Bai, Nathan L. Tolman and Haitao Liu

Author Contributions: R.B. and H.L. designed and directed the experiments. R.B. conducted the experiments. All authors discussed the results. R.B. and H.L. wrote the manuscript with input from all authors.

5.2 Introduction

Graphite has high heat resistance, high heat and electrical conductivity.[172-173] These properties make it suitable for applications in electrodes, batteries and electrical products.[174-176] Moreover, a single-layer graphite, or graphene, has also been widely researched for potential applications in sensors and electronic devices due to its unique electrical properties,[177-178] some examples of graphene-based devices include gas sensors, biosensors, electrochemical sensors, flexible light emitting diodes (LEDs), solar cells and field effect transistors (FETs).[179-184] Work function of graphitic material play an important role in many of these applications as it impacts interfacial charge doping and charge injection. Therefore, they will benefit from a detailed understanding of the work function of graphitic surface exposed to air.

Graphite basal plane is also considered a stable surface in air due to be absence of dangling bonds and surface reconstruction. For this reason, highly oriented pyrolytic graphite (HOPG) is extensively used as a standard to calibrate the work function of other materials.[185-187] The work function of graphene depends on the number of layers and was predicted to be between 4.46 eV and 4.64 eV.[185] However, the work function values of HOPG found in the literature are very different, even when measured under the same environmental conditions. The reported values range from less than 4.5 eV to as high as 5 eV.[188-192] Such a wide range of work function values may cause high uncertainty when calibrating the work function of other materials.[193] The different work function values on HOPG may be due to surface contamination.[194] Therefore, when using HOPG to calibrate the work function, the changes in the surface characteristics of the HOPG sample should be considered.

The surface properties of graphite itself have been explored through extensive theoretical and experimental studies.[195-197] However, a series of recent characterizations, such as atomic force microscopy (AFM), water contact angle, Fourier transform infrared (FTIR) and ellipsometry, have shown that the graphite surface after exfoliation will be contaminated by the surrounding air within a time frame ranging from minutes to days.[198-202] A recent ultra-violet photoelectron spectroscopy (UPS) experiment shows that after a freshly-exfoliated graphite surface was exposed to air for more than 1 day, there was still change in the composition of the surface contaminations.[203] These and other literatures also indicate that the contamination on the graphite surface may contain hydrocarbon compounds, metal atoms, oxygen and sulfur.[204-205] All of those findings suggest that the electrical properties of graphite may also be affected by contaminants in the air. Therefore, when studying the electrical properties of the graphite surface, the influence of unintentional airborne contaminations needs to carefully considered. In this regard, Martinez-Martin and

coworkers reported that the effect of adsorption of polycyclic aromatic hydrocarbons on the surface potential map of HOPG. Their experiment was conducted in a vacuum chamber that has residue hydrocarbon vapor from an unidentified.[206]

Here, we use Kelvin probe force microscopy (KPFM) to study the influence of ambient air contaminations on the surface potential of HOPG. We track the change of surface potential map on the same area of HOPG over several days and report both long- and short-term changes due to the unintentional contamination of HOPG surface by airborne hydrocarbons.

5.3 Experimental Section

5.3.1 Materials

HOPG (SPI-2, 10 × 10 × 2 mm in size) was purchased from SPI Supplies. Scotch brand tape (3M, Inc) was used to peel off the top layers of the basal plane of the HOPG. The calibration slide used for surface potential calibration was purchased from Motic Microscopes.

5.3.2 KPFM measurements

Throughout the study, surface morphologies and electrical curves of the samples were monitored on an Asylum MFP-3D Atomic Force Microscope by tapping and electrical mode in air with Budget Sensors Tap 190E-G tips (190 kHz, 48 N/m). Images were analyzed by Igor Software (Version 6.3.7.2) equipped with Asylum Research package. KPFM measurements were performed in an amplitude-modulated system by using a two-pass technique. The first pass was to determine

the topography of the surface and the second pass was to measure the contact potential difference of the sample surface. The applied tip voltage was 3 V. All images were flattened to center data and remove tilt. Due to the flattening, the center of the potential map is close to 0 V.

5.4 Experimental Section

5.4.1 Results

We created a clean HOPG surface by using tape to remove the top layers of HOPG and mounted the sample on the AFM instrument located in a shared facility instrument room. We used KFPM to characterize an HOPG surface at the same location after its cleavage and during its storage in ambient for up to 4 days. We observed a slow, but significant change of the surface potential of HOPG during this time period. The result is shown in Figure 35. The most important observation here is that while there is no obvious change in the amplitude images (Figure 35. a1-a5) collected on different days, the surface potential maps showed significant variations.

On the surface potential map of freshly-cleaved HOPG, we observed micrometer-sized domains, with both positive and negative potential contrast (Figure 35.b1). Notably, these domains are not linked to any features in the corresponding amplitude image although some do appear to be correlated with step edges. In the latter case, the domains are mostly showing a negative surface potential contrast. After 1 day of air exposure, the potential map becomes more heterogeneous (Figure 35. b2), with a large number of new domain structure appeared. This trend continued on the second day (Figure 35. b3) of air exposure, with a noticeable increase in the heterogeneity of the background. On the third day (Figure 35. b4) and especially the fourth day (Figure 35. b5) of

air exposure, the surface potential images continue to show significant change; however, the background becomes much more homogeneous. In particular, from day 3 to day 4, many domain features disappeared in the surface potential map. During this time period, the amplitude images are practically the same.

We also tracked the topography and surface potential images of another HOPG sample for up to 14 days (Figure 36). This sample showed a similar behavior during day 0 - 5 as we discussed above. After day 5, the surface potential map of the sample remained largely unchanged.

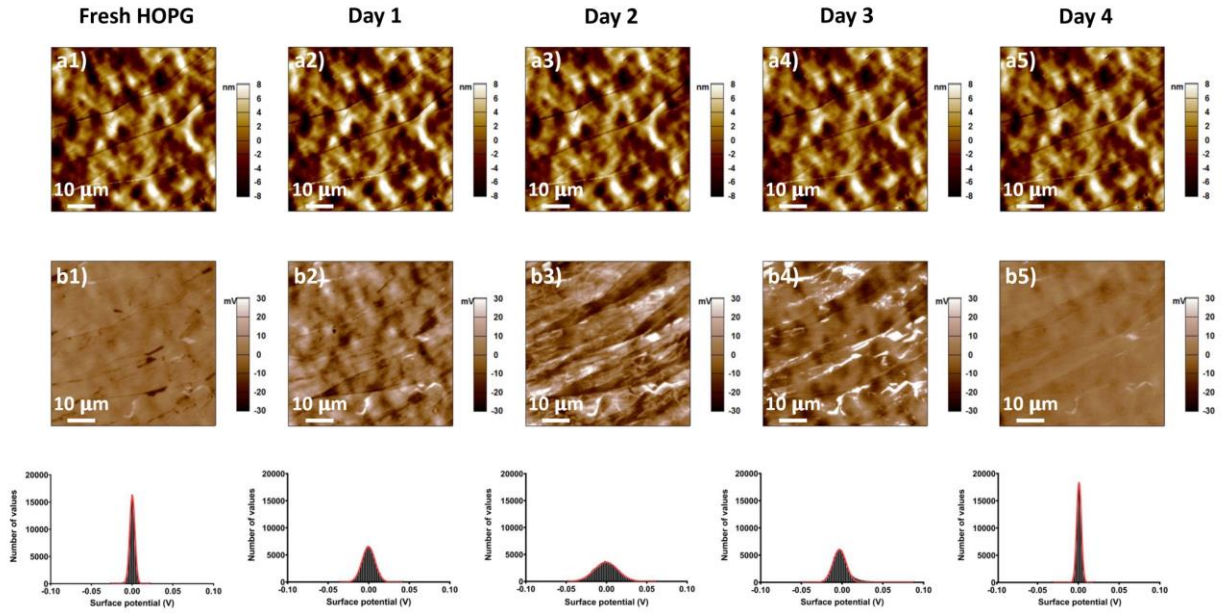

Figure 35. KPFM images of HOPG on different days at the same location. a1-a5, Amplitude images. b1-b5, Potential maps. Last row, Histogram of the potential map corresponding to different days.

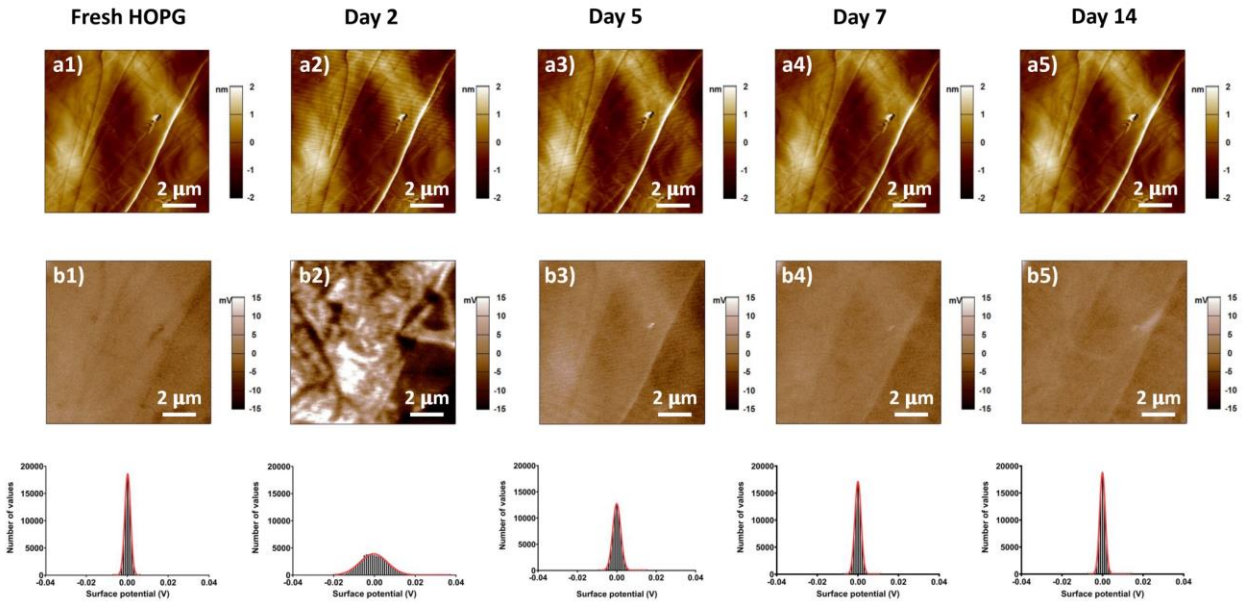

Figure 36. KPFM images of HOPG on different days at the same location (2 weeks study for another sample). a1-a5, Amplitude images. b1-b5, Potential maps. Last row, Histogram of the potential map corresponding to different days.

To quantify the change of the surface potential map, the histograms of the CPD extracted from the potential map are given in Figure 35 and Figure 36. We also plotted the half width at half maximum (HWHM) of the histogram peaks of the two samples (one sample for 4 days and the other sample for 14 days) as a function of air exposure time in Figure 37. For both samples, the HWHM value gradually increased in the first several days and then decreased over time.

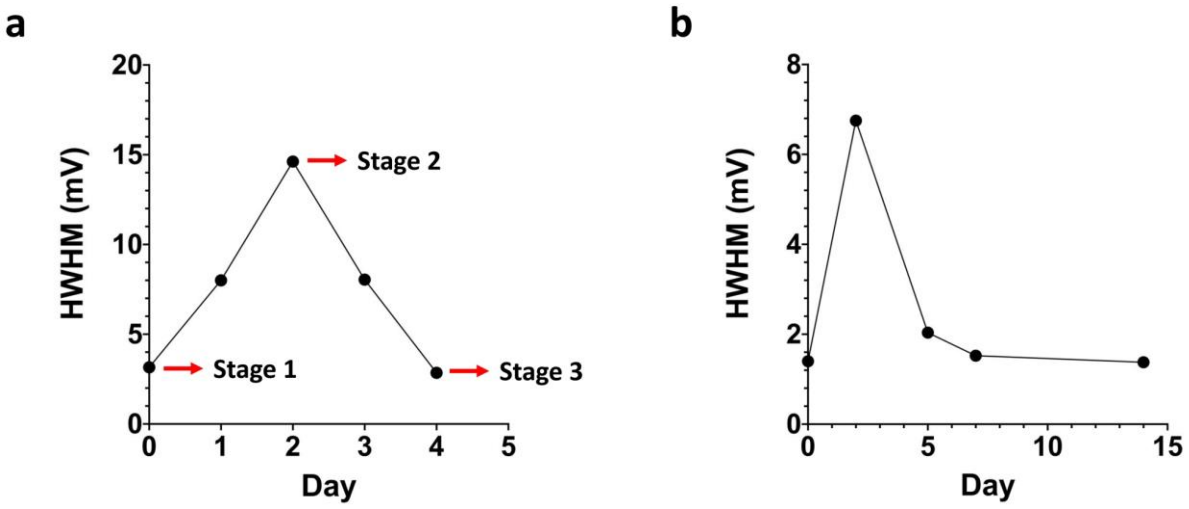

Figure 37. HWHM for the histogram of the potential map on different days. a, Four-day study of the sample in Figure 35. b, Fourteen-day study of the sample in Figure 36.

In addtition to time, the surface potential map of HOPG may be also sensitive to the history of AFM scan. For the sample shown in Figure 35, we have carried out contineous scans at the same location during each day. On the third day we found that the potential map showed a gradual change after multiple scans. Shown in Figure 38a, we show 12 KPFM images sequentially collected on this sample on day 3. Both the positive and negtive contrast regions reduced in area after repeated scanning. It can be seen that the potential map stabilized after the 10th scan. To highlight the change in the sample, we plot the cross sections of the potential maps at the same location for the first, sixth, and twelfth scans. Shown in Figure 38b, many peaks in the cross section completely disappeared after repeated AFM scans while one peak remained at the same intensity.

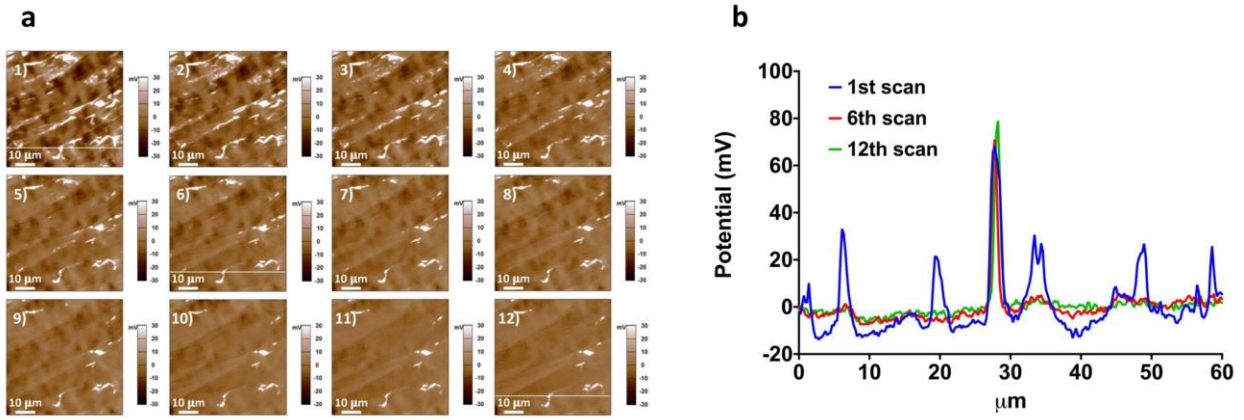

Figure 38. KPFM potential maps of HOPG scanning continuously at the same location on day 3. a, First to twelfth scan. White cross sections indicate locations where the potential values were measured. b, Potential values measured at locations where white lines indicate.

To verify whether the behavior shown in Figure 38 is caused by AFM laser or environmental humidity, we conducted experiments on the surfaces of other samples that had been contaminated for 3 days. We first collect multiple consecutive KPFM images at the same location on the three sample surfaces each time (each AFM scan takes 8.5 minutes). These first collected images showed slight differences, and the size of some positive CPD areas gradually decreased but did not completely disappear (similar to the observation in Figure 38). Then, we stopped the AFM scanning of these samples and turned off the AFM laser for one sample for two hours. For the other two samples, we kept the AFM laser turned on and reduced the humidity in the reaction chamber with nitrogen for one hour. After the corresponding processing time was over, we performed KPFM scanning on the same area of the three samples each time. For comparison, we plotted the HWHM of the histogram of each potential map in Figure 39. We can see that the HWHM of the three samples dropped sharply at the beginning and finally reached a stable level. The data here indicates that the cause for the change in the potential map during scans is time or

mechanical contact between the AFM tip and the sample, rather than laser illumination or environmental humidity.

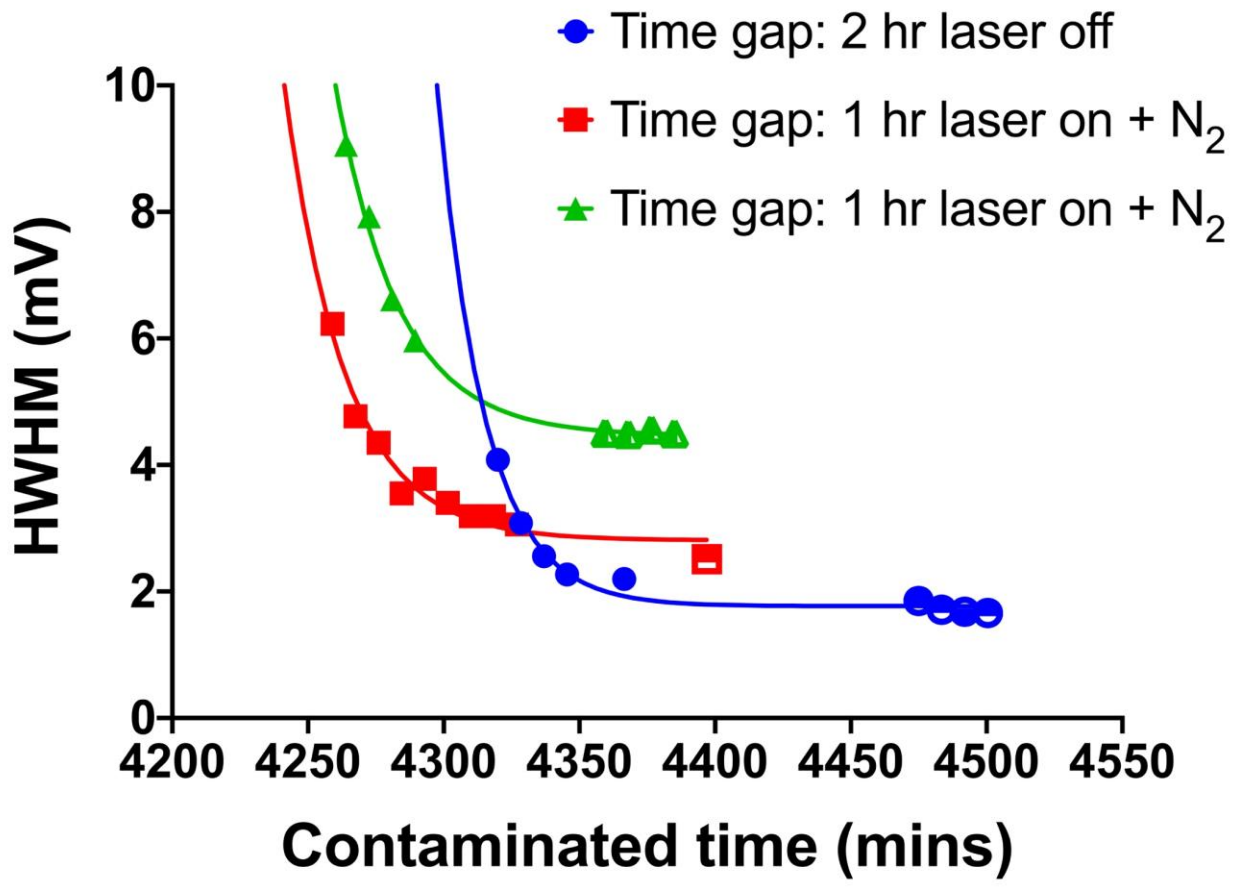

Figure 39. The HWHM of the histogram of the potential maps of the three samples on the 3rd day changes with time.

In addition, for some scans of a sample on day 2, we found that HWHM of the histogram of the potential maps can also gradually increase with the scan (Figure 40). Here, the change trend of HWHM over time is opposite to that on day 3. But this is reasonable, because day 2 is the process of introducing more contaminations. This result shows that the continuous scanning will not necessarily lead to a decrease in HWHM, because the time effect is involved.

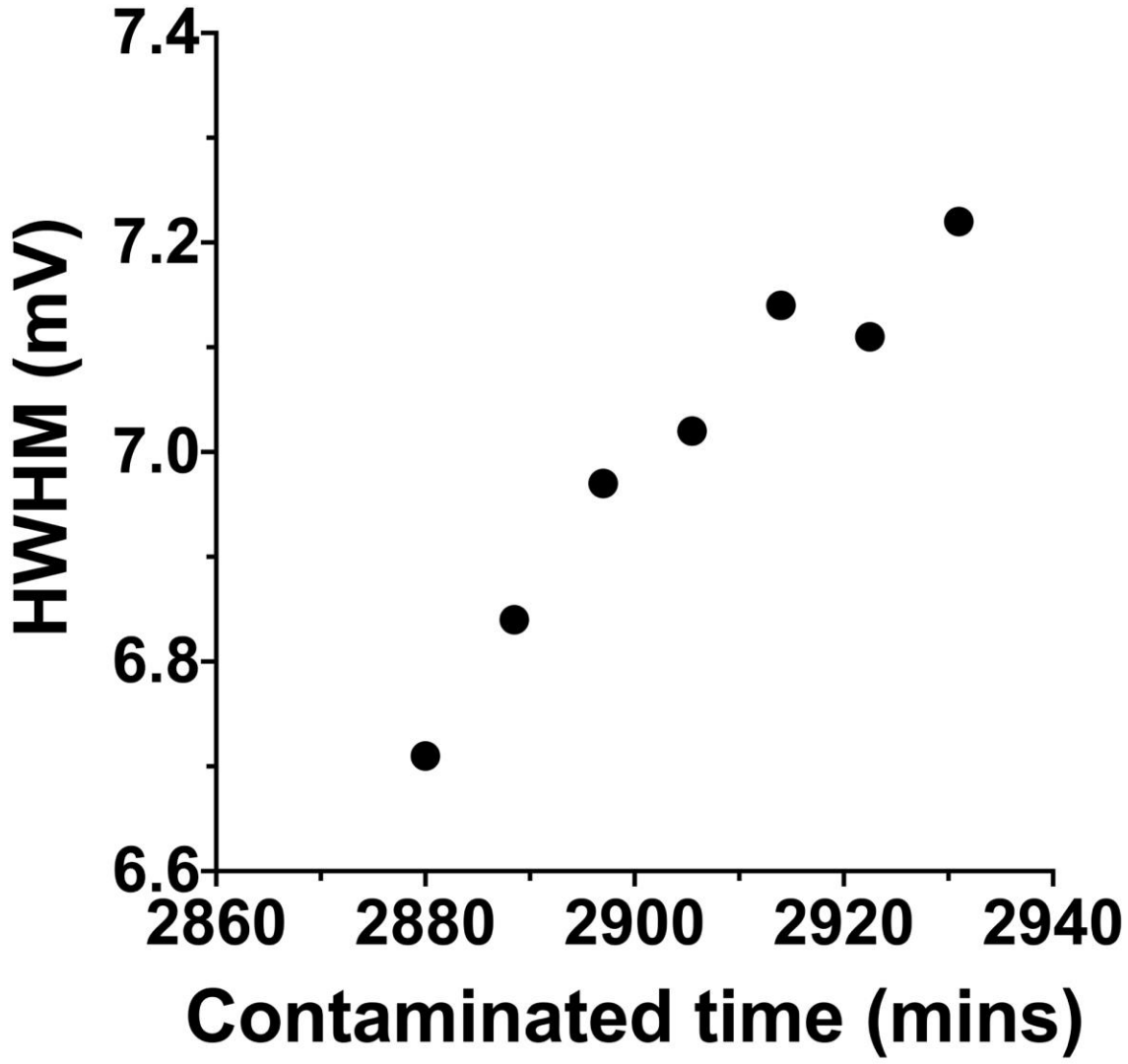

Figure 40. The HWHM of the histogram of the potential maps of one sample on the 2nd day changes with time.

To understand our data, it is important to know how the positive/negative CPD features in the potential map is translated to real surface potentials, *i.e.*, is positive CPD features due to a higher or lower surface potential. We used a glass calibration slide with chromium metal deposition for KPFM scanning. The work function of chromium metal is about 4.5 eV, and the work function of glass is about 4.7 eV.[207-208] From the potential map in Figure 41, we see that the

CPD of the chromium metal is larger than that of the background glass. This result indicates that the area with a larger work function will exhibit a lower CPD in our potential map. Based on the data analysis, we deduce that the work function of the lower CPD region in the HOPG potential map will be larger than that of graphite.

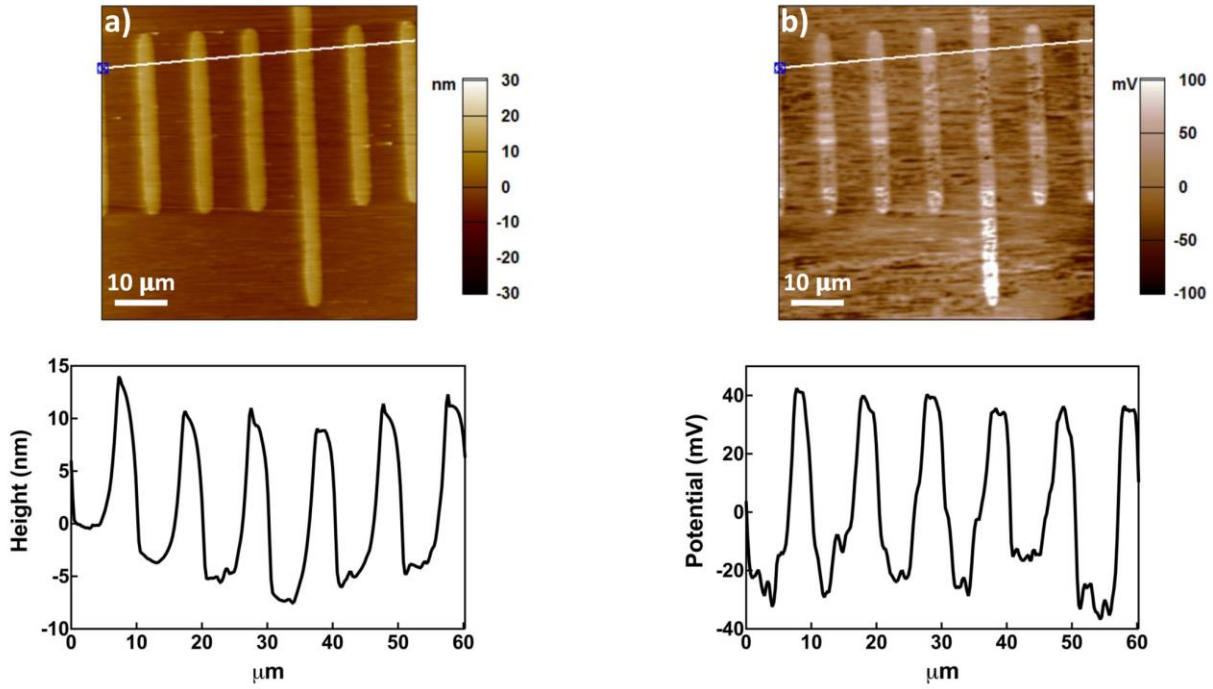

Figure 41. KPFM for a glass calibration slide with the deposition of chromium metal. a, Height image. b, Potential image. White cross sections indicate locations where values were measured.

5.4.2 Discussion

The data we presented above suggests a dynamic surface where the surface coverage, type and/or orientation of the airborne contaminants are changing constantly at the HOPG-air interface.

Time has the most significant impact on the coverage and type of the contaminant. We describe the influence of contaminants on the surface potential map of the sample in three stages (Figure 42): stage 1, when the HOPG surface was just exfoliated and the surface coverage of contaminants is low, the surface potential of the sample is mostly uniform as it reflects the nature of clean HOPG; stage 2, when more contaminants are absorbed, the surface potential is highly heterogeneous, due to the different type and/or orientation of the contaminants; stage 3, at even longer air exposure times, we observed a decrease in the HWHM of the distribution of surface potential. This data suggests that the composition and/or orientation of the contaminants on the sample surface becomes more uniform and results in a decrease in the heterogeneity of the surface potential. The potential map did not show significant change from day 5 to day 12, suggesting that equilibrium is achieved at day 5 of air exposure.

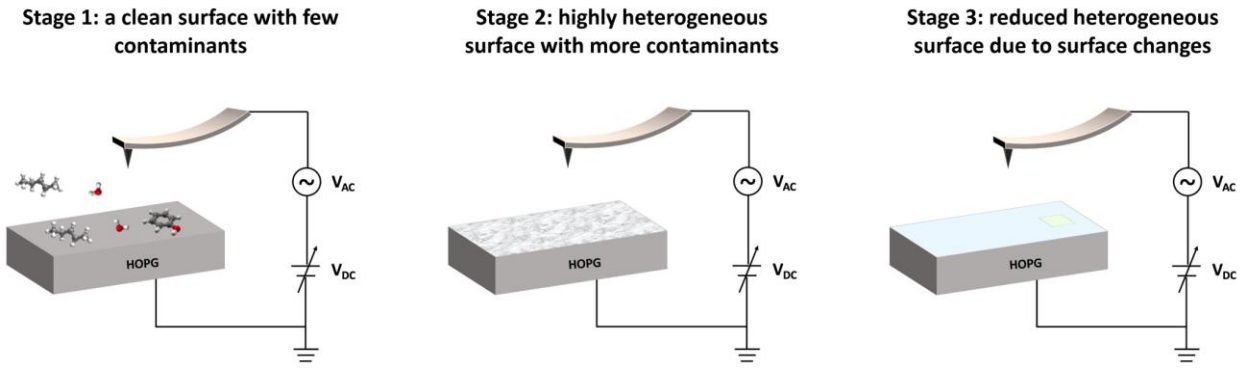

Figure 42. Schematic diagram of three stages for the influence of air contaminants adsorption on the surface potential map of HOPG.

From the calibration, we know that patches of bright spots (*i.e.*, areas of high CPD) are of lower work function compared to the background. We speculate that the change in the CPD features are related to a reorganization of the surface adsorbed dipole. Specifically, the larger work

function may be related to the specific dipole direction (outward from air to HOPG) of some contaminants in that region, because these contaminants will shift the vacuum energy level upwards, thereby increasing the working function of HOPG (Figure 43a).[209-210] Similarly, the higher CPD (lower work function) area in the HOPG potential map may be related to the presence of some contaminants with the opposite dipole direction (outward from HOPG to air) in that region (Figure 43b).[211] Over time, the orientation of the contaminant may change (Figure 43c). Another speculation for the disappearance of the surface potential in some areas of HOPG is the replacement of other contaminations. These new contaminants may be non-polar, or they may shield the potential on the sample surface.[161, 212-215]

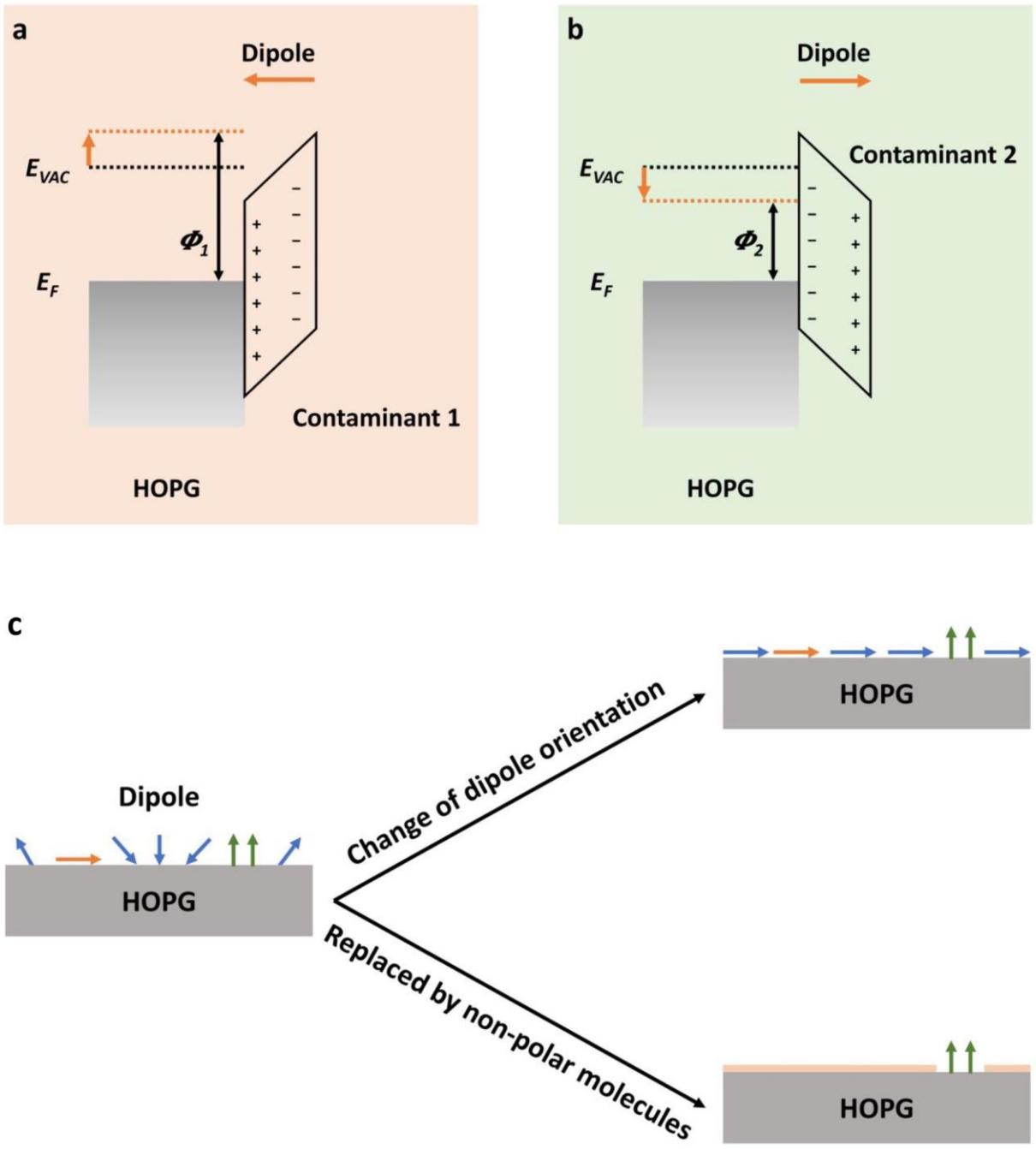

Figure 43. Schematic diagram of possible explanations for a, b, The influence of contaminants on the work function of the HOPG surface. c, The reducing heterogeneity on the potential diagram.

5.5 Conclusion

In summary, we used KPFM to study the potential map of the HOPG surface, and then found that air contaminant has a great influence on the potential map of the HOPG surface. The daily changes of the HOPG surface potential map are likely to be related to changes in the coverage, type and/or direction of contaminants on the surface over time. Our findings indicate that when experimenting with the work function of graphite in the air, we should consider the influence of molecular adsorption on its surface electrical properties at different stages. We hope that our findings will help to better understand the surface properties of HOPG, which may help develop technologies to prevent or utilize graphite contamination.

6.0 Summary and Prospective

6.1 Summary

In this dissertation, I demonstrated our efforts to combine DNA nanotechnology with electronic device production technology. We have developed a doping method based on DNA materials to produce electronic devices. By the way, I also studied the influence of contaminations on the surface potential of graphite.

In chapter 2, I reported a method of using DNA nanostructures as patterns and doping sources to achieve *n*-type site-specific doping of Si wafers. This method diffuses the phosphorus atoms naturally contained in DNA into Si at high temperatures, resulting in local *n*-type doping. A doping length of 30 nm is achieved for 10s of thermal treatment at 1000 °C. The characteristics of the prototype FET further fabricated using the DNA-based doping strategy confirmed that the doping is *n*-type. Compared with traditional doping strategies, this method is unique in that it has the potential to deliver different types and/or doses of dopants in one doping step. Such a strategy provides a new way to reduce the complexity and cost of semiconductor nonmanufacturing.

In Chapter 3, I used DNA nanostructures as templates to pattern mixed SAMs to achieve site-specific delivery of *n*-type and *p*-type dopants, and further help form both *n*-type and *p*-type doping. This work provides a way to combine DNA nanostructures with monolayer doping technology, which further expands the application of DNA nanotechnology in the field of doping, making it possible to achieve bottom-up doping of any shape.

In Chapter 4, I demonstrated the use of DNA-based doping methods to fabricate PN diodes. This method diffuses the phosphorus atoms naturally contained in DNA into the *p*-type Si through

high temperature, thereby generating multiple vertical PN diodes. The performance of the PN diode produced by the DNA-based doping method is consistent with the traditional PN diode. We also proposed a method of using metal-modified DNA to simplify the manufacturing process of complex devices. The use of DNA to fabricate devices here further provides practical applications of DNA-based doping in device fabrication, and provides the possibility for simple, low-cost, high-resolution and large-scale production of electronic devices.

In Chapter 5, we also used the key characterization technique KPFM to study the potential map of the HOPG surface, and found that air contaminants have a great influence on the potential map of the HOPG surface. The daily changes of the HOPG surface potential map may be related to the changes in the coverage, type and/or direction of the contaminants on the surface over time. We pointed out that when learning the work function of graphite in air, the influence of molecular adsorption on its surface electrical properties should be considered at different cases. Our work has a better understanding of the electrical properties of the graphite surface, which may help the future use of graphite in the manufacture of electronic devices.

6.2 Future Perspective

Overall, my work has provided new insights into the use of DNA nanomaterials in electronics manufacturing and provided new methods to reduce the complexity and cost of semiconductor nanofabrication. Although the realization of the application of DNA-based doping in mass production still requires more research, such as the effective generation of large-scale DNA templates, the precise and accurate deposition of metal electrodes, and the development of manufacturing processes compatible with semiconductor devices, we hope that our results can be

a stepping stone for the development of DNA nanotechnology in future electronic devices. I also hope that the results for the effect of contaminations on the surface potential of graphite can be helpful to the application of graphite in various fields.

Bibliography

1. Schubert, E. F., *Doping in III-V Semiconductors*. E. Fred Schubert: 2015.

2. Berger, L. I., *Semiconductor Materials*. CRC Press: 1996.

3. El, R., Doping: Connectivity of Semiconductors. Lumen: 2019.

4. Donev, J. Dopant. https://energyeducation.ca/encyclopedia/Dopant.

5. Deambi, S., *From sunlight to electricity: A practical handbook on solar photovoltaic applications*. The Energy and Resources Institute (TERI): 2015.

6. Quirk, M.; Serda, J., *Semiconductor manufacturing technology*. Prentice Hall Upper Saddle River, NJ: 2001; Vol. 1.

7. Xu, Y.; Schoonen, M. A., The absolute energy positions of conduction and valence bands of selected semiconducting minerals. *American Mineralogist* **2000,** *85* (3-4), 543-556.

8. Himpsel, F.; Hollinger, G.; Pollak, R., Determination of the Fermi-level pinning position at Si (111) surfaces. *Physical Review B* **1983,** *28* (12), 7014.

9. Williams, J., Ion implantation of semiconductors. *Materials Science and Engineering: A* **1998,** *253* (1-2), 8-15.

10. Stolk, P.; Gossmann, H.-J.; Eaglesham, D.; Jacobson, D.; Rafferty, C.; Gilmer, G.; Jaraiz, M.; Poate, J.; Luftman, H.; Haynes, T., Physical mechanisms of transient enhanced dopant diffusion in ion-implanted silicon. *Journal of Applied Physics* **1997,** *81* (9), 6031-6050.

11. Anders, A., *Handbook of plasma immersion ion implantation and deposition*. Wiley New York: 2000; Vol. 8.

12. Michel, T.; Le Perchec, J.; Lanterne, A.; Monna, R.; Torregrosa, F.; Roux, L.; Commandre, M., Phosphorus emitter engineering by plasma-immersion ion implantation for c-Si solar cells. *Solar Energy Materials and Solar Cells* **2015,** *133*, 194-200.

13. Ziegler, J., High energy ion implantation. *Nuclear Instruments and Methods in Physics Research Section B: Beam Interactions with Materials and Atoms* **1985,** *6* (1-2), 270-282.

14. Kim, Y.; Massoud, H. Z.; Fair, R. B., The effect of ion-implantation damage on dopant diffusion in silicon during shallow-junction formation. *Journal of Electronic Materials* **1989,** *18* (2), 143-150.

15. Rubin, L.; Poate, J., Ion implantation in silicon technology. *Industrial Physicist* **2003,** *9* (3), 12-15.

16. Fahey, P. M.; Griffin, P.; Plummer, J., Point defects and dopant diffusion in silicon. *Reviews of Modern Physics* **1989,** *61* (2), 289.

17. Jones, S. W., Diffusion in silicon. *IC Knowledge LLC* **2008**, 23-61.

18. Gebel, T.; Voelskow, M.; Skorupa, W.; Mannino, G.; Privitera, V.; Priolo, F.; Napolitani, E.; Carnera, A., Flash lamp annealing with millisecond pulses for ultra-shallow boron profiles in silicon. *Nuclear Instruments and Methods in Physics Research Section B: Beam Interactions with Materials and Atoms* **2002,** *186* (1-4), 287-291.

19. Fiory, A., Rapid thermal processing for silicon nanoelectronics applications. *JOM* **2005,** *57* (6), 21-26.

20. Ferry, D. K., *Semiconductors*. Macmillan New York: 1991.

21. Ho, J. C.; Yerushalmi, R.; Jacobson, Z. A.; Fan, Z.; Alley, R. L.; Javey, A., Controlled nanoscale doping of semiconductors via molecular monolayers. *Nature Materials* **2008,** *7* (1), 62-67.

22. Guan, B.; Siampour, H.; Fan, Z.; Wang, S.; Kong, X. Y.; Mesli, A.; Zhang, J.; Dan, Y., Nanoscale nitrogen doping in silicon by self-assembled monolayers. *Scientific Reports* **2015,** *5* (1), 1-9.

23. Elbersen, R.; Vijselaar, W.; Tiggelaar, R. M.; Gardeniers, H.; Huskens, J., Fabrication and doping methods for silicon nano‐and micropillar arrays for solar‐cell applications: a review. *Advanced Materials* **2015,** *27* (43), 6781-6796.

24. Ye, L.; Pujari, S. P.; Zuilhof, H.; Kudernac, T.; de Jong, M. P.; van der Wiel, W. G.; Huskens, J., Controlling the dopant dose in silicon by mixed-monolayer doping. *ACS Applied Materials & Interfaces* **2015,** *7* (5), 3231-3236.

25. McKibbin, S.; Polley, C.; Scappucci, G.; Keizer, J.; Simmons, M., Low resistivity, super-saturation phosphorus-in-silicon monolayer doping. *Applied Physics Letters* **2014,** *104* (12), 123502.

26. Ho, J. C.; Yerushalmi, R.; Smith, G.; Majhi, P.; Bennett, J.; Halim, J.; Faifer, V. N.; Javey, A., Wafer-scale, sub-5 nm junction formation by monolayer doping and conventional spike annealing. *Nano Letters* **2009,** *9* (2), 725-730.

27. Ang, K.-W.; Barnett, J.; Loh, W.-Y.; Huang, J.; Min, B.-G.; Hung, P.; Ok, I.; Yum, J.; Bersuker, G.; Rodgers, M. In *300mm FinFET results utilizing conformal, damage free, ultra shallow junctions (X j ~ 5nm) formed with molecular monolayer doping technique*, 2011 International Electron Devices Meeting, IEEE: 2011; pp 35.5. 1-35.5. 4.

28. Longo, R. C.; Cho, K.; Schmidt, W. G.; Chabal, Y. J.; Thissen, P., Monolayer doping via phosphonic acid grafting on silicon: microscopic insight from infrared spectroscopy and density functional theory calculations. *Advanced Functional Materials* **2013,** *23* (27), 3471-3477.

29. Voorthuijzen, W. P.; Yilmaz, M. D.; Naber, W. J.; Huskens, J.; van der Wiel, W. G., Local doping of silicon using nanoimprint lithography and molecular monolayers. *Advanced Materials* **2011,** *23* (11), 1346-1350.

30. Martinez, V. M.; Edgar, T. F., Control of lithography in semiconductor manufacturing. *IEEE Control Systems Magazine* **2006,** *26* (6), 46-55.

31. Biswas, A.; Bayer, I. S.; Biris, A. S.; Wang, T.; Dervishi, E.; Faupel, F., Advances in top–down and bottom–up surface nanofabrication: Techniques, applications & future prospects. *Advances in Colloid and Interface Science* **2012,** *170* (1-2), 2-27.

32. Dill, F. H., Optical lithography. *IEEE Transactions on Electron Devices* **1975,** *22* (7), 440-444.

33. Li, C.; Wang, G., MEMS manufacturing techniques for tissue scaffolding devices. In *MEMS for Biomedical Applications*, Elsevier: 2012; pp 192-217.

34. Ito, T.; Okazaki, S., Pushing the limits of lithography. *Nature* **2000,** *406* (6799), 1027-1031.

35. Voelkel, R.; Vogler, U.; Bich, A.; Pernet, P.; Weible, K. J.; Hornung, M.; Zoberbier, R.; Cullmann, E.; Stuerzebecher, L.; Harzendorf, T., Advanced mask aligner lithography: new illumination system. *Optics Express* **2010,** *18* (20), 20968-20978.

36. Guckel, H., High-aspect-ratio micromachining via deep X-ray lithography. *Proceedings of the IEEE* **1998,** *86* (8), 1586-1593.

37. Altissimo, M., E-beam lithography for micro-/nanofabrication. *Biomicrofluidics* **2010,** *4* (2), 026503.

38. Tseng, A. A.; Chen, K.; Chen, C. D.; Ma, K. J., Electron beam lithography in nanoscale fabrication: recent development. *IEEE Transactions on Electronics Packaging Manufacturing* **2003,** *26* (2), 141-149.

39. Watt, F.; Bettiol, A.; Van Kan, J.; Teo, E.; Breese, M., Ion beam lithography and nanofabrication: a review. *International Journal of Nanoscience* **2005,** *4* (03), 269-286.

40. Acikgoz, C.; Hempenius, M. A.; Huskens, J.; Vancso, G. J., Polymers in conventional and alternative lithography for the fabrication of nanostructures. *European Polymer Journal* **2011,** *47* (11), 2033-2052.

41. Guo, L. J., Nanoimprint lithography: methods and material requirements. *Advanced Materials* **2007,** *19* (4), 495-513.

42. Chou, S. Y.; Krauss, P. R.; Renstrom, P. J., Nanoimprint lithography. *Journal of Vacuum Science & Technology B: Microelectronics and Nanometer Structures Processing, Measurement, and Phenomena* **1996,** *14* (6), 4129-4133.

43. Torres, C. S.; Zankovych, S.; Seekamp, J.; Kam, A.; Cedeno, C. C.; Hoffmann, T.; Ahopelto, J.; Reuther, F.; Pfeiffer, K.; Bleidiessel, G., Nanoimprint lithography: an alternative nanofabrication approach. *Materials Science and Engineering: C* **2003,** *23* (1-2), 23-31.

44. Schift, H., Nanoimprint lithography: An old story in modern times? A review. *Journal of Vacuum Science & Technology B: Microelectronics and Nanometer Structures Processing, Measurement, and Phenomena* **2008,** *26* (2), 458-480.

45. Zankovych, S.; Hoffmann, T.; Seekamp, J.; Bruch, J.; Torres, C. S., Nanoimprint lithography: challenges and prospects. *Nanotechnology* **2001,** *12* (2), 91.

46. Hawker, C. J.; Russell, T. P., Block copolymer lithography: Merging "bottom-up" with "top-down" processes. *MRS Bulletin* **2005,** *30* (12), 952-966.

47. Bates, C. M.; Maher, M. J.; Janes, D. W.; Ellison, C. J.; Willson, C. G., Block copolymer lithography. *Macromolecules* **2014,** *47* (1), 2-12.

48. Nunns, A.; Gwyther, J.; Manners, I., Inorganic block copolymer lithography. *Polymer* **2013,** *54* (4), 1269-1284.

49. Kim, H.-C.; Park, S.-M.; Hinsberg, W. D., Block copolymer based nanostructures: materials, processes, and applications to electronics. *Chemical Reviews* **2010,** *110* (1), 146-177.

50. Krishnamoorthy, S.; Hinderling, C.; Heinzelmann, H., Nanoscale patterning with block copolymers. *Materials Today* **2006,** *9* (9), 40-47.

51. Peters, R. D.; Yang, X. M.; Wang, Q.; de Pablo, J. J.; Nealey, P. F., Combining advanced lithographic techniques and self-assembly of thin films of diblock copolymers to produce templates for nanofabrication. *Journal of Vacuum Science & Technology B: Microelectronics and Nanometer Structures Processing, Measurement, and Phenomena* **2000,** *18* (6), 3530-3534.

52. Atabaki, A. H.; Moazeni, S.; Pavanello, F.; Gevorgyan, H.; Notaros, J.; Alloatti, L.; Wade, M. T.; Sun, C.; Kruger, S. A.; Meng, H., Integrating photonics with silicon nanoelectronics for the next generation of systems on a chip. *Nature* **2018,** *556* (7701), 349-354.

53. Atabaki, A. H.; Meng, H.; Alloatti, L.; Mehta, K. K.; Ram, R. J., High-speed polysilicon CMOS photodetector for telecom and datacom. *Applied Physics Letters* **2016,** *109* (11), 111106.

54. Peercy, P. S., The drive to miniaturization. *Nature* **2000,** *406* (6799), 1023.

55. Allan, A.; Edenfeld, D.; Joyner, W. H.; Kahng, A. B.; Rodgers, M.; Zorian, Y., 2001 technology roadmap for semiconductors. *Computer* **2002,** *35* (1), 42-53.

56. Kuo, Y., Thin film transistor technology—Past, present, and future. *Electrochemical Society Interface* **2013,** *22* (1), 55.

57. Zhang, G.; Surwade, S. P.; Zhou, F.; Liu, H., DNA nanostructure meets nanofabrication. *Chemical Society Reviews* **2013,** *42* (7), 2488-2496.

58. Surwade, S. P.; Zhao, S.; Liu, H., Molecular lithography through DNA-mediated etching and masking of SiO2. *Journal of the American Chemical Society* **2011,** *133* (31), 11868-11871.

59. Surwade, S. P.; Zhou, F.; Wei, B.; Sun, W.; Powell, A.; O'Donnell, C.; Yin, P.; Liu, H., Nanoscale growth and patterning of inorganic oxides using DNA nanostructure templates. *Journal of the American Chemical Society* **2013,** *135* (18), 6778-6781.

60. Surwade, S.; Zhou, F.; Li, Z.; Powell, A.; O'Donnell, C.; Liu, H., Nanoscale patterning of self-assembled monolayers using DNA nanostructure templates. *Chemical Communications* **2016,** *52* (8), 1677-1680.

61. Tian, C.; Kim, H.; Sun, W.; Kim, Y.; Yin, P.; Liu, H., DNA nanostructures-mediated molecular imprinting lithography. *ACS Nano* **2017,** *11* (1), 227-238.

62. Ricardo, K. B.; Xu, A.; Salim, M.; Zhou, F.; Liu, H., Deposition of DNA Nanostructures on Highly Oriented Pyrolytic Graphite. *Langmuir* **2017,** *33* (16), 3991-3997.

63. Zhou, F.; Michael, B.; Surwade, S. P.; Ricardo, K. B.; Zhao, S.; Liu, H., Mechanistic study of the nanoscale negative-tone pattern transfer from DNA nanostructures to SiO2. *Chemistry of Materials* **2015,** *27* (5), 1692-1698.

64. Becerril, H. A.; Woolley, A. T., DNA shadow nanolithography. *Small* **2007,** *3* (9), 1534-1538.

65. Li, H.; Carter, J. D.; LaBean, T. H., Nanofabrication by DNA self-assembly. *Materials Today* **2009,** *12* (5), 24-32.

66. Seeman, N. C., Nucleic acid junctions and lattices. *Journal of Theoretical Biology* **1982,** *99* (2), 237-247.

67. Seeman, N. C.; Lukeman, P. S., Nucleic acid nanostructures: bottom-up control of geometry on the nanoscale. *Reports on Progress in Physics* **2004,** *68* (1), 237.

68. Petrillo, M. L.; Newton, C. J.; Cunningham, R. P.; Ma, R. I.; Kallenbach, N. R.; Seeman, N. C., The ligation and flexibility of four‐arm DNA junctions. *Biopolymers: Original Research on Biomolecules* **1988,** *27* (9), 1337-1352.

69. Rothemund, P. W., Folding DNA to create nanoscale shapes and patterns. *Nature* **2006,** *440* (7082), 297.

70. Ke, Y.; Ong, L. L.; Sun, W.; Song, J.; Dong, M.; Shih, W. M.; Yin, P., DNA brick crystals with prescribed depths. *Nature Chemistry* **2014,** *6* (11), 994-1002.

71. Wei, B.; Dai, M.; Yin, P., Complex shapes self-assembled from single-stranded DNA tiles. *Nature* **2012,** *485* (7400), 623-626.

72. Ke, Y.; Ong, L. L.; Shih, W. M.; Yin, P., Three-dimensional structures self-assembled from DNA bricks. *Science* **2012,** *338* (6111), 1177-1183.

73. Mathieu, F.; Liao, S.; Kopatsch, J.; Wang, T.; Mao, C.; Seeman, N. C., Six-helix bundles designed from DNA. *Nano Letters* **2005,** *5* (4), 661-665.

74. Rothemund, P. W.; Ekani-Nkodo, A.; Papadakis, N.; Kumar, A.; Fygenson, D. K.; Winfree, E., Design and characterization of programmable DNA nanotubes. *Journal of the American Chemical Society* **2004,** *126* (50), 16344-16352.

75. Jungmann, R.; Scheible, M.; Kuzyk, A.; Pardatscher, G.; Castro, C. E.; Simmel, F. C., DNA origami-based nanoribbons: assembly, length distribution, and twist. *Nanotechnology* **2011,** *22* (27), 275301.

76. Yan, H.; Park, S. H.; Finkelstein, G.; Reif, J. H.; LaBean, T. H., DNA-templated self-assembly of protein arrays and highly conductive nanowires. *Science* **2003,** *301* (5641), 1882-1884.

77. He, Y.; Chen, Y.; Liu, H.; Ribbe, A. E.; Mao, C., Self-assembly of hexagonal DNA two-dimensional (2D) arrays. *Journal of the American Chemical Society* **2005,** *127* (35), 12202-12203.

78. Chen, J.; Seeman, N. C., Synthesis from DNA of a molecule with the connectivity of a cube. *Nature* **1991,** *350* (6319), 631-633.

79. He, Y.; Ye, T.; Su, M.; Zhang, C.; Ribbe, A. E.; Jiang, W.; Mao, C., Hierarchical self-assembly of DNA into symmetric supramolecular polyhedra. *Nature* **2008,** *452* (7184), 198-201.

80. Shih, W. M.; Quispe, J. D.; Joyce, G. F., A 1.7-kilobase single-stranded DNA that folds into a nanoscale octahedron. *Nature* **2004,** *427* (6975), 618-621.

81. Wang, P.; Meyer, T. A.; Pan, V.; Dutta, P. K.; Ke, Y., The beauty and utility of DNA origami. *Chem* **2017,** *2* (3), 359-382.

82. Hu, Q.; Li, H.; Wang, L.; Gu, H.; Fan, C., DNA nanotechnology-enabled drug delivery systems. *Chemical Reviews* **2018,** *119* (10), 6459-6506.

83. Pinheiro, A. V.; Han, D.; Shih, W. M.; Yan, H., Challenges and opportunities for structural DNA nanotechnology. *Nature Nanotechnology* **2011,** *6* (12), 763.

84. Liu, N.; Liedl, T., DNA-assembled advanced plasmonic architectures. *Chemical Reviews* **2018,** *118* (6), 3032-3053.

85. Peng, Z.; Liu, H., Bottom-up Nanofabrication Using DNA Nanostructures. *Chemistry of Materials* **2016,** *28* (4), 1012-1021.

86. Taniguchi, M.; Kawai, T., DNA electronics. *Physica E: Low-dimensional Systems and Nanostructures* **2006,** *33* (1), 1-12.

87. Kershner, R. J.; Bozano, L. D.; Micheel, C. M.; Hung, A. M.; Fornof, A. R.; Cha, J. N.; Rettner, C. T.; Bersani, M.; Frommer, J.; Rothemund, P. W., Placement and orientation of individual DNA shapes on lithographically patterned surfaces. *Nature Nanotechnology* **2009,** *4* (9), 557-561.

88. Gopinath, A.; Miyazono, E.; Faraon, A.; Rothemund, P. W., Engineering and mapping nanocavity emission via precision placement of DNA origami. *Nature* **2016,** *535* (7612), 401-405.

89. Wang, R.; Zhang, G.; Liu, H., DNA-templated nanofabrication. *Current Opinion in Colloid & Interface Science* **2018,** *38*, 88-99.

90. Hong, F.; Zhang, F.; Liu, Y.; Yan, H., DNA origami: scaffolds for creating higher order structures. *Chemical Reviews* **2017,** *117* (20), 12584-12640.

91. Zhang, H.; Chao, J.; Pan, D.; Liu, H.; Huang, Q.; Fan, C., Folding super-sized DNA origami with scaffold strands from long-range PCR. *Chemical Communications* **2012,** *48* (51), 6405-6407.

92. Schmidt, T. L.; Beliveau, B. J.; Uca, Y. O.; Theilmann, M.; Da Cruz, F.; Wu, C.-T.; Shih, W. M., Scalable amplification of strand subsets from chip-synthesized oligonucleotide libraries. *Nature Communications* **2015,** *6* (1), 1-7.

93. Ducani, C.; Kaul, C.; Moche, M.; Shih, W. M.; Högberg, B., Enzymatic production of'monoclonal stoichiometric'single-stranded DNA oligonucleotides. *Nature Methods* **2013,** *10* (7), 647.

94. Marchi, A. N.; Saaem, I.; Vogen, B. N.; Brown, S.; LaBean, T. H., Toward larger DNA origami. *Nano Letters* **2014,** *14* (10), 5740-5747.

95. Aghebat Rafat, A.; Pirzer, T.; Scheible, M. B.; Kostina, A.; Simmel, F. C., Surface‐Assisted Large‐Scale Ordering of DNA Origami Tiles. *Angewandte Chemie International Edition* **2014,** *53* (29), 7665-7668.

96. Woo, S.; Rothemund, P. W., Self-assembly of two-dimensional DNA origami lattices using cation-controlled surface diffusion. *Nature Communications* **2014,** *5* (1), 1-11.

97. Liu, W.; Zhong, H.; Wang, R.; Seeman, N. C., Crystalline two‐dimensional DNA‐origami arrays. *Angewandte Chemie International Edition* **2011,** *50* (1), 264-267.

98. Gerling, T.; Wagenbauer, K. F.; Neuner, A. M.; Dietz, H., Dynamic DNA devices and assemblies formed by shape-complementary, non–base pairing 3D components. *Science* **2015,** *347* (6229), 1446-1452.

99. Woo, S.; Rothemund, P. W., Programmable molecular recognition based on the geometry of DNA nanostructures. *Nature Chemistry* **2011,** *3* (8), 620.

100. Tikhomirov, G.; Petersen, P.; Qian, L., Programmable disorder in random DNA tilings. *Nature Nanotechnology* **2017,** *12* (3), 251.

101. Seeman, N. C., DNA components for molecular architecture. *Accounts of Chemical Research* **1997,** *30* (9), 357-363.

102. Lin, C.; Rinker, S.; Wang, X.; Liu, Y.; Seeman, N. C.; Yan, H., In vivo cloning of artificial DNA nanostructures. *Proceedings of the National Academy of Sciences* **2008,** *105* (46), 17626-17631.

103. Kick, B.; Praetorius, F.; Dietz, H.; Weuster-Botz, D., Efficient production of single-stranded phage DNA as scaffolds for DNA origami. *Nano Letters* **2015,** *15* (7), 4672-4676.

104. Praetorius, F.; Kick, B.; Behler, K. L.; Honemann, M. N.; Weuster-Botz, D.; Dietz, H., Biotechnological mass production of DNA origami. *Nature* **2017,** *552* (7683), 84-87.

105. Niekamp, S.; Blumer, K.; Nafisi, P. M.; Tsui, K.; Garbutt, J.; Douglas, S. M., Folding complex DNA nanostructures from limited sets of reusable sequences. *Nucleic Acids Research* **2016,** *44* (11), e102-e102.

106. Tian, C.; Zhang, C.; Li, X.; Hao, C.; Ye, S.; Mao, C., Approaching the limit: can one DNA strand assemble into defined nanostructures? *Langmuir* **2014,** *30* (20), 5859-5862.

107. Han, D.; Qi, X.; Myhrvold, C.; Wang, B.; Dai, M.; Jiang, S.; Bates, M.; Liu, Y.; An, B.; Zhang, F., Single-stranded DNA and RNA origami. *Science* **2017,** *358* (6369).

108. Li, N.; Shang, Y.; Han, Z.; Wang, T.; Wang, Z.-G.; Ding, B., Fabrication of metal nanostructures on DNA templates. *ACS Applied Materials & Interfaces* **2018,** *11* (15), 13835-13852.

109. Braun, E.; Eichen, Y.; Sivan, U.; Ben-Yoseph, G., DNA-templated assembly and electrode attachment of a conducting silver wire. *Nature* **1998,** *391* (6669), 775-778.

110. Zinchenko, A. A.; Yoshikawa, K.; Baigl, D., DNA‐templated silver nanorings. *Advanced Materials* **2005,** *17* (23), 2820-2823.

111. Nguyen, K.; Monteverde, M.; Filoramo, A.; Goux‐Capes, L.; Lyonnais, S.; Jegou, P.; Viel, P.; Goffman, M.; Bourgoin, J. P., Synthesis of thin and highly conductive DNA‐based palladium nanowires. *Advanced Materials* **2008,** *20* (6), 1099-1104.

112. Richter, J.; Mertig, M.; Pompe, W.; Mönch, I.; Schackert, H. K., Construction of highly conductive nanowires on a DNA template. *Applied Physics Letters* **2001,** *78* (4), 536-538.

113. Geng, Y.; Pearson, A. C.; Gates, E. P.; Uprety, B.; Davis, R. C.; Harb, J. N.; Woolley, A. T., Electrically conductive gold-and copper-metallized DNA origami nanostructures. *Langmuir* **2013,** *29* (10), 3482-3490.

114. Schreiber, R.; Kempter, S.; Holler, S.; Schüller, V.; Schiffels, D.; Simmel, S. S.; Nickels, P. C.; Liedl, T., DNA origami‐templated growth of arbitrarily shaped metal nanoparticles. *Small* **2011,** *7* (13), 1795-1799.

115. Sun, W.; Boulais, E.; Hakobyan, Y.; Wang, W. L.; Guan, A.; Bathe, M.; Yin, P., Casting inorganic structures with DNA molds. *Science* **2014,** *346* (6210).

116. Jin, Z.; Sun, W.; Ke, Y.; Shih, C.-J.; Paulus, G. L.; Wang, Q. H.; Mu, B.; Yin, P.; Strano, M. S., Metallized DNA nanolithography for encoding and transferring spatial information for graphene patterning. *Nature Communications* **2013,** *4* (1), 1-9.

117. Choi, J.; Chen, H.; Li, F.; Yang, L.; Kim, S. S.; Naik, R. R.; Ye, P. D.; Choi, J. H., Nanomanufacturing of 2D Transition Metal Dichalcogenide Materials Using Self‐Assembled DNA Nanotubes. *Small* **2015,** *11* (41), 5520-5527.

118. Hui, L.; Nixon, R.; Tolman, N.; Mukai, J.; Bai, R.; Wang, R.; Liu, H., Area-Selective Atomic Layer Deposition of Metal Oxides on DNA Nanostructures and Its Applications. *ACS Nano* **2020,** *14* (10), 13047-13055.

119. Aoi, K.; Takasu, A.; Okada, M., DNA-based polymer hybrids Part 1. Compatibility and physical properties of poly (vinyl alcohol)/DNA sodium salt blend. *Polymer* **2000,** *41* (8), 2847-2853.

120. Karni, M.; Zidon, D.; Polak, P.; Zalevsky, Z.; Shefi, O., Thermal degradation of DNA. *DNA and Cell Biology* **2013,** *32* (6), 298-301.

121. Pillers, M. A.; Lieberman, M., Thermal stability of DNA origami on mica. *Journal of Vacuum Science & Technology B, Nanotechnology and Microelectronics: Materials, Processing, Measurement, and Phenomena* **2014,** *32* (4), 040602.

122. Kim, H.; Surwade, S. P.; Powell, A.; O'Donnell, C.; Liu, H., Stability of DNA origami nanostructure under diverse chemical environments. *Chemistry of Materials* **2014,** *26* (18), 5265-5273.

123. Liu, X.; Zhang, F.; Jing, X.; Pan, M.; Liu, P.; Li, W.; Zhu, B.; Li, J.; Chen, H.; Wang, L., Complex silica composite nanomaterials templated with DNA origami. *Nature* **2018,** *559* (7715), 593-598.

124. Kim, H.; Arbutina, K.; Xu, A.; Liu, H., Increasing the stability of DNA nanostructure templates by atomic layer deposition of Al2O3 and its application in imprinting lithography. *Beilstein Journal of Nanotechnology* **2017,** *8* (1), 2363-2375.

125. Zhou, F.; Sun, W.; Ricardo, K. B.; Wang, D.; Shen, J.; Yin, P.; Liu, H., Programmably shaped carbon nanostructure from shape-conserving carbonization of DNA. *ACS Nano* **2016,** *10* (3), 3069-3077.

126. Pillers, M. A.; Lieberman, M., Embedded silicon carbide "replicas" patterned by rapid thermal processing of DNA origami on silicon. *Journal of Vacuum Science & Technology B, Nanotechnology and Microelectronics: Materials, Processing, Measurement, and Phenomena* **2016,** *34* (6), 060602.

127. Hofheinz, M.; Jehl, X.; Sanquer, M.; Molas, G.; Vinet, M.; Deleonibus, S., Simple and controlled single electron transistor based on doping modulation in silicon nanowires. *Applied Physics Letters* **2006,** *89* (14), 143504.

128. Vijayvargiya, V.; Vishvakarma, S. K., Effect of drain doping profile on double-gate tunnel field-effect transistor and its influence on device RF performance. *IEEE Transactions on Nanotechnology* **2014,** *13* (5), 974-981.

129. Elibol, O.; Morisette, D.; Akin, D.; Denton, J.; Bashir, R., Integrated nanoscale silicon sensors using top-down fabrication. *Applied Physics Letters* **2003,** *83* (22), 4613-4615.

130. Hao, X.; Cho, E.-C.; Scardera, G.; Shen, Y.; Bellet-Amalric, E.; Bellet, D.; Conibeer, G.; Green, M. A., Phosphorus-doped silicon quantum dots for all-silicon quantum dot tandem solar cells. *Solar Energy Materials and Solar Cells* **2009,** *93* (9), 1524-1530.

131. Sandow, C.; Knoch, J.; Urban, C.; Zhao, Q.-T.; Mantl, S., Impact of electrostatics and doping concentration on the performance of silicon tunnel field-effect transistors. *Solid-State Electronics* **2009,** *53* (10), 1126-1129.

132. Mukhopadhyay, S.; Raychowdhury, A.; Roy, K., Accurate estimation of total leakage in nanometer-scale bulk CMOS circuits based on device geometry and doping profile. *IEEE Transactions on Computer-Aided Design of Integrated Circuits and Systems* **2005,** *24* (3), 363-381.

133. Abelein, U.; Assmuth, A.; Iskra, P.; Schindler, M.; Sulima, T.; Eisele, I., Doping profile dependence of the vertical impact ionization MOSFET's (I-MOS) performance. *Solid-State Electronics* **2007,** *51* (10), 1405-1411.

134. Kennedy, N.; Duffy, R.; Eaton, L.; O'Connell, D.; Monaghan, S.; Garvey, S.; Connolly, J.; Hatem, C.; Holmes, J. D.; Long, B., Phosphorus monolayer doping (MLD) of silicon on insulator (SOI) substrates. *Beilstein Journal of Nanotechnology* **2018,** *9* (1), 2106-2113.

135. Liu, H.; Chen, Y.; He, Y.; Ribbe, A. E.; Mao, C., Approaching the limit: can one DNA oligonucleotide assemble into large nanostructures? *Angewandte Chemie International Edition* **2006,** *45* (12), 1942-1945.

136. Snow, E.; Deal, B., Polarization phenomena and other properties of phosphosilicate glass films on silicon. *Journal of the Electrochemical Society* **1966,** *113* (3), 263.

137. Sah, C.-T.; Sello, H.; Tremere, D., Diffusion of phosphorus in silicon oxide film. *Journal of Physics and Chemistry of Solids* **1959,** *11* (3-4), 288-298.

138. Palik, E.; Bermudez, V.; Glembocki, O., Ellipsometric Study of the Etch‐Stop Mechanism in Heavily Doped Silicon. *Journal of the Electrochemical Society* **1985,** *132* (1), 135.

139. Palik, E.; Faust Jr, J. W.; Gray, H.; Greene, R., Study of the Etch‐Stop Mechanism in Silicon. *Journal of the Electrochemical Society* **1982,** *129* (9), 2051.

140. Jackson, W.; Johnson, N.; Tsai, C.; Wu, I. W.; Chiang, A.; Smith, D., Hydrogen diffusion in polycrystalline silicon thin films. *Applied Physics Letters* **1992,** *61* (14), 1670-1672.

141. Gass, J.; Müller, H.; Stüssi, H.; Schweitzer, S., Oxygen diffusion in silicon and the influence of different dopants. *Journal of Applied Physics* **1980,** *51* (4), 2030-2037.

142. Pearson, A. C.; Liu, J.; Pound, E.; Uprety, B.; Woolley, A. T.; Davis, R. C.; Harb, J. N., DNA origami metallized site specifically to form electrically conductive nanowires. *The Journal of Physical Chemistry B* **2012,** *116* (35), 10551-10560.

143. Henini, M., Handbook of Semiconductor Manufacturing Technology. *Microelectronics* **2001,** *2* (32), 180.

144. Yurasov, D.; Drozdov, M.; Novikov, A., Method of selective doping of silicon by segregating impurities. *Technical Physics Letters* **2011,** *37* (9), 824.

145. Mack, C., Semiconductor Lithography (Photolithography)-The Basic Process. *The Basics of Microlithography* **2017**.

146. Barber, A. H.; Cohen, S. R.; Kenig, S.; Wagner, H. D., Interfacial fracture energy measurements for multi-walled carbon nanotubes pulled from a polymer matrix. *Composites Science Technology* **2004,** *64* (15), 2283-2289.

147. Zhang, X.; Sun, C.; Fang, N., Manufacturing at nanoscale: Top-down, bottom-up and system engineering. *Journal of Nanoparticle Research* **2004,** *6* (1), 125-130.

148. Gates, B. D.; Xu, Q.; Stewart, M.; Ryan, D.; Willson, C. G.; Whitesides, G. M., New approaches to nanofabrication: molding, printing, and other techniques. *Chemical Reviews* **2005,** *105* (4), 1171-1196.

149. Nakayama, Y.; Okazaki, S.; Saitou, N.; Wakabayashi, H., Electron‐beam cell projection lithography: A new high‐throughput electron‐beam direct‐writing technology using a specially tailored Si aperture. *Journal of Vacuum Science Technology B: Microelectronics Processing Phenomena* **1990,** *8* (6), 1836-1840.

150. Vieu, C.; Carcenac, F.; Pepin, A.; Chen, Y.; Mejias, M.; Lebib, A.; Manin-Ferlazzo, L.; Couraud, L.; Launois, H., Electron beam lithography: resolution limits and applications. *Applied Surface Science* **2000,** *164* (1-4), 111-117.

151. Deguchi, K.; Miyoshi, K.; Ishii, T.; Matsuda, T., Patterning characteristics of a chemically-amplified negative resist in synchrotron radiation lithography. *Japanese Journal of Applied Physics* **1992,** *31* (9R), 2954.

152. Wagner, C.; Harned, N., EUV lithography: Lithography gets extreme. *Nature Photonics* **2010,** *4* (1), 24.

153. Huie, J. C., Guided molecular self-assembly: a review of recent efforts. *Smart Materials Structures* **2003,** *12* (2), 264.

154. Cai, J.; Chen, H.; Huang, J.; Wang, J.; Tian, D.; Dong, H.; Jiang, L., Controlled self-assembly and photovoltaic characteristics of porphyrin derivatives on a silicon surface at solid–liquid interfaces. *Soft Matter* **2014,** *10* (15), 2612-2618.

155. Diagne, C. T.; Brun, C.; Gasparutto, D.; Baillin, X.; Tiron, R., DNA origami mask for sub-ten-nanometer lithography. *ACS Nano* **2016,** *10* (7), 6458-6463.

156. Pfitzner, E.; Wachauf, C.; Kilchherr, F.; Pelz, B.; Shih, W. M.; Rief, M.; Dietz, H., Rigid DNA beams for high‐resolution single‐molecule mechanics. *Angewandte Chemie International Edition* **2013,** *52* (30), 7766-7771.

157. Bai, R.; Du, Y.; Xu, A.; Hu, Y.; Erickson, J. R.; Hui, L.; Chen, J.; Xiong, F.; Liu, H., DNA‐Based Strategies for Site‐Specific Doping. *Advanced Functional Materials* **2021,** *31* (1), 2005940.

158. Abel, E.; Sabherwal, I., Reactions of the silicon–phosphorus bond. Part I. Insertions in trimethylsilyldiphenylphosphine. *Journal of the Chemical Society A: Inorganic, Physical, Theoretical* **1968**, 1105-1108.

159. Guo, D.-Z.; Hou, S.-M.; Zhang, G.-M.; Xue, Z.-Q., Conductance fluctuation and degeneracy in nanocontact between a conductive AFM tip and a granular surface under small-load conditions. *Applied Surface Science* **2006,** *252* (14), 5149-5157.

160. Melitz, W.; Shen, J.; Kummel, A. C.; Lee, S., Kelvin probe force microscopy and its application. *Surface Science Reports* **2011,** *66* (1), 1-27.

161. Sugimura, H.; Ishida, Y.; Hayashi, K.; Takai, O.; Nakagiri, N., Potential shielding by the surface water layer in Kelvin probe force microscopy. *Applied Physics Letters* **2002,** *80* (8), 1459-1461.

162. Thompson, S. E.; Parthasarathy, S., Moore's law: the future of Si microelectronics. *Materials Today* **2006,** *9* (6), 20-25.

163. Charles Jr, H. K., Miniaturized electronics. *Johns Hopkins APL Technical Digest* **2005,** *26* (4), 402-413.

164. Seisyan, R., Nanolithography in microelectronics: A review. *Technical Physics* **2011,** *56* (8), 1061.

165. Wu, M.-H.; Park, C.; Whitesides, G. M., Fabrication of arrays of microlenses with controlled profiles using gray-scale microlens projection photolithography. *Langmuir* **2002,** *18* (24), 9312-9318.

166. Costner, E. A.; Lin, M. W.; Jen, W.-L.; Willson, C. G., Nanoimprint lithography materials development for semiconductor device fabrication. *Annual Review of Materials Research* **2009,** *39*, 155-180.

167. Škereň, T.; Pascher, N.; Garnier, A.; Reynaud, P.; Rolland, E.; Thuaire, A.; Widmer, D.; Jehl, X.; Fuhrer, A., CMOS platform for atomic-scale device fabrication. *Nanotechnology* **2018,** *29* (43), 435302.

168. Bai, R.; Du, Y.; Xu, A.; Hu, Y.; Erickson, J. R.; Hui, L.; Chen, J.; Xiong, F.; Liu, H., DNA‐Based Strategies for Site‐Specific Doping. *Advanced Functional Materials* **2020**, 2005940.

169. Arole, V.; Munde, S., Fabrication of nanomaterials by top-down and bottom-up approaches-an overview. *J. Mater. Sci* **2014,** *1*, 89-93.

170. Sawant, S.; Baliga, B. J., Current saturation control in silicon emitter switched thyristors. *Solid-State Electronics* **2000,** *44* (1), 133-142.

171. Ghazi, H. E.; Jorio, A.; Zorkani, I., Analysis of temperature effect on IV characteristics of silicon (npn) emitter-base. *Moroccan Journal of Condensed Matter* **2009,** *11* (2).

172. Chehreh Chelgani, S.; Rudolph, M.; Kratzsch, R.; Sandmann, D.; Gutzmer, J., A review of graphite beneficiation techniques. *Mineral Processing and Extractive Metallurgy Review* **2016,** *37* (1), 58-68.

173. Jara, A. D.; Betemariam, A.; Woldetinsae, G.; Kim, J. Y., Purification, application and current market trend of natural graphite: A review. *International Journal of Mining Science and Technology* **2019,** *29* (5), 671-689.

174. Akanda, M. R.; Sohail, M.; Aziz, M. A.; Kawde, A. N., Recent advances in nanomaterial‐modified pencil graphite electrodes for electroanalysis. *Electroanalysis* **2016,** *28* (3), 408-424.

175. Kravchyk, K. V.; Wang, S.; Piveteau, L.; Kovalenko, M. V., Efficient aluminum chloride–natural graphite battery. *Chemistry of Materials* **2017,** *29* (10), 4484-4492.

176. Chung, D., Review graphite. *Journal of Materials Science* **2002,** *37* (8), 1475-1489.

177. Eda, G.; Fanchini, G.; Chhowalla, M., Large-area ultrathin films of reduced graphene oxide as a transparent and flexible electronic material. *Nature Nanotechnology* **2008,** *3* (5), 270-274.

178. Balandin, A. A.; Ghosh, S.; Bao, W.; Calizo, I.; Teweldebrhan, D.; Miao, F.; Lau, C. N., Superior thermal conductivity of single-layer graphene. *Nano Letters* **2008,** *8* (3), 902-907.

179. Yuan, W.; Shi, G., Graphene-based gas sensors. *Journal of Materials Chemistry A* **2013,** *1* (35), 10078-10091.

180. Justino, C. I.; Gomes, A. R.; Freitas, A. C.; Duarte, A. C.; Rocha-Santos, T. A., Graphene based sensors and biosensors. *TrAC Trends in Analytical Chemistry* **2017,** *91*, 53-66.

181. Han, T.-H.; Kim, H.; Kwon, S.-J.; Lee, T.-W., Graphene-based flexible electronic devices. *Materials Science and Engineering: R: Reports* **2017,** *118*, 1-43.

182. Han, T.-H.; Lee, Y.; Choi, M.-R.; Woo, S.-H.; Bae, S.-H.; Hong, B. H.; Ahn, J.-H.; Lee, T.-W., Extremely efficient flexible organic light-emitting diodes with modified graphene anode. *Nature Photonics* **2012,** *6* (2), 105-110.

183. Yin, Z.; Zhu, J.; He, Q.; Cao, X.; Tan, C.; Chen, H.; Yan, Q.; Zhang, H., Graphene ‐ based materials for solar cell applications. *Advanced Energy Materials* **2014,** *4* (1), 1300574.

184. Zhan, B.; Li, C.; Yang, J.; Jenkins, G.; Huang, W.; Dong, X., Graphene field ‐ effect transistor and its application for electronic sensing. *Small* **2014,** *10* (20), 4042-4065.

185. Sque, S. J.; Jones, R.; Briddon, P. R., The transfer doping of graphite and graphene. *Physica Status Solidi (A)* **2007,** *204* (9), 3078-3084.

186. Hansen, W. N.; Hansen, G. J., Standard reference surfaces for work function measurements in air. *Surface Science* **2001,** *481* (1-3), 172-184.

187. Lägel, B.; Ayala, M.; Schlaf, R., Kelvin probe force microscopy on corona charged oxidized semiconductor surfaces. *Applied Physics Letters* **2004,** *85* (20), 4801-4803.

188. Böhmisch, M.; Burmeister, F.; Rettenberger, A.; Zimmermann, J.; Boneberg, J.; Leiderer, P., Atomic force microscope based Kelvin probe measurements: application to an electrochemical reaction. *The Journal of Physical Chemistry B* **1997,** *101* (49), 10162-10165.

189. Glatzel, T.; Rusu, M.; Sadewasser, S.; Lux-Steiner, M. C., Surface photovoltage analysis of thin CdS layers on polycrystalline chalcopyrite absorber layers by Kelvin probe force microscopy. *Nanotechnology* **2008,** *19* (14), 145705.

190. Liscio, A.; Palermo, V.; Müllen, K.; Samorì, P., Tip− sample interactions in Kelvin probe force microscopy: quantitative measurement of the local surface potential. *The Journal of Physical Chemistry C* **2008,** *112* (44), 17368-17377.

191. Sommerhalter, C.; Matthes, T. W.; Glatzel, T.; Jäger-Waldau, A.; Lux-Steiner, M. C., High-sensitivity quantitative Kelvin probe microscopy by noncontact ultra-high-vacuum atomic force microscopy. *Applied Physics Letters* **1999,** *75* (2), 286-288.

192. Kim, C. H.; Bae, C. D.; Ryu, K. H.; Lee, B. K.; Shin, H. J. In *Local work function measurements on various inorganic materials using Kelvin probe force spectroscopy*, Solid State Phenomena, Trans Tech Publ: 2007; pp 607-610.

193. Fernández Garrillo, P. A.; Grévin, B.; Chevalier, N.; Borowik, Ł., Calibrated work function mapping by Kelvin probe force microscopy. *Review of Scientific Instruments* **2018,** *89* (4), 043702.

194. Sadewasser, S.; Glatzel, T., Comment on "electrostatic force microscopy on oriented graphite surfaces: coexistence of insulating and conducting behaviors". *Physical Review Letters* **2007,** *98* (26), 269701.

195. Zheng, Y.; Ando, T., Hall conductivity of a two-dimensional graphite system. *Physical Review B* **2002,** *65* (24), 245420.

196. Pietronero, L.; Strässler, S.; Zeller, H.; Rice, M., Electrical conductivity of a graphite layer. *Physical Review B* **1980,** *22* (2), 904.

197. Banerjee, S.; Sardar, M.; Gayathri, N.; Tyagi, A.; Raj, B., Conductivity landscape of highly oriented pyrolytic graphite surfaces containing ribbons and edges. *Physical Review B* **2005,** *72* (7), 075418.

198. Wastl, D. S.; Speck, F.; Wutscher, E.; Ostler, M.; Seyller, T.; Giessibl, F. J., Observation of 4 nm pitch stripe domains formed by exposing graphene to ambient air. *ACS Nano* **2013,** *7* (11), 10032-10037.

199. Li, Z.; Wang, Y.; Kozbial, A.; Shenoy, G.; Zhou, F.; McGinley, R.; Ireland, P.; Morganstein, B.; Kunkel, A.; Surwade, S. P., Effect of airborne contaminants on the wettability of supported graphene and graphite. *Nature Materials* **2013,** *12* (10), 925-931.

200. Temiryazev, A.; Frolov, A.; Temiryazeva, M., Atomic-force microscopy study of self-assembled atmospheric contamination on graphene and graphite surfaces. *Carbon* **2019,** *143*, 30-37.

201. Kozbial, A.; Li, Z.; Sun, J.; Gong, X.; Zhou, F.; Wang, Y.; Xu, H.; Liu, H.; Li, L., Understanding the intrinsic water wettability of graphite. *Carbon* **2014,** *74*, 218-225.

202. Hurst, J. M.; Li, L.; Liu, H., Adventitious hydrocarbons and the graphite-water interface. *Carbon* **2018,** *134*, 464-469.

203. Salim, M.; Hurst, J.; Montgomery, M.; Tolman, N.; Liu, H., Airborne contamination of graphite as analyzed by ultra-violet photoelectron spectroscopy. *Journal of Electron Spectroscopy and Related Phenomena* **2019,** *235*, 8-15.

204. Metois, J.; Heyraud, J.; Takeda, Y., Experimental conditions to obtain clean graphite surfaces. *Thin Solid Films* **1978,** *51* (1), 105-117.

205. Sen, A.; Bercaw, J. E., Thermal desorption studies on hydrogen-and oxygen-terminated graphite surfaces. *The Journal of Physical Chemistry* **1980,** *84* (4), 465-466.

206. Martinez-Martin, D.; Longuinhos, R.; Izquierdo, J. G.; Marele, A.; Alexandre, S. S.; Jaafar, M.; Gómez-Rodríguez, J. M.; Bañares, L.; Soler, J. M.; Gomez-Herrero, J., Atmospheric contaminants on graphitic surfaces. *Carbon* **2013,** *61*, 33-39.

207. Nouzák, L.; Richterová, I.; Pavlů, J.; Němeček, Z.; Šafránková, J., Investigations of the photoemission from glass dust grains. In *WDS'14 Proc. Contrib. Papers—Phys.*, 2014; pp 361-370.

208. Michaelson, H. B., The work function of the elements and its periodicity. *Journal of Applied Physics* **1977,** *48* (11), 4729-4733.

209. Gu, D.; Sistiabudi, R.; Dey, S. K., Modification of work function of Ti by self-assembled monolayer molecules on Si O 2 ／ p ‐ Si. *Journal of Applied Physics* **2005,** *97* (12), 123710.

210. de Boer, B.; Hadipour, A.; Mandoc, M. M.; van Woudenbergh, T.; Blom, P. W., Tuning of metal work functions with self ‐ assembled monolayers. *Advanced Materials* **2005,** *17* (5), 621-625.

211. Leung, T.; Kao, C.; Su, W.; Feng, Y.; Chan, C., Relationship between surface dipole, work function and charge transfer: Some exceptions to an established rule. *Physical Review B* **2003,** *68* (19), 195408.

212. Fan, W.; Chakraborty, A., Investigation of the interaction of polar molecules on graphite surface: prediction of isosteric heat of adsorption at zero surface coverage. *The Journal of Physical Chemistry C* **2016,** *120* (41), 23490-23499.

213. Chao Niu, T.; Li Huang, Y.; Tao Sun, J.; Kera, S.; Ueno, N.; Thye Shen Wee, A.; Chen, W., Tunable two-dimensional molecular dipole dot arrays on graphite. *Applied Physics Letters* **2011,** *99* (14), 143114.

214. Lee, I.; Chung, E.; Kweon, H.; Yiacoumi, S.; Tsouris, C., Scanning surface potential microscopy of spore adhesion on surfaces. *Colloids and Surfaces B: Biointerfaces* **2012,** *92*, 271-276.

215. Drolle, E.; Ngo, W.; Leonenko, Z.; Subbaraman, L.; Jones, L., Nanoscale characteristics of ocular lipid thin films using Kelvin probe force microscopy. *Translational Vision Science & Technology* **2020,** *9* (7), 41-41.